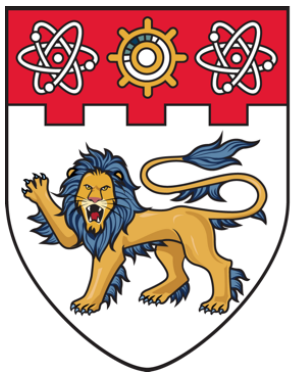

NANYANG TECHNOLOGICAL UNIVERSITY
SINGAPORE

Impact absorption in shear-stiffening materials

Anatoli Kurkin

SCHOOL OF MATERIALS SCIENCE AND ENGINEERING

2022

IMPACT ABSORPTION IN SHEAR-STIFFENING MATERIALS

Anatoli Kurkin

SCHOOL OF MATERIALS SCIENCE AND ENGINEERING

A thesis submitted to the Nanyang Technological University
in partial fulfilment of the requirement for the degree of
Doctor of Philosophy

2022

Statement of Originality

I hereby certify that the work embodied in this thesis is the result of original research, is free of plagiarised materials, and has not been submitted for a higher degree to any other University or Institution.

12/08/2022
Date

Kurkin Anatolii

Supervisor Declaration Statement

I have reviewed the content and presentation style of this thesis and declare it is free of plagiarism and of sufficient grammatical clarity to be examined. To the best of my knowledge, the research and writing are those of the candidate except as acknowledged in the Author Attribution Statement. I confirm that the investigations were conducted in accord with the ethics policies and integrity standards of Nanyang Technological University and that the research data are presented honestly and without prejudice.

17 Aug 2022

. . . . . .

Date

Assoc Prof Alfred Tok

. . . . . .

Authorship Attribution Statement

This thesis contains material from 2 papers published in the following peer-reviewed journals in which I am listed as an author.

Chapter 4 is published as A. Kurkin, V. Lipik, X. Zhang and A. Tok. In Situ Observation of Shear-Induced Jamming Front Propagation during Low-Velocity Impact in Polypropylene Glycol/Fumed Silica Shear Thickening Fluids. *Polymers* **14** (14), 2768 (2022). DOI: 10.3390/polym14142768.

The contributions of the co-authors are as follows:

- I designed the study and performed all experiments at the School of Materials Science and Engineering (NTU) as well as analyzed the data and prepared the manuscript draft. The manuscript was revised by Dr. Lipik and Asst Prof. Zhang.
- Dr Lipik assisted in the interpretation of results and actively participated in discussions.
- Assistant Prof Zhang helped to analyze the speed camera recordings using digital image correlation (DIC) software.
- Associate Prof Tok provided the initial project direction and helped to edit the manuscript drafts.

Chapter 5 is published as A. Kurkin, V. Lipik, K. Tan, G. L. Seah, X. Zhang and A. Tok. Correlations Between Precursor Molecular Weight and Dynamic Mechanical Properties of Polyborosiloxane (PBS). *Macromolecular Materials and Engineering* **306** (11), 2100360 (2021). DOI: 10.1002/mame.202100360.

The contributions of the co-authors are as follows:

- I designed the study, conducted all characterization (except GPC) and interpretation of the data, wrote the drafts of the manuscript. The manuscript was revised by Dr. Lipik and Asst Prof. Zhang.
- Dr. Lipik assisted in the results interpretation and revised the manuscript.

- Mr. Tan conducted the synthesis of the samples under my guidance.
- Dr. Seah conducted GPC characterization and analysis of the data.
- Asst Prof. Zhang helped with the design of the study and revised the manuscript.
- Assoc Prof. Tok. supervised the project, provided resources and reviewed the manuscript.

12/08/2022
Date

Kurkin Anatolii

Abstract

Nowadays there is a huge demand for protective gear in the sports industry due to the growing popularity of extreme sports in view of their greater availability. The need for them is not limited to extreme sports but spreads wider to sports with a high risk of injuries, such as hockey, American football, skiing, skateboarding, cycling, etc.

A new class of "smart" protective materials – shear-stiffening materials, is intended to replace outdated solutions in a view of their advantages. Specifically, self-healing ability (hence, recyclability and reusability), ability to spread out the impact over a large area, and most importantly instant stiffening response to external stimuli which is completely reversible. Presently, two types of shear stiffening materials exist – shear thickening fluid (STF) which is a liquid dense suspension, and shear-stiffening gel (SSG) which is a supramolecular polymer network. However, it remains unclear how does the impact energy is dissipated in them and how features of their stiffening mechanism (jamming – in STF and dynamic crosslinking – in SSG) contribute to impact absorption.

Jamming has been found to play a major role in impact dissipation on the example of polypropylene glycol/fumed silica STF. For the first time, using novel optical in situ speed recording of impact it was found that jamming can be triggered at as low volume fraction as $\phi > 7.2\%$. Analysis of the flow field during impact revealed that the front propagation speed is 3-5 times higher than the speed of the impactor rod, which rules out jamming by densification, showing that the growth of jamming front is triggered by shear. The main impact absorption begins when the jamming front reaches the boundary, creating a solid-like plug under the rod that confronts its movement. These results provide important insights into the impact absorption mechanism in fumed silica suspensions with a focus on shear jamming.

It was discovered that the stiffening response of the best known representative of SSG – polyborosiloxane (PBS), can be controlled by the molecular weight of the precursor due to chosen straightforward condensation synthesis routine. Introduced boron cites through Si-

O-B bridges behave as dynamic crosslinks and are responsible for shear-stiffening properties. The dynamic crosslinking density which was quantified by Si-O-B infrared band intensity was shown to define the efficiency of impact absorption. PBS demonstrated a linear increase in peak forces with a decrease in the number of Si-O-B bonds during the drop weight impact test. Therefore, the low molecular weight of a precursor, hence, a high number of dynamic crosslinks is a primary requirement for effective protection against low-velocity impact.

The origins of dynamic crosslinking in PBS are in debate for many decades. Here, we show that it does not involve hydrogen bonding, dative bonding or formation/exchange of boron anhydrides as was proposed earlier but solely is the result of associative dynamic exchange of Si-O-B covalent bonds. The formation and breakage of Si-O-B bonds were found to have a low energy barrier, therefore, can be easily formed and exchanged at room temperature. It was also found that the viscoelastic properties of PBS are largely dependent on the B-O functionality of the boron compound. Trifunctional boron crosslinking through B-O bonds results in gelation whereas bifunctional phenylboronic acid provided only chain extension without any signs of gelation. Therefore, mechanical properties could be tuned by the right choice of boron functionality which results in n-functional dynamic covalent bonds $(\text{-Si-O})_n\text{-B}$.

Lay Summary

The rapid development of the world pushes people to greater heights, for example in sports. World records continue to grow every year owing to the development of technologies to maximize the potential of athletes. However, this increases the likelihood of injury and its severity. To keep up with the times, new protective solutions are being developed to replace existing ones due to their obsolescence.

Protective equipment can become "smart" if special materials are introduced that can effectively adapt to different exploiting conditions. Shear-stiffening materials (SSM) are of that kind, they are liquid when deformed slowly but solidify upon impact absorbing a lot of shock energy. SSM-based protective gear would less hinder movements which makes it indispensable in situations in which the mobility and comfort of the athlete are a priority. Also, due to their unique self-healing ability, they can be reused many times and easily recycled.

In this thesis, we have set a goal to reveal details on the mechanism of impact absorption in SSMs with respect to their stiffening mechanism and assess their potential for substitution of conventional protective solutions.

Acknowledgements

This dissertation would not have been possible without financial support from the Singapore International Graduate Award (SINGA) during my PhD program. It allowed me to focus on the research without financial worries.

Special thanks are conveyed to my research project supervisor Professor Alfred Tok for his continual guidance and support throughout all four years of the program. I am very grateful for giving me the opportunity to join NTU and his group. I would like to extend my thanks to my mentor Dr. Vitali Lipik for his research insights and incisive recommendations concerning the scope of the research and to my collaborator Dr. Zhang Xin for his active participation in the discussion and the interpretation of the results.

Special thanks to my TAC members Prof Leong Kah Fai and Prof Tan Kwan Wee for their constructive criticism of my work and valuable support. I would also like to extend my gratitude to Prof John V. Hanna and David Bradley for the input who performed MNR experiments and gave valuable advice. I am most grateful to Dr. Zoey Seah for her expert input and experimental help, Dr. Bhudolia Somen for the fruitful discussions, and for allowing me to use his team's facilities, and Dr. Dre for constant support.

My work would be more difficult without the help of all the technicians (especially Zi Li Gan, Wilson Lim, and Nelson Ng) and the staff of the School of Materials Science and Engineering (NTU), who provided great support and persevered in training me to use the instruments. I also had a great pleasure working with all members of my research group (especially Dr. Ronn Goei and Amanda Jiaming) and the research team of the Sportmaster R&D lab, I am grateful for their continued support.

I would like to especially thank my family and friends for their faith in me and their support during this difficult time for me. Without the help and support from Yulia Lekina and Anna Korsakova I could not imagine making it.

Table of Contents

Table Captions

Figure Captions

Figure 2.9 (**a**) Storage modulus of SSG as a function of angular frequency with liquid/solid transition. Reprinted with permission from reference[32]. Copyright 2014, American Institute of Physics; (**b**) Cold flow of SSG, impact-induced hardening and with elastic rebound of SSG. Reprinted with permission from reference.[13] Copyright 2022, Elsevier.

Figure 2.10 (**a**) Illustration of the different states of PBS at different deformation rates. Viscous liquid state at low rates, elastomeric state at intermediate, and glassy states and high strain rates. Reprinted with permission from reference[17]. Copyright 2016, Elsevier; (**b**) Mechanism of impact dissipation which results in expansion of impact area. Reprinted with permission from reference[14]. Copyright 2020, Elsevier.

Figure 2.11 Proposed mechanisms of dynamic crosslinking in PBS.

Figure 2.12 Proposed molecular structure of PBS through condensation synthesis at 200 ºC, the scheme is developed based on the reaction described by Zinechenko.[126] From the top to the bottom: linear borono-terminated (ortho-borate), linear boroxine terminated (meta-borate), and cyclic molecules.

Figure 2.13 Reactants and synthesis outcomes of PBS; the scheme is developed based on the reaction described in a study by Liu[28]. They observed the formation of boroxine molecules which hydrolyze into borono-terminated molecules when equilibrated with air humidity.

Figure 2.14 Various bifunctional and trifunctional boron compounds (defined by B-O_n- or B-Cl_n-) reacted with hydroxy-terminated PDMS; the scheme is developed based on reactions described in a study by Gridina and co-workers.[30] They found that only trifunctional boron compounds result in gelation of PBS whereas bifunctional demonstrate a mild increase in viscosity only.

Figure 2.15 The scheme is developed based on reactions described by Mitrofanov and co-workers[43] for PBS synthesis. From the top to the bottom: reversible formation of boron trioxide from boric acid by dehydration, condensation of hydroxy-terminated PDMS with boric acid at 160 ºC, thermal cleavage of cyclic dimethyl siloxanes molecules at 240 ºC followed by insertion of boron trioxide, condensation with hydroxy-terminated PDMS with boron trioxide at room temperature with possible molecular structures of products.

Figure 2.16 (**a**) Synthesized telechelic PBS where phenylboronic acid is covalently attached to PDMS through phenyl ring and protected ester groups; the scheme is developed based on the reaction description from ref.[144] Protective groups were later hydrolyzed in water which led to the formation of the elastomeric film on the water surface. (**b**) Synthesized pendant PBS protected with hydrolysable ester group; the scheme is developed based on the reaction description from ref. [42]

Figure 2.17 Synthesis scheme of simple PBS from a trimethyl borate with hydroxy-terminated PDMS which results in a trifunctional crosslinking through Si-O-B bonds and release of methanol; the scheme is developed based on the reaction description from ref.[29]

Figure 2.18 (**a**) Formation and exchange of boronic esters. The dissociative mechanism of exchange through dehydration/hydrolysis (on the left) and associative mechanism through transesterification and metathesis (on the right). (**b**) Formation and exchange of boroxines from boronic acids. The formation can occur through direct dehydration or Lewis base facilitated dehydration. The exchange of boroxines occurs through metathesis. Reprinted with permission from ref.[44] © Royal Society of Chemistry.

Figure 3.1 Anton Paar MCR 501 rotational rheometer which was used in this thesis with a parallel plate spindle.

Figure 3.2 Drop-weight impact testing machine CADEX Twin Wire 1000 kg which was used in this thesis.

Figure 3.3 Basics of the attenuated total reflection (ATR) method of infrared spectroscopy.

Figure 3.4 Basics of gel-permeation chromatography. Adapted with permission from ref. Copyright © 2009 John Wiley & Sons, Inc.

Figure 3.5 Energy levels splitting in magnetic field (Zeeman effect).

Figure 3.6 Basic principles of MALDI-MS technique with an axial time-of-flight (ToF) detector.

Figure 4.1 Custom setup for pull-up tests: (**a**) Photo of the setup with a pneumatic grip holding the cylindrical rod at the top and the sample holder attached at the bottom; (**b**) Schematic illustration of the starting position during the pull-up test with all dimensions shown.

Figure 4.2 Illustrations of low-velocity impact setups. (**a**) The drop weight impact setup with a custom 3d printed TPU container. All samples were filled to the 13 mm thickness level from the bottom. Height from the surface of STF to the tip of the hemispherical impactor was a controlled parameter. (**b**) The acrylic glass setup which was used together with a speed camera for the flow field analysis during impact. All samples were subjected to the impact from the same height (327 mm).

Figure 4.3 Flow rheological analysis of STF at three weight fractions. Viscosity as a function of shear rate in a parallel plates geometry with a 0.5 mm gap. Numbers on the arrows represent ratios of viscosities at different stages, the first two values at the bottom during the Newtonian stage, values on top ratios at the maximum viscosities. An additional graph inside the main is a shear stress-rate plot which was used for power-law fitting to establish the regime of shear thickening (DST or CST). (1, 3) Photos of STF 25% and 15% during flow tests at the maximum viscosity when fluid starts to slip off (17 1/s and 18 1/s, respectively), (2) when STF 25% becomes cloudy (41 1/s); (4) in contrast to STF 25%,

STF 15% did not demonstrate any change in optical properties (at 42 1/s).

Figure 4.4 Extensional "pull-up" test, peak forces at each individual extensional rate test were plot against the rate, peak forces are plot in a log scale. Normal force profile at 8mm/s is shown in the middle of the figure, at this rate peak force values reach the plateau.

Figure 4.5 Results from the drop weight test with the hemispherical impactor. (**a**) Peak forces at six different energies with error bars. Percentages represent the weight fraction of fumed silica in STF. Each value is the average of ten tests with an error not exceeding 10%. (**b**) Normal force registered with the load cell as a function of time during 30 J impact. These curves are also the average over ten tests.

Figure 4.6 Change in impactor depth for two types of impact tests and the resemblance between them. (**a**) Rod depth against time during speed camera impact test. The speed of the rod before the impact $v_0 = 2.4\ m/s$. Photographs from the speed camera when the rod is completely stopped (19.4 mm for STF 25%, 23.7 mm for STF 20%, and the rod hit the bottom for STF 15% at 30.6 mm depth). Recording of whole tests is shown in Supplementary Video 1. (**b**) Calculated force-displacement (depth) profiles for drop weight test at 30 J. Displacement was calculated from the integration of the velocity-time plot, which in turn was obtained by integrating the force-time plot divided by the impactor weight.

Figure 4.7 Jamming front propagation during impact. Calculated jamming front thickness during the impact of STF for three particles weight fractions. Front thickness was obtained measuring the maximum thickness of the third strain isoline (dark orange) in a vertical direction from the rod bottom surface. (1-3) Color-graded strain fields were calculated using DIC software. Red represents the highest displacement value where yellow is the lowest, green color represents no displacement. The red zone is the jamming front propagating towards the bottom at a speed faster than the speed of the rod. Captured pictures are front dimensions at the moment of reaching the bottom.

molecular weight of precursors.

Figure 6.1 (**a**) FTIR spectra of PBS samples synthesized at room temperature (B25RT), with heating in toluene in a Dean-Stark apparatus (B25), 15 min after addition of boric acid to PDMS25 without any stirring (B25RT2), and precursor (PDMS25). The inset is the zoomed-in plot in the tetrahedral B-O asymmetric stretching zone. (**b**) Gauss function fit of B25 spectra in a trigonal B-O asymmetric stretching zone with $R^2 = 0.9999$. (**c**) Splitting of asymmetric B-O stretching band based on a symmetry of boron compound (free BA, one, two, and three protons substituted BA molecules).

Figure 6.2 1D spectrum of boric acid alone (BA precursor) and B25 acquired at 16.4 T with 10 kHz spinning. The line shape is fit using the quadrupole parameters (CQ = 2300, 2400 kHz, $\eta = 0.2$) that were obtained from solid-state ^{11}B-NMR, with red curves being a sum of the fits. BO_3 ring corresponds to the three-coordinate boroxine species and the BO_3 non-ring to the other three-coordinate boron species. Chemical shifts $\boldsymbol{\delta_{iso}}$ = 16.0 and 19.3 ppm (BA), 13.9 ppm (B25).

Figure 6.3 FTIR spectra of three PBS samples: B25 equilibrated with the laboratory moist, B25 hydrolyzed in a 10:1 solution of THF/H_2O, and B25 directly mixed with water after 20 minutes.

Figure 6.4 MALDI-ToF-MS spectra of the precursor (PDMS 25) versus PBS product (B25). Peaks coincide due to hydrolysis of B25 upon contact with water during the co-crystallization stage.

Figure 6.5 Apparent viscosities as a function of shear rate. In the selected range of rates, all PBA-based PBS demonstrated Newtonian flow. Numbers indicate an n-times increase in apparent viscosities with respect to the silicone oil precursor.

Figure 6.6 (**a**) FTIR spectra of PBS samples synthesized with bifunctional phenylboronic acid (PBA) from different MW PDMS. The inset is the zoomed-in plot in

the 1200-1500 cm^{-1} range. (**b**) Gauss function fit of P25 spectra in a trigonal B-O asymmetric stretching zone with $R^2 = 0.9999$. (**c**) 1D spectrum of P25 versus B25 acquired at 16.4 T with 10 kHz spinning (black curve). The line shape is fit using the quadrupole parameters (CQ = 2300, 2400 kHz, $\eta = 0.2$) that were obtained from solid-state ^{11}B-NMR (red curve). Chemical shifts $\boldsymbol{\delta_{iso}}$ = 16.0 and 26.0 ppm (P25), 13.9 ppm (B25).

Figure 7.1 Jamming front prorogation during low-velocity impact in fumed silica/polypropylene glycol.

Figure 7.2 Drop weight impact test of PBS samples. a) Illustration of the testing setup; b) peak forces generated during impact test against MW of the PBS with three distinctive zones; c) schematic illustration of the molecular structure in Zone 1 (on the left) and Zone 3 (on the right) during low-velocity impact.

Figure 7.3 Illustration of drop weight impact setup for testing 11 mm thick layers of STF 25%, SSG, and EVA foam sample in a TPU container. On the right, peak force values at different impact energies; each data point is an average value over ten tests.

Figure 7.4 Results of the drop weight impact test for three SSG layers thicknesses (11, 5.5, and 2.7 mm) versus EVA foam and STF 25%. Peak forces are generated at different impact energies; each data point is an average value over ten tests.

Figure 7.5 (**a**) 3D models of the honeycomb (closed-cell topology) and gyroid (continues topology) structures; (**b**) drop weight test results of the FDM printed composites from a self-produced PEBAX filament subjected to 7.5 J impact, two types of samples were produced for each structure – one, empty (unfilled) and another filled with STF 15% (PPG/fumed silica); (**c**) Photos of composites testing setup (on the left), broken walls of the matrix with STF leaking out (on the right).

Figure 7.6 (**a**) Schematic of the setup used for STF encapsulation. (**b**) Illustration showing the formation mechanism and structure of the outer and inner walls of the STF

capsule. (**c**) Optical image of the obtained capsules with one enlarged in the inset. (**d**) A broken STF capsule Reprinted with permission from reference [71]. © Royal Society of Chemistry

Figure 7.7 Orifice coagulation bath method for STF encapsulation. Reprinted with permission from reference [197] © 2020 Elsevier Ltd.

Figure 7.8 Soft composite concept where PBS is the middle layer closed by 3D fabric from two sides and stitched over the area.

Figure 7.9 Concept of bicomponent yarns with PBS being a core and polyester (PE) a shell for protective fabrics.

Abbreviations

STF	Shear Thickening Fluid
SSG	Shear Stiffening Gel
PBS	Polyborosiloxane
SSM	Shear Stiffening Material
PPG	Polypropylene Glycol
MW	Molecular Weight
CP	Crossover point
FTIR	Fourier Transform Infrared Spectroscopy
IR	Infrared
NMR	Nuclear Magnetic Resonance
MALDI	Matrix Assisted Laser Desorption Ionization
ToF	Time-of-Flight
MS	Mass Spectrometry
DST	Discontinuous Shear Thickening
SJ	Shear Jamming
PDMS	Polydimethylsiloxane
ARL	Army Research Laboratory
UHMWPE	Ultra Hight Molecular Weight Polyethylene
PU	Polyurethane
PE	Polyethylene
PVA	Polyvinyl Alcohol
BPO	Benzoyl Peroxide
CST	Continues Shear Thickening
CSR	Critical Shear Rate
STR	Shear Thickening Ratio
VCSR	Viscosity at the Critical Shear Rate
MV	Maximum Viscosity
PEG	Polyethylene Glycol
BA	Boric Acid

PBA	Phenylboronic Acid
CIP	Carbonyl Iron Particles
CNT	Carbon Nano Tube
SHPB	Split Hopkinson Pressure Bar
TRIS	Trisaminomethane
PVDF	Polyvinylidene Fluoride
PP	Parallel Plate
CP	Cone and Plate
CC	Concentric Cylinders
ATR	Attenuated Total Reflection
GPC	Gel Permeation Chromatography
HPLC	High Performance Liquid Chromatography
MAS	Magic Angle Spinning
DHB	Dihydroxybenzoic Acid
KI	Potassium Iodide
THF	Tetrahydrofuran
TPU	Thermoplastic Urethane
DIC	Digital Image Correlation
PMMA	Polymethyl Methacrylate
DMA	Dynamic Mechanical Analysis
DMF	Dimethylformamide
IPA	Isopropyl Alcohol
RT	Room Temperature
EVA	Ethylene Vinyl Acetate
FDM	Fused Deposition Modeling
PEI	Polyethylenimine

Chapter 1

Introduction

This chapter introduces the background of the impact of protective materials in sports and discusses the potential of shear-stiffening materials to replace outdated conventional solutions. Next, we discuss the most promising representatives of this class of materials – shear thickening fluid (STF) and shear-stiffening gels (SSG), as well as protective composites based on them. After that, we formulate the remaining challenges for their successful implementation as bulk protection which we attempt to resolve in this thesis followed by objectives and scope, an overview of the entire thesis, and outcomes with a focus on the significance and novelties.

1.1 Background

Nowadays, there is a vast demand for protective gear in the sports industry because the health and safety of people doing sports are of significant interest. Proper protective equipment is essential in sports where a high risk of injuries is involved, such as hockey, American football, skiing, motorcycling, skateboarding, etc[1–4].

There are plenty of existing solutions in the form of soft protection. Minimizing the probability of injuries and absorbing as much impact as possible remain the main aims of these solutions. Still up to date, in most cases, polymeric low-density foams are used; they typically dissipate energy through the cell buckling, bending, or fracture[5–7]. Two types of foams exist depending on their cellular structure (closed-cell or open-cell, respectively). Closed-cell polymeric foams are usually stronger and more efficient in shock absorption since air enclosed in foam voids performs the work of the damper and absorbs the bulk of the energy during the compression-decompression cycle[8]. And in the case of an open-cell foam, the air easily leaves the volume of the foam, negating energy absorption due to air compression. It is worth noting that existing solutions were developed decades ago and reached the maximum of their capabilities in view of physical limitations. For example, a critical weakness of polymeric foams is that the pressure during impact concentrates at one point, which significantly concerns athletes' safety[9]. That is why rigid panels are usually combined with foam in protective gear to spread the impact over a larger area[10]. However, bulky and inflexible, these solutions reduce the user's mobility and comfort. Other limitations include thickness restriction, a limited range of impact energies, loss of damping performance over time due to deformation cycles in flexible foams, and irreversible deformation in rigid foams after the first impact[10]. Also, foams' high thermal insulation properties may lead to overheating the user[11]. Permanent crosslinking, beneficial for mechanical properties, often makes the materials non-recyclable.

In the light of advances in research of "smart" materials, new solutions were proposed to overcome mentioned limitations. Shear-stiffening materials are one of the most prospective candidates[12,13]. Their unique features include self-healing (hence, recyclability), the ability

to spread out the impact over a large area[14], and most importantly, instant stiffening response to external stimuli, which is completely reversible[15–17]. Presently, two types of shear stiffening materials exist – shear thickening fluid (STF), a dense suspension, and shear-stiffening gel (SSG), a supramolecular polymer network[13].

STF is a non-Newtonian fluid whose viscosity increases by several orders of magnitude with shear stress[12,18]. This type of fluid has been known for a very long time, but it found application not long ago. Today, one of the widest applications of STF is in liquid armor[19]. Kevlar sheets are impregnated with STF and then dried. Improved bulletproof properties of liquid armor are associated with increased friction between Kevlar yarns[12]. Friction dramatically reduces the main disadvantage of Kevlar fabric, the so-called windowing effect, in which the fibers move apart upon penetration impact. However, STF impact absorption impact on its own is a relatively unexplored subject for all its enormous potential.

Despite the different nature and origin of the stiffening mechanism, SSG undergoes a similar liquid/solid transition with an increase in shear rate and so the elastic modulus, and it exhibits highly elastic behavior as a solid body[20]. A few successful companies (such as D3O®, and Armorgel®)[21,22] have utilized SSG as a "smart" component of their polyurethane foams for impact protective gear. However, SSG was added at a small concentration as a filler, and the foam is responsible for the main protective effect. And this is the only successful application of SSG in the field of protection today. Therefore, the aptitude of SSG to mitigate impact alone remains unclear.

1.2 Problem Statement

Suspension of fumed silica in polar organic oligomers (such as polypropylene glycol) is the most successfully implemented STF for protective composites due to high stability [23,24] (which prevent sedimentation of particles over time) and strong shear thickening at low particle loading[25,26]. Despite various studies on the rheology of fumed silica suspensions and protective performance of its composites, the impact absorption mechanism remains unknown. This gap needs to be filled for the effective implementation of STF as bulk protection and improvement of protective properties.

Polyborosiloxane (PBS) is the most utilized representative of the SSG class in the field of protective equipment for being easily synthesized from a relatively cheap component due

to the wide availability of methods to tailor dynamic and mechanical properties[13]. There are two branches of PBS research that are not well connected. One aims to modify the rheological properties through various approaches (manipulation with the density of supramolecular network[27–30], the addition of functional fillers[31–34] or permanent crosslinks[35–37], and chemical modification[38]). Another targets impact protection in PBS composites[13,39–41]. This limits the selection of optimal PBS synthesis parameters for effective shock absorption. Thus, establishing a correlation between the density of dynamic crosslinks and impact absorption will help to direct the focus in the right direction. Another unknown question is the origin of dynamic crosslinking in PBS, which has been debated in the literature for over seventy years[29,42,43] due to the complexity of the chemistry of boron dynamic interactions[38,44,45]. The answer may make it possible to improve / reduce the cost of PBS production technology, as well as to maximize the protective properties.

1.2 Objectives and Scope

This thesis aims to reveal details on the mechanism of low-velocity impact absorption in the two most promising shear stiffening materials: fumed silica/polypropylene glycol (PPG) suspension from the STF side and polyborosiloxane (PBS) from the SSG side. More specifically:

(1) find out the possibility of jamming transition during low-velocity impact and how it contributes to the impact absorption in fumed silica-based STF;
(2) correlate the density of dynamic crosslinking with the viscoelastic properties and impact absorption in PBS;
(3) assess the effect of bi-/tri-/tetra-functional boron dynamic crosslinking on the mechanical properties as well as reveal details on the origin of dynamic crosslinking in PBS polymer.

1.3 Dissertation Overview

This thesis aims to evaluate the potential of shears-stiffening materials for low-velocity impact protection as well as to resolve the disputes over mechanisms that would provide

valuable insights on how it can be improved.

Chapter 1 introduces the background of the protective materials against low-velocity impact, such as one finds in sports, overviews emerged “smart” (namely, shear-stiffening) materials to overcome drawbacks of preexisted solutions. After that, the remaining challenges of “smart” materials are formulated, followed by objectives and scope, an overview of the entire thesis, outcomes, and novelties.

Chapter 2 reviews the literature concerning shear-stiffening materials: existing types (STF and SSG), their most promising candidates, their applications in the field of impact protection, proposed explanations for stiffening mechanisms, factors affecting stiffening performance, and how it contributes to impact absorption. Besides, knowledge gaps in the field are described and justified.

Chapter 3 discusses the experimental methodology and basic principles of characterization techniques used in this thesis. Specifically, description of the working principles of the employed characterization techniques in the context of the project's objectives.

Chapter 4 presents a major set of results on the impact absorption mechanism in fumed silica/polypropylene glycol suspension. Optical in situ speed recording of flow field during low-velocity impact demonstrated new evidence of shear-activated jamming, supported by the flow and extensional rheological analysis. Furthermore, the mechanism of impact absorption in this type of STF is discussed with the emphasis on how shear jamming contributes to impact protective properties (reduction of peak force, distribution of impact over area and thickness, etc.).

Chapter 5 establishes links between the synthesized PBSs and various mechanical properties, particularly the viscoelastic properties of the resulting gels and their protective properties. The molecular weight (MW) of the precursor, which was found directly connected to the density of the supramolecular network, is used as a varying parameter. Correlations are established between the precursor MW, crossover point (CP) modulus, and normal peak forces generated in response to low-velocity impacts. Infrared spectra (IR) and oscillatory test data of synthesized PBSs have been interpreted in relation to the shear-stiffening mechanism. The mechanism of impact absorption in PBS is discussed with particular attention to the contribution of the shear-stiffening effect.

Chapter 6 provides insights into the mechanism of dynamic crosslinking in PBS, which

has been debated for 70 years. The dynamic covalent bonding through substitution of oxygen atom in Si-O-B covalent bonds with the oxygen of silanol groups is demonstrated to be the origin of PBS gelation and its unique viscoelastic properties. The formation and breakage of Si-O-B bonds have a low energy barrier; therefore, they can be easily formed and exchanged at room temperature. Viscoelastic properties can be tuned by the right choice of boron functionality, which results in n-functional dynamic covalent bonds (-Si-O)$_n$-B. FTIR, ^{13}B-NMR, MALDI-ToF-MS analyses. Additionally, synthesis kinetic studies were utilized to support the findings.

Chapter 7 concludes the finding of three results chapters, including (1) in situ observation of jamming front propagation during low-velocity impact in polypropylene glycol/fumed silica STF and how it contributes to impact dissipation; (2) correlations between the molecular weight of precursor and mechanical properties in polyborosiloxane (PBS) with particular attention to impact absorption; (3) Mechanism of multifunctional dynamic crosslinking in PBS. The potential of STF and SSG to replace conventional protective materials is discussed with ideas about their composites as bulk protection.

1.4 Findings and Outcomes

Several findings and outcomes are reported in this thesis with an emphasis on novelty. They are arranged according to the objectives stated earlier.

The following findings were discovered regarding the first objective (1):

- Discontinuous shear thickening (DST) is present at as low as $\phi = 7.2\%$ fumed silica volume fraction and onwards, a prerequisite for jamming. This fact confirms results from another study[46] where the DST threshold ϕ_{DST} for hydrophilic fumed silica suspensions was found to be around 6%. The presence of DST is important as it is a prerequisite for shear jamming (SJ).
- Analysis of the flow field during impact reveals jamming at $\phi \cong 7.2\%$ and onwards. The possibility of jamming at such low concentrations is shown for the first time in the literature.
- The front propagation speed at $\phi > 7.2\%$ is 3-5 times higher than the speed of the impactor rod, which rules out jamming by densification, and confirms that the

propagation is triggered by shear. This fact agrees with those reported by Naald et al.[47]; however, in our work, it is shown for much smaller ϕ.

- The main impact absorption begins when the jamming front reaches the boundary, creating a solid-like plug under the rod that confronts its movement. The efficiency of impact absorption depends on fumed silica fraction through the thickness of the front between the rod and the bottom. This is a novel insight into the mechanism of impact absorption which clarifies the requirements for the design of impact-resistant composites based on STF.

Achieving the second objective (2) resulted in the following findings and novel correlations:

- With the aid of IR characterization paired with gas-permeation chromatography (GPC), we demonstrated that the number of dynamic crosslinks in PBS (represented by the intensity of the Si-O-B band) corresponds to the number of hydroxy groups in precursor PDMS. This discovery confirms the completion of the reaction without chains scissoring, permanent crosslinking, or polymerization. Therefore, chosen synthesis routine allows for precise control of the outcomes of the resulted PBS.
- Crossover point modulus (which represents the stiffness at the point of liquid/solid transition) of PBS is in a linear relationship with the number of precursor hydroxy groups, hence, the number of dynamic crosslinks. Normal peak forces generated in PBS and energy absorption during the low-velocity impact test demonstrated a linear increase with the number of dynamic crosslinks. These novel correlations provide guidelines to tailor the mechanical response of PBS for shock energy dissipation, dampers, sensors etc.
- The efficiency of impact absorption is defined by the stiffness of PBS (when all dynamic crosslinks “lock” due to the inability to relax) together with the required energy to break all dynamic bonds depending on the impact energy. This provides clear guidance to focus on dynamic crosslinking density for the improvement of energy absorption in PBS.

Out of objective (3), the following findings were discovered:

- Dynamic covalent bonding through B-O ligand exchange is shown to be the most probable mechanism behind the unique viscoelastic properties of PBS. The same

mechanism is involved in initial gelation as well as dynamic exchange. The oxygen atom in Si-O-B bonds undergoes rapid associative exchange with oxygens hydroxyl bearing moieties (free silanol, alcohol, water). The formation/exchange of Si-O-B bonds has a low energy barrier that makes them easy to form (even at room temperature) and vulnerable to break (during hydrolysis or with the addition of -OH-bearing molecules). This solves the long-lasting debate on the mechanism which allows simplifying and improving the synthesis path of PBS.

- Dynamic crosslinking does not involve hydrogen bonding, dative bonding or formation/exchange of boron anhydrides but is solely the result of associative dynamic exchange of Si-O-B covalent bonds.
- The Viscoelastic properties of PBS largely depend on the B-O functionality of the boron compound. Tetrafunctional boron crosslinker demonstrated the highest rubbery plateau, which confirms the highest number of dynamic bonds, followed by trifunctional boric acid. In contrast, bifunctional phenylboronic acid provided only chain extension without any signs of gelation. Therefore, mechanical properties could be tuned by the right choice of boron functionality, resulting in n-functional dynamic covalent bonds $(\text{-Si-O})_n\text{-B}$.

Chapter 2

Literature Review

This chapter reviews the literature concerning shear-stiffening materials: the most promising representatives of STF and SSG for impact protection (fumed silica-based STF and polyborosiloxane), factors affecting their stiffening performance, existing protective composites based on them, and proposed theories on their stiffening mechanisms. Special attention is given to research on the mechanisms of low-velocity impact absorption with remaining knowledge gaps.

2.1. Shear-stiffening materials

Shear-stiffening is a unique effect when modulus or viscosity increases with an increase in shear deformation rate. Such behavior can be observed in some types of supramolecular polymers and suspensions.[13] This type of material is called shear-stiffening materials. They stiffen in response to external stimuli once the threshold deformation rate is exceeded. Another distinctive feature of these materials is that the transition from liquid to solid (or highly viscous) state is reversible; hence, they return to the original liquid state upon removal of external stress[15–17]. Even though these materials were discovered decades ago, they have recently attracted renewed attention in the field of protective equipment[12,13]. During the liquid/solid transition, a significant amount of energy can be absorbed or contribute to shock absorption through indirect processes (increase in friction between yarns, creating a jammed solid plug, etc.). However, applications will depend on a time scale of impact; for example, these materials will behave differently under low-velocity impacts such as in sports compared to high-velocity projectile impacts. Factors to be considered when choosing shear-stiffening materials for a particular protective application: deformation rates during impact, impact area size, and predominant direction of impact (how much shear stress versus tensile/compression). There are two common types of shear-stiffening materials with different stiffening mechanisms. Still, both provide similar advantages in impact absorption: shear thickening fluids (STF) and shear-stiffening gels (Figure 2.1).

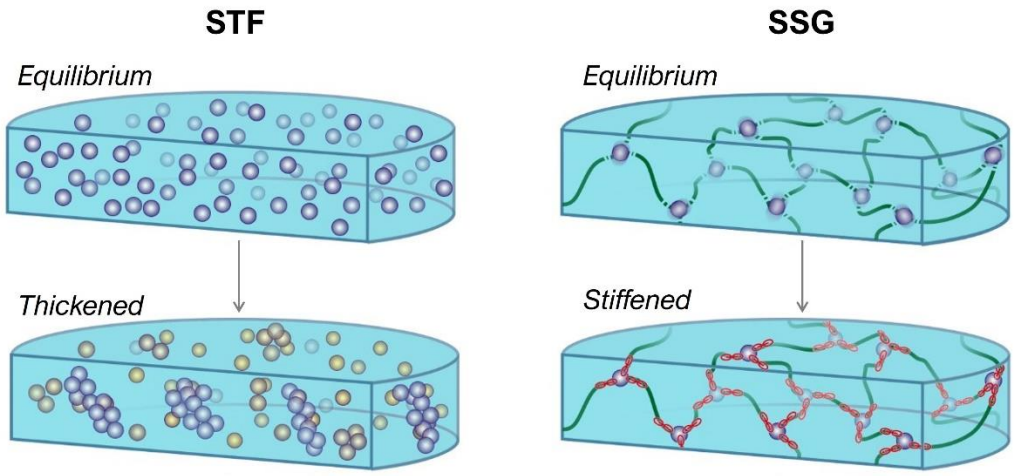

Figure 2.1 Shear thickening fluid (STF) in the equilibrium state when particles are well-dispersed and thickened state when particles are forced into contact with each other (on the left). Shear-stiffening gel (SSG) in the equilibrium state when dynamic crosslinks can travel in the bulk and stiffened state when they "lock", which results in a solid behavior (on the right).

Shear thickening fluids (STF) are dense suspensions of solid particles in the liquid medium which possess non-Newtonian properties; specifically, the viscosity increases with an increase in shear rate[12]. The thickening behavior arises from the particle-particle (via friction) and particle-medium interactions (hydrodynamic forces)[48]. This unique feature makes STF a "smart" material that allows use in various protective applications.

Shear-stiffening gel is the second class of "smart" materials which is, in contrast to STF, a supramolecular polymer system[13,49]. The liquid/solid transition originates from dynamic supramolecular bonds; at a lower deformation rate, they relax and reconnect (the material flows like a liquid), but once the transition rate is exceeded, these bonds "lock" and behave as permanent crosslinks (the material behaves as an elastic rubber)[17,31,50]. Some of the STF and SSG protective applications will be discussed next.

2.1.1 STF composites for impact absorption

The first attempt to unitize STF for impact protection devices was made by Gates in 1968[51] however, for over three decades, no more studies were published. In 2004

unique properties of STF were reexplored for body armor, and the U.S. Army Research Laboratory (ARL), in collaboration with the University of Delaware, filed the patent [19]. The main approach was to impregnate a fabric material (Kevlar in their case) with an STF diluted in alcohol and then dry (Figure 2.2). After this patent, many works were published devoted to the impregnation and testing of various fabrics for ballistic, stabbing, and cutting resistance[52–58]. Other high-performance fabrics were tried together with STF, such as Ultra High Molecular Weight Polyethylene (UHMWPE), Twaron, and Spectra, and their performance was assessed [59,60]. As it turned out, the reason why these characteristics are significantly improved is a significant increase in friction between the fibers, which reduces the likelihood of a windowing effect (the main drawback of all fabrics in the field of protection)[12,61].

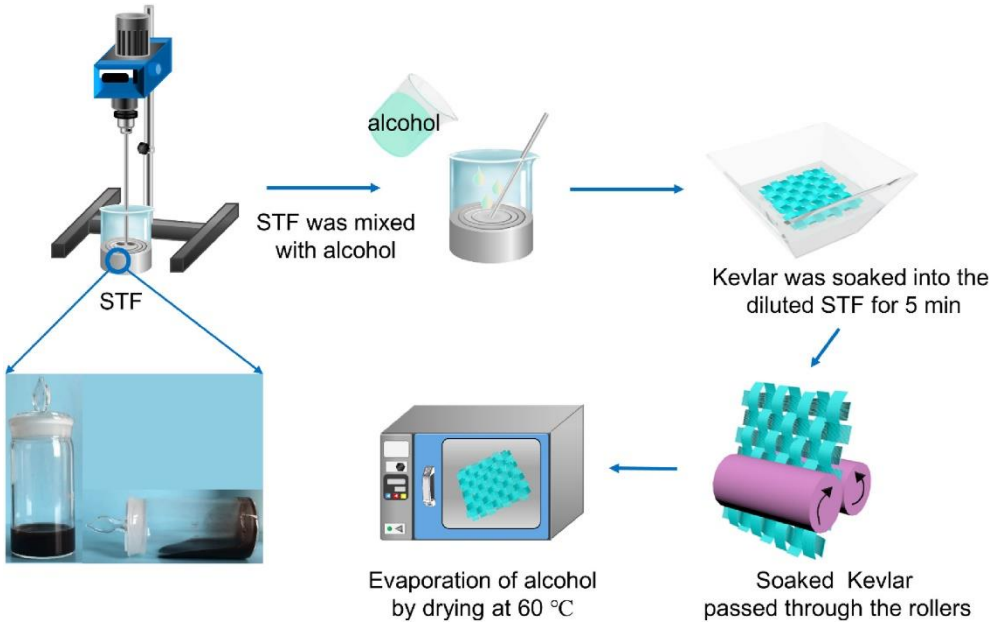

Figure 2.2 General preparation routine of STF/Kevlar composites for bullet-proof protection. Reproduced with permission.[62] Copyright 2022, Elsevier.

Other impact protective composites include: steel plate backed with an STF impregnated open-cell polyurethane (PU) foam which was designed to protect against standard blast load[63], composite which was produced by in situ formation of closed-cell PU foams with STF which was also used as an approach to encapsulate STF[64], an ecofriendly composite made by engraving micro-agglomerated cork sheets with

various microfluidic patterns and filling them with STF[65], STF-filled sandwich composite panels with carbon fiber reinforced plastic facings[66], PU skeleton (with cubic holes in it) filled with STF sandwich composite[67,68], composites where STF is intercalated in a spacer fabric and incapsulated in a polyethylene (PE) copolymer shell for a football helmet padding[69].

One of the biggest challenges in using STF for protective gear is its flowability; if the composites are not completely sealed, STF will eventually leak out. Therefore, some researchers tried to develop encapsulation approaches to overcome this challenge, such as applying calcium alginate in an orifice coagulation bath[70] or enclosing the material in a polyurea shell in a precursor solution[71].

2.1.2 SSG composites for impact absorption

Shear-stiffening behavior is observed in some soft biological polymer materials, targeted to prevent damage to biosystems at dangerously excessive deformations[72]. Similar behavior was discovered in synthetic polymer network gels. The stiffening of their networks in response to deformation/deformation rate arises from the physical nature of their crosslinks[73]. Based on that principle, various shear-stiffening hydrogels were developed to mimic biological materials and their ability to stiffen in the body[74–76]. One particular example of shear-stiffening hydrogel is the polyvinyl alcohol (PVA) slime. It is well-known material from a classic school experiment where a solution of PVA in water is mixed with a solution of borax in water, resulting in an instant formation of slime. It was used as an example of how physical crosslinking can provide strong enough interactions to solidify water solution[77]. This type of hydrogel demonstrates an increase in elastic modulus with an increase in shear deformation rate as well as liquid/solid transition in oscillatory shear experiments (at a loss/storage modules curves crossover)[78,79]. Yet, shear-stiffening hydrogels suffer a few drawbacks because of their aqueous nature, making them difficult to use for impact protective gear. For instance, they exhibit limited mechanical strength, loss of properties over time due to water evaporation, and dependence on external conditions (humidity, pH, temperature, etc.)[80].

A water-free and boron-containing SSG gained significant interest in the field of protective composites – polyborosiloxane (PBS). PBS is known as the main compound of Silly Putty™ – a gel-like toy popular among children for its bouncy yet stretchable properties. Its dynamic properties come from a physical crosslinking of siloxane chains with boron-containing compounds (typically, boric acid)[13]. The exact mechanism of stiffening in PBS will be discussed further.

Most PBS applications in the field of impact protection are connected to foams where PBS acts as a filler in the bulk of foam. Typically, polyurethane foam is used as a matrix, such as in a study by Xiaoke et al.[81] where PBS is premixed with component A (polyol premixed with all necessary components such as cross-linker, blowing agent, catalyst, etc.), then this mixture is added to isocyanate with subsequent mixing for a short while. After the mixture is poured into a mold, a "smart" foam is formed (Figure 2.3).

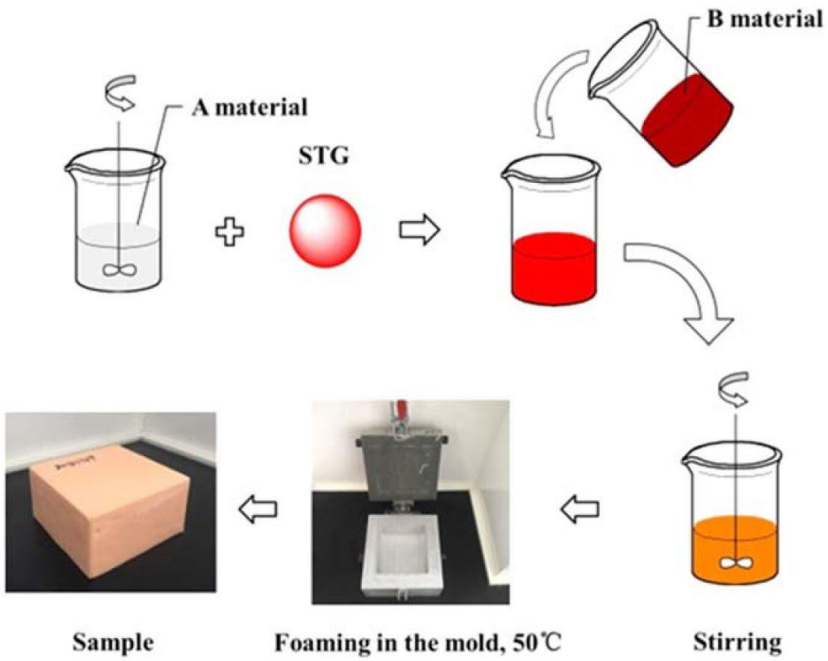

Figure 2.3 Preparation procedure of PU foam-based composite with PBS. Material A is polyol; material B is isocyanate. Reprinted with permission from ref [81]. © IOP Publications.

This approach was used in a variety of patents in the field of sports protection. Two companies were established based on the patents with a similar idea: D3O[21] and

Armorgel[22] which achieved commercial success in the area of "smart" protective gear. After the formation of the "smart' PU foam in the mold, PBS stays enclosed in the foam, providing additional impact absorption on top of the foam cushioning.

Another approach to making a "smart" foam is a dip and dry method where pre-produced open-cell foams are used. Wang et al.[82] used commercially available polyurethane open-cell sponge as a matrix. PBS mixed with BPO in acetone was dipped in a sponge, followed by drying in the vacuum oven to remove acetone, this procedure was repeated to reach saturation. After that, the impregnated foam was cross-linked with BPO in the oven for 2 hours (Figure 2.4).

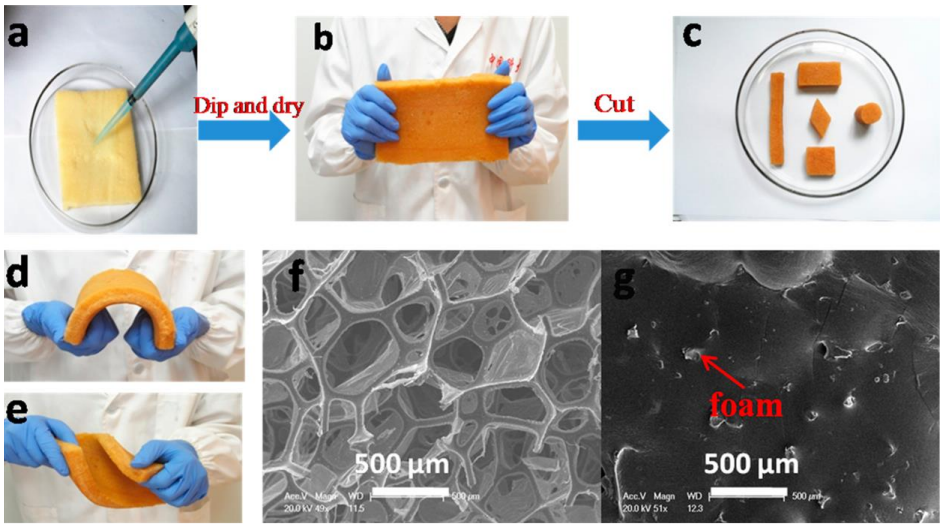

Figure 2.4 General preparation routine of PBS impregnated open-cell PU foam composite. Reprinted with permission from ref [82]. © ACS Publications.

Other composites design approaches were utilized to maximize the contribution of PBS to energy absorption. Xu et al.[40] used silly putty as a core material for Kevlar composite. Silly putty was locked in a sandwich structure where the bottom and the top layer of Kevlar fabric were stitched together. To improve the self-stiffening effect, $CaCO_3$ particles were dispersed inside silly putty. In the ballistic test, composite showed 60% higher energy dissipation than neat Kevlar. He et al.[20] prepared a composite of STF impregnated Kevlar fabric with PBS using the "dip and dry" method. Significant enhancements were demonstrated in terms of rod penetration resistance, knife cutting resistance, yarn pull-out test, and split-Hopkinson bar test. A similar

approach was used by Zhao et al.[41] where they prepared multilayer Kevlar composites that were impregnated with PBS using the dissolution-volatilization method.

2.2 Shear thickening fluids

Shear thickening fluid (STF) is a type of colloidal suspension that possesses a non-Newtonian behavior under shear deformation. More specifically, it is a dilatant, where its apparent viscosity increases beyond a critical shear rate. The shear thickening phenomenon exhibited is reversible, meaning the material returns to its initial liquid state upon removal of the applied stress[18]. Typical STF forms stable suspension due to steric, electrostatic, or Brownian interactions[83].

2.2.1 Mechanism of shear thickening in STF

Initially, the order-disorder theory was believed to explain the increase in viscosity during the shear thickening phase. Hoffman's work[84] was a pioneer study on the explanation of the shear thickening mechanism. In this work, the shear thickening fluid was proposed to act opposite to shear-thinning fluid since they are opposite in rheological properties. It was believed that at the critical shear rate, the transition from order (in a colloid suspension) to disorder happens and causes a significant increase in viscosity. Later some discrepancies were found, and a new model was proposed. Bossis et al.[83] proposed that hydrodynamic force is the main cause of the shear thickening effect. Before the critical shear rate, particle-particle interactions are repulsive (because of electrostatic, Brownian, or any other forces), and the suspension is stable. After the onset is reached, the hydrodynamic forces dominate over repulsive forces, and the particles aggregate into so-called hydroclusters. The reduced mobility of particles (due to association in hydroclusters as well as the subsequent increase in hydrodynamic resistance) causes drastic viscosity growth. However, it was found that pressure created by hydrodynamic forces is not enough to overcome repulsion forces to form clusters.

The mechanism of shear thickening was recently re-explained using contact rheology model[16,85–88] after reconsidering the old explanation by hydrodynamic model[83]. It was found that pressure created by hydrodynamic forces is not enough to overcome repulsion forces to form clusters. The contact rheology model suggests that the main contribution to the shear thickening is due to particle-particle interactions, not the particle-medium ones. After reconsideration, two types of shear thickening were introduced[18]: continues shear thickening (CST), which is a weak type of shear thickening mainly driven by hydrodynamic forces, and discontinues shear thickening (DST), which results in a discontinuous jump in shear stress beyond a critical shear rate due to contact forces between particles. A relatively new concept of jamming by shear (SJ) was introduced as an extreme behavior of DST suspensions below jamming particles' fraction ϕ_J for a range of suspensions with sufficiently strong frictional interactions[16] (Figure 2.5). SJ is a reversible transition of unjammed dense suspension to a solid-like state with finite yield stress induced by shear[89–91].

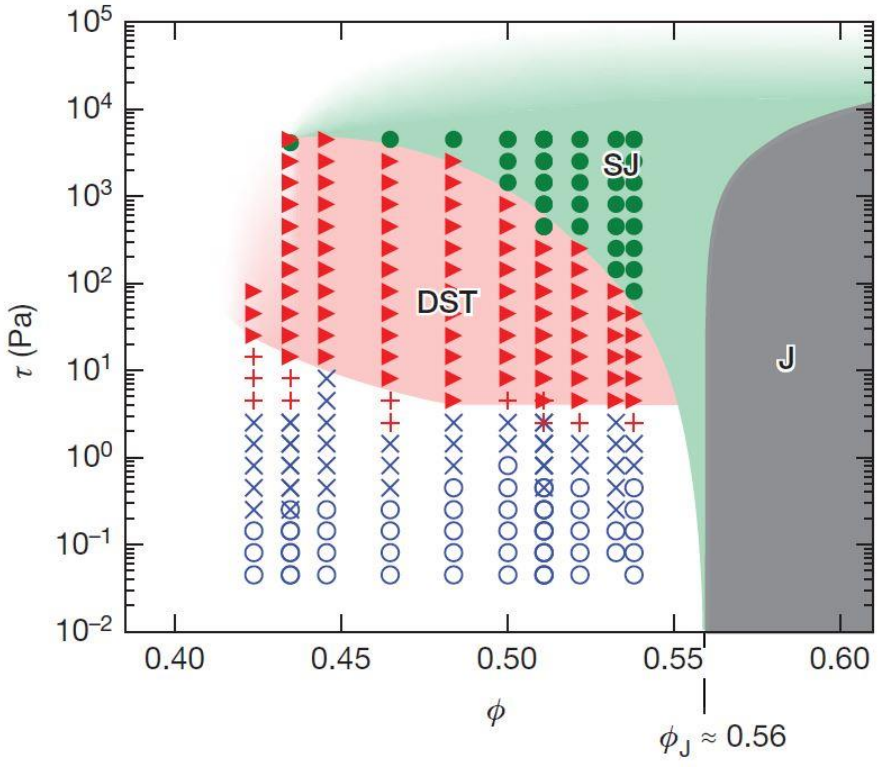

Figure 2.5 State diagram of different states of STF with isotropic particles: blue circles – shear thinning regime, blue crosses – Newtonian flow, red crosses – continues shear thickening, red

triangles – discontinues shear thickening and green dots – shear-jammed. Reprinted with permission from ref.[16] © Copyrights 2016, Springer Publishing.

Sliding and rolling friction between particles are among the main contributors to the DST and SJ[92]. Manipulation with the surface roughness[93], aspect ratio [94], adhesion[95], and chemistry[96] was shown to allow to tune the thickening, as well as to shift the onset. However, surface chemistry (hydrogen bonds, in particular) was found to be essential for DST and SJ, where surface roughness cannot lead to DST alone[46,96].

2.2.2 Effect of different factors on rheological properties of STF

Many researchers tried to manipulate the rheology of STF to improve the strength of shear thickening or to shift the onset by changing various parameters. The viscosity of STF can increase by a few orders in magnitude depending on particle fraction concentration, particle surface chemistry, particle aspect ratio, size, chemical structure, and molecular weight of the liquid medium[12,47,97–99].

Rheological properties of STF could exhibit systematic variations based on a few key characteristics: critical shear rate (CSR) is the onset value of shear thickening, shear thickening ratio (STR) is the ratio between the highest viscosity and the viscosity at the onset which defines the magnitude of thickening, viscosity at the critical shear rate (VCSR) and maximum viscosity (MV). The typical rheological curve of STF is shown in Figure 2.6. These parameters will be used to examine the effect of different factors on thickening performance. Some of these conclusions are intuitively understandable based on general logic.

It was calculated that for a dense suspension of perfectly spherical particles, weak shear thickening started to be observed from 0.4 particles volume fraction ϕ, where $\phi = 0.56$ is optimal for a strong shear-thickening[100]. Higher ϕ increases the probability of contacts and, hence, lowers CSR to trigger shear thickening [101]. With an increase in ϕ STR increases and both VCSR and MV, respectively[12].

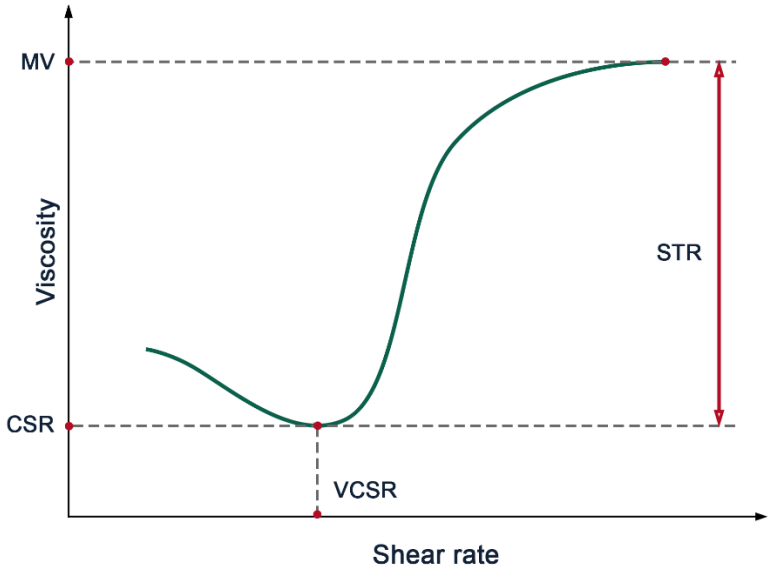

Figure 2.6 The typical rheological curve of STF. CSR is critical shear rate, STR – shear thickening ratio, VCSR – viscosity at the critical shear rate, MV – maximum viscosity.

Based on previous studies, it was found that CSR decreases with an increase in particle size[102,103]. This is because, for bigger particles, Brownian stresses are lower; hence, it is easier to overcome repulsive forces between particles, and thickening occurs at lower shear stresses[102]. Also, with smaller particle sizes, overall viscosity (including VCSR) increases due to more dense packing of particles, hence, a higher density of inter-particle bonding[12].

Properties of the liquid medium also play an important role in shear thickening. Normally polar organic liquids are used as a medium, such as ethylene glycol, small molecular weight PPG, and PEG. Two factors define the shear thickening efficiency – molecular weight and chemical composition. Based on numbers of studies[104,105] CSR decreases with an increase in MW of the polymer medium, and stronger shear thickening is observed in general (in terms of both MV and STR). This is because, with higher MW, absorption of polymer on the particles is enhanced through polar silanol-polymer interactions. Chemical composition is also an important characteristic; based on research[101], PPG demonstrated higher STR and lower CSR compared to the same molecular weight PEG (400). The reason is the higher thickness of the solvation layer in the case of PPG because of a higher degree of polymerization.

Particles aspect ratio plays an important role in shear thickening performance. Based on a study by Beazley et al.[106] particles with a higher aspect ratio cause stronger shear thickening due to particles interlocking, which reduces their degrees of freedom in the flow field. Rod particles are the most efficient among others, then followed by plates, grains, and spherical, respectively[107] (Figure 2.7). It was found that the same magnitude of shear thickening can be achieved with much lower loadings when high aspect ratio particles are used[108]. For example, for a fumed silica STF, shear thickening is observed at as low as $\phi = 0.07$[109]. Fumed silica is known to possess a high aspect ratio due to the production process where nanosized particles fuse together, forming rods that, at extremely high temperatures, grow into aggregates of a few µm.

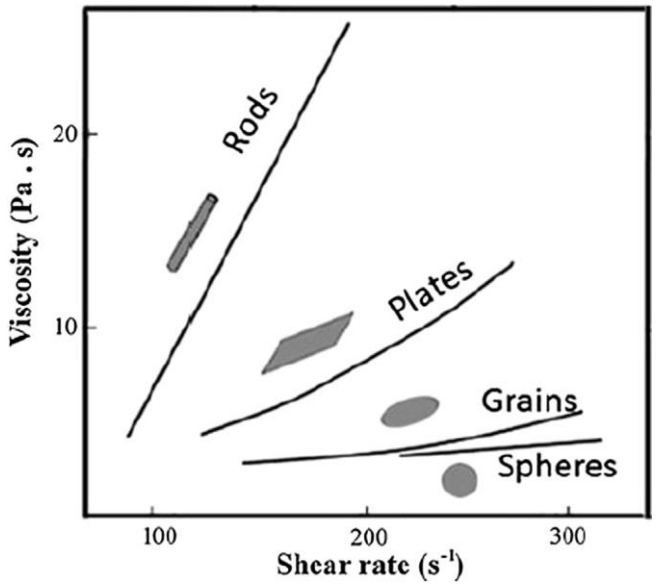

Figure 2.7 Effect of particle aspect ratio on the shear thickening strength. Reprinted with permission from ref [107]. © AIP Publishing.

2.2.3 Fumed silica-based STF

Fumed silica STF is a preferable choice for many applications due to its lower weight per unit volume and high colloid stability. Fumed silica is produced from pyrolyzing tetrachlorosilanes in a hydrogen-oxygen flame, forming primary particles (5-30 nm) that cool to form silica aggregates (100-500 nm) (Figure 2.8). This gives it a fluffy

white appearance characterized by extremely low bulk density (20-50 g/L), high surface area (125-200 m^2/g), and high aspect ratio[110]. The large surface area of fumed silica is dominated by the presence of silanol groups that are prone to form hydrogen bonds. In fumed silica/polar polymer suspensions, the terminal hydroxyl bonds, as well as internal oxygen atoms on the PPG chains, form hydrogen bonds with the abundant surface silanol groups on fumed silica. The interaction surface between PPG and fumed silica acts as a solvation layer that hinders the interaction between fumed silica particles, hence, stabilizing the dispersion of fumed silica in the suspension[111]. Flow rheology of fumed silica STF has been broadly studied in literature[12,16,111–114]. However, little attention has been given to the nature of shear thickening (CST or DST). In a study by Bourrianne et al.[46], CST and DST transitions were found to occur starting from $\phi_{DST} \cong 6\%$ for hydrophilic fumed silica-based STF which is considerably lower than for spherical particles. However, the stresses produced by steady-state rheology are very limited, which makes it hard to achieve and study SJ[115].

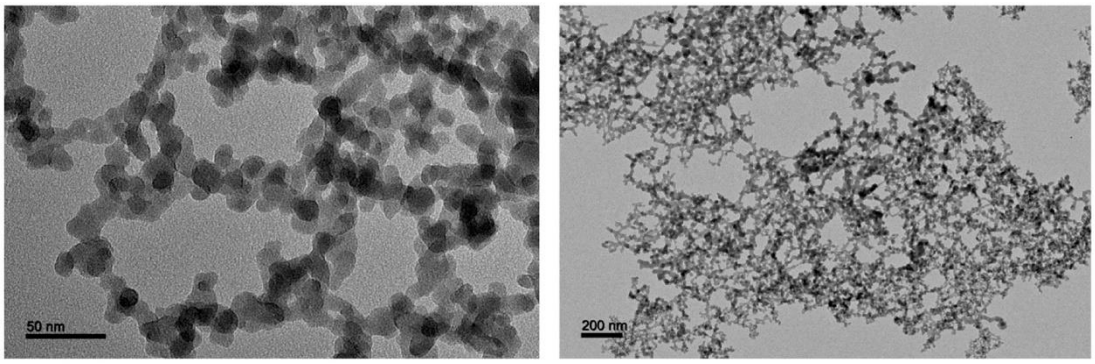

Figure 2.8 TEM images of fumed silica suspended in water. Reprinted with permission from ref.[116] © MDPI Publishing.

As shown earlier[96] interparticle hydrogen bonding can be a source of strong frictional interaction, which may lead to SJ in dense suspensions. Since fumed silica surface is silanol rich with a high area, it suggests that it may possess shear jamming behavior at high concentrations/stresses. The evidence of SJ in fumed silica suspension was provided by Naald et al.[47]: they observed it during impact using high-speed ultrasound imaging. They found that SJ was achieved only at the intermediate molecular weights

of PEG due to the optimal thickness of the solvation layer, which allows forming frictional contact networks rather than lubricated contacts.

2.2.4 Impact absorption in STF

Unique shear thickening properties of STF have found applications in the protective field, from sports protective equipment to flexible body armor[12]. With progress in the development of STF protective composites, some researchers were trying to understand how shear thickening and shear jamming contributes to impact absorption. It was especially interesting considering that STF can support the body weight of the person running across it[18]. The origin of such large positive normal stresses generated during impact has been debated for many years. Two mechanisms were proposed: jamming by densification[66,117,118] and by shear[119–123], where the second requires sufficiently strong frictional interactions between particles such as via hydrogen bonding[96]. Both mechanisms suggest that the jamming of particles is the cause of high normal forces, which act in the opposite direction of the impact load. In the study by Waitukaitis et al.[118] they demonstrate that high normal stresses in cornstarch water suspension arise from the formation of the densification front beneath the impactor rod using high-speed videography coupled with embedded force sensing X-ray imaging. They also concluded that the growing jamming front itself is the main cause of large normal stresses and that the presence of boundary is not essential for that. This mechanism was supported by Fu et al.[66,117] where the same conclusions were made but in the case of STF consisted of styrene/acrylate copolymer particles in an ethylene glycol medium. On the contrary, another brunch of research has been developing in recent years where the shear strain triggers the rapid growth of the jamming front. After the breakthrough study by Bi et al.[119] where they demonstrated that the shear strain transmitted through the network of force-bearing grains is the trigger of jamming, the same research group who first believed that the jamming is caused by densification[118] changed their opinion and proved that the shear is the cause of jamming during low-velocity impact[16].

Various types of impact were utilized to find the limits and conditions of shear jamming in water cornstarch suspensions[120,121,123]owever, less attention has been paid to more complex STFs such as fumed silica/polymer suspension, which found more use in real-world applications. Despite the study by Naald et al.[47] where they conducted impact tests on a fumed silica STF to reveal the presence of SJ, it remains unclear how jamming transition contributes to impact protection and the mechanism of impact absorption in fumed silica/polymer suspensions.

2.3 Polyborosiloxanes (PBS)

Shear-stiffening gels (SSG) have attracted the attention of many researchers in the last decade due to their unique viscoelastic properties, self-healing ability, ease of synthesis, and affordability of raw materials.[13] As it was mentioned earlier, the most common and utilized SSG is polyborosiloxane (PBS). PBS is a viscoelastic gel that is a result of boron dynamic crosslinking of polydimethylsiloxane (PDMS) chains. There are a few pathways of PBS synthesis, such as via condensation reaction between hydroxy end groups of boric acid (BA) and PDMS,[14,35–37,124,125] boron termination reaction of scissored PDMS pieces[28,31,126] due to random chain scission of PDMS chains at a temperature higher than 150 ºC with the presence of BA as a catalyst,[28,126] or simultaneous polymerization of PDMS with borono ends modification from dichloro dimethyl silane.[127,128] Incorporated boron crosslinks possess sticker-like behavior due to their supramolecular nature. However, the nature of these interactions is still debated in the literature[29,42]. Hypotheses and evidence on the nature of dynamic crosslinking in PBS will be discussed further in detail.

PBS behaves like a viscous liquid at low deformation rates due to the dynamic relaxation of supramolecular bonds (Figure 2.9, a). At this stage, it demonstrates typical cold-flow characteristics, such as the one found in plasticine[13] (Figure 2.9, b). However, once this rate exceeds the critical value, stickers do not have enough time to relax and reconnect; therefore, these temporary connections lock and behave as permanent crosslinking points.[13,32] During this transition, PBS changes its behavior from viscous to rubbery. If the strain rate keeps rising, PBS, eventually, will transit in

a glassy state where the dynamic bonds start to break due to excessive external stresses. At this stage, PBS demonstrates brittle fractures if deformed, such as the ones found in highly crystalline plastics. This behavior is fully reversible even after brittle fracture[17,129].

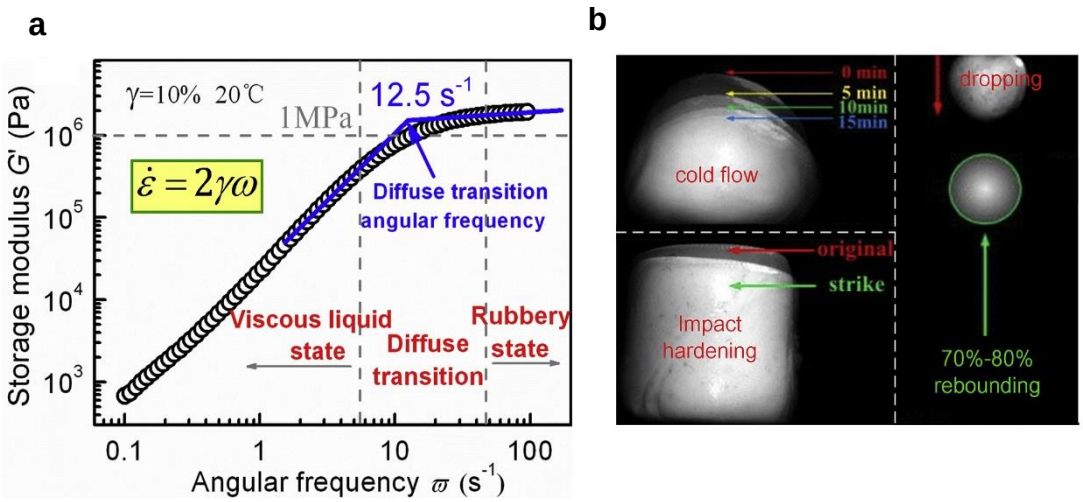

Figure 2.9 (**a**) Storage modulus of SSG as a function of angular frequency with liquid/solid transition. Reprinted with permission from reference[32]. Copyright 2014, American Institute of Physics; (**b**) Cold flow of SSG, impact-induced hardening and with elastic rebound of SSG. Reprinted with permission from reference.[13] Copyright 2022, Elsevier.

2.3.1 Effect of various parameters on viscoelastic properties of PBS

To assess the effect of BA concentration on rheological properties, we need to consider the synthesis pathway. As it was mentioned earlier, there are two main ones, one through direct condensation reaction between hydroxyl groups of BA and HO-PDMS-OH, which can take place even at room temperature[29,43], and another, which does not require the presence of hydroxyl groups in PDMS and happens due to random scissoring of PDMS chains at elevated temperatures (> 150 ºC) and insertion of BA at the scissored sights[28]. In the first case, the maximum effective concentration is reached at the stoichiometric ratio between the BA and PDMS hydroxyl group. Hence, it depends on the molecular weight of PDMS. In this case, gel-like properties start to

appear when 50% of the stoichiometric concertation is achieved. At lower concentrations, only viscous liquids are produced. Therefore, in the first synthesis scenario, elasticity gradually increases from 50% to 100% of stochiometric saturation[29]. Generally, an excessive amount of BA (above stoichiometric saturation) does not affect the viscoelastic properties but may lead to the formation of boroxines (BA anhydrides) or other boron complexes, which can reduce the mobility of dynamic bonds.

If the second synthesis route is used, the effect of BA concentration is different. In each individual case, stoichiometric saturation concentration would be different and depends on the degree of chain cleavage. For instance, higher temperature and longer reaction time would promote more serious chain scissoring, which means higher stoichiometric saturation concentration. This would lead to a higher density of dynamic crosslinks overall, hence, more elastic properties. Another factor is that BA acts as a catalyst on its own, promoting more dramatic chain scissoring at higher concentrations.

Another very important factor affecting the properties of PBS is the molecular weight of PDMS. Molecular weight defines the number of dynamic crosslinks, hence, the density of supramolecular mesh. BA end modification of shorter chains results in a stronger shear-stiffening effect. However, the relationship between molecular weight and rheological properties is not as straightforward as it seems. Tang et al.[130] assessed the effect of molecular weight of hydroxy-terminated PDMS on a resulting rheological property of PBS. They found that plateau elastic moduli first decreased and then increased with the molecular weight of the precursor due to a decrease in the number density of supramolecular interactions and dominance of topological entanglements (for molecular weights higher than entanglement molecular weight $M > M_e$). Seerapan et al.[124] demonstrated the same trend, but for a narrower range of PDMS molecular weights, they found that relaxation time decreases with the precursor's molecular weight. Similar conclusions were made by Liu et al.[28] that lower MW of PDMS results in a stiffer polymer with reduced supramolecular mobility.

Various fillers have been used as functional additives to modify the viscoelastic properties of PBS for different applications. Reinforcing fillers, such as $CaCO_3$, were

used to increase storage modulus via the particle enhancement effect[32,40]. Magnetic fillers, such as carbonyl iron particles (CIPs) and Fe_3O_4 particles which, demonstrated improved stiffening performance when the magnetic field is applied[131–134]. And conductive fillers, such as CNTs[39,135,136], carbon black[41,137], Ag nanowires[35,138] and graphene sheets[33,139] for various electronic applications.

2.3.2 Impact absorption in PBS

Due to its unique self-healing and shear-stiffening properties, PBS has found many uses in impact protective applications. Despite the wide range of various PBS composites, the potential of impact absorption of PBS on its own has hardly been studied. This might be due to complications with the molding of PBS for real applications since it flows at low deformation rates. Wang et al.[17] investigated PBS filled with magnetic particles under high strain rates using a modified Split Hopkinson Pressure Bar (SHPB). They found that energy absorption was attributed to two transitions, from liquid to elastic and elastic to glassy (Figure 2.10, a). The transition from the rubbery to the glassy state could be studied only using impact techniques such as weight drop impact tests and SHPB as it happens at rates unachievable by a conventional rheometer. This transition is a result of the simultaneous breakage of many supramolecular interactions.[140,141] It significantly contributes to overall energy absorption when rates exceed the critical value at which supramolecular bonds break.[32,140] In another study, Zhang et al.[14] demonstrated that during a low-velocity weight drop test, the impact area expanded five times when a PBS layer is used, which is the result of the stiffening front formation under impact. Moreover, they observed the formation of cracks which was found to be beneficial for impact absorption (Figure 2.10, b).

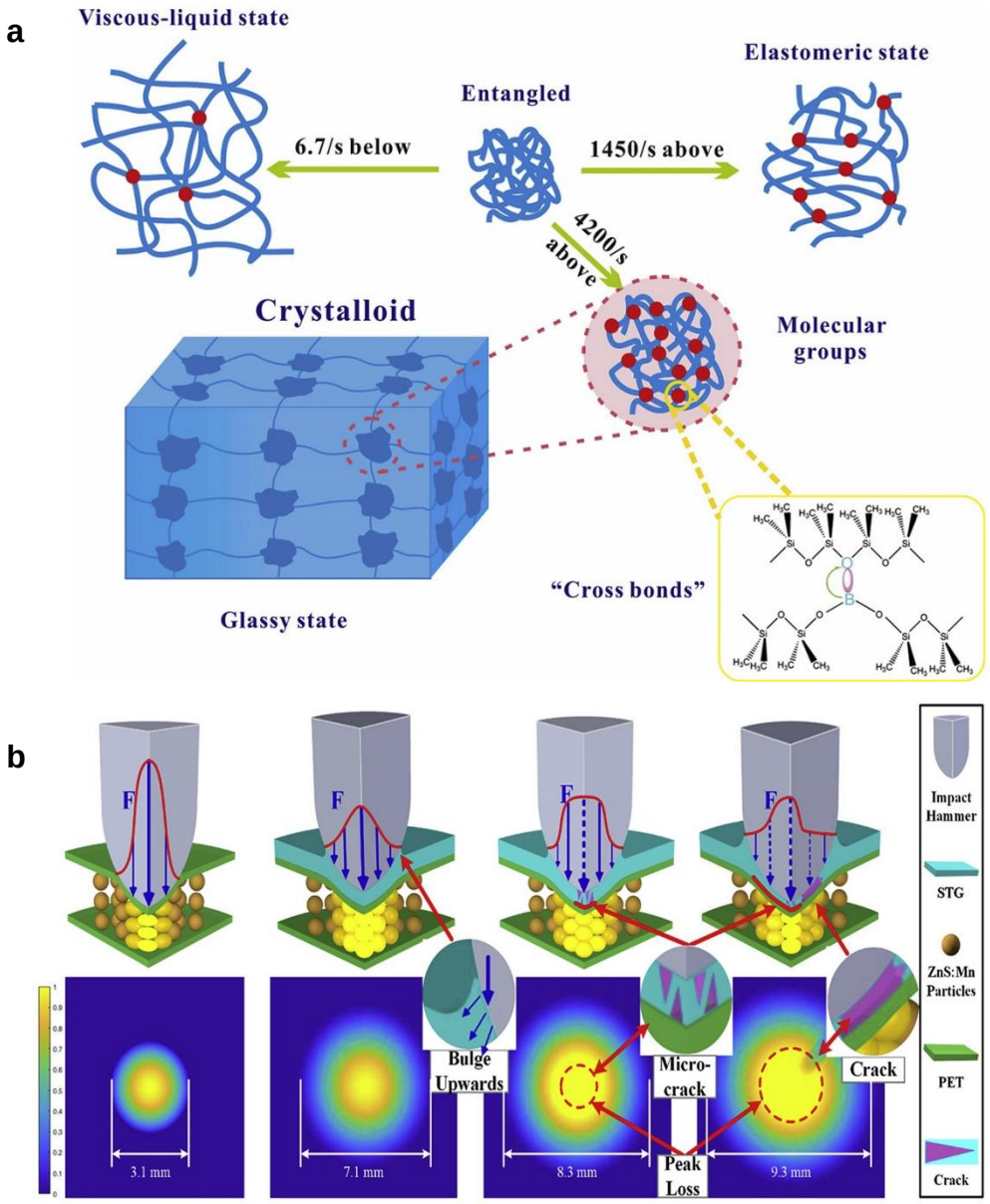

Figure 2.10 (**a**) Illustration of the different states of PBS at different deformation rates. Viscous liquid state at low rates, elastomeric state at intermediate, and glassy states and high strain rates. Reprinted with permission from reference[17]. Copyright 2016, Elsevier; (**b**) Mechanism of impact dissipation which results in expansion of impact area. Reprinted with permission from reference[14]. Copyright 2020, Elsevier.

2.3.3 Mechanism of dynamic crosslinking in PBS

The origin of dynamic crosslinking in PBS was debated for many decades. This material was first synthesized in 1947 by McGregor and Warrick of Corning Inc. [142] However, they have not provided any details on the nature of interactions. Two different explanations appeared simultaneously in 1960, one by Wick[143] and another by Vale[127]. Wick proposed that the dative bonds between the boron atom and the oxygen in the siloxane backbone are the cause of such unique viscoelastic and self-healing behavior (Figure 2.11, a). On the other hand, Vale suggested that the hydrogen bonding between hydroxy terminated borono groups is the main and the only type of supramolecular interaction in PBS (Figure 2.11, b). For many years, it was debated in the literature whether hydrogen or dative bonding is the main contributor to dynamic cross-linking, with some discrepancies on both sides. Not so long ago, another type of dative bonding was suggested to be the dominant interaction in PBS by Zepeda-Velazquez et al.[144] They proposed that dative bonding between oxygen atoms in boric acid end groups and boron atoms (Figure 2.11, c) together with hydrogen bonding are in charge of elastomeric properties in PBS[42]. Recently, another mechanism of dynamic crosslinking was proposed by Bloomfield[29], where he claims that the origins of dynamic properties have been misunderstood for 70 years. He suggested that in PBS, all PDMS chains are covalently bonded through trifunctional boron cross-links like in silicone rubber, but in the case of PBS, these covalent bonds are dynamic. They detach and frequently re-attach through oxygens ligand exchange with silanol groups (Figure 2.11, d). This mechanism resembles well-established dynamic covalent bonding which is observed in boronic esters [45,145,146] which will be discussed further.

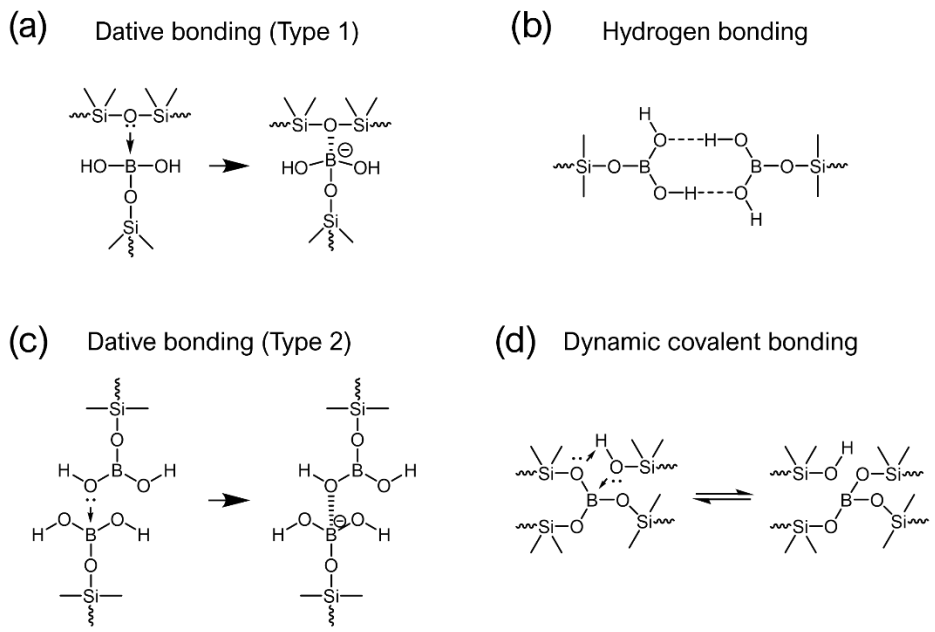

Figure 2.11 Proposed mechanisms of dynamic crosslinking in PBS.

2.3.3.1 Hydrogen bonding in PBS

Hydrogen bonding was one of the first proposed supramolecular interactions to be responsible for the gelation of PBS. It was believed that after the synthesis, PDMS chains become terminated with boron functionality through a single Si-O-B covalent bond, whereas the two remaining hydroxyl groups participate in a hydrogen bonding with other borono modified chains ends (Figure 2.12, a). These borono ends act like stickers detaching and re-attaching endlessly, which results in the ability to flow at longer timescales; however, in one short timetable, they do not have enough time to re-attach, and PBS becomes solid.

Zinchenko et al.[126] conducted a study on the hydrolysis of PBS to reveal details on the mechanism of dynamic crosslinking and molecular microstructure. Hydrogen bonding was believed to be the reason for the unique viscoelastic properties. However, this study was rather focused on the microstructure of the resulted PBS chains than on the mechanism. With the aid of IR spectroscopy and proton NMR, they have shown that the formation of the Si-O-B band (1340 cm-1) goes along with the disappearance of

Si-OH bands (3700 cm^{-1}) which confirms the condensation pathway of the reaction between silanol and boron hydroxyl groups. The presence of the B-O-B band (1380 cm-1) was due to the partial crystallization of BA into boron anhydrite (boroxine), also bound (3250 cm-1) and free B-O-H (3650 cm-1) bands were observed. However, we need to point out that obtained IR data was off 1% PBS solution in CCl_4, not a pure PBS. Partial hydrolysis in moist air revealed the disappearance of the B-O-B bond (probably conversion of boroxines into BA) and the appearance of Si-OH back, but, interestingly, the Si-O-B band remained preserved. After complete hydrolysis in solution with water complete loss of boron (hence, full conversion of Si-O-B bond into Si-OH) was observed. Based on an analysis of MW, boron content, and -OH groups content, they suggested that there is a significant amount of cyclic PBS molecules together with ortho- and meta-borates $(\sim SiO)_3B$ and $(\sim SiO)_3B_3O_3$ respectively (Figure 2.12).

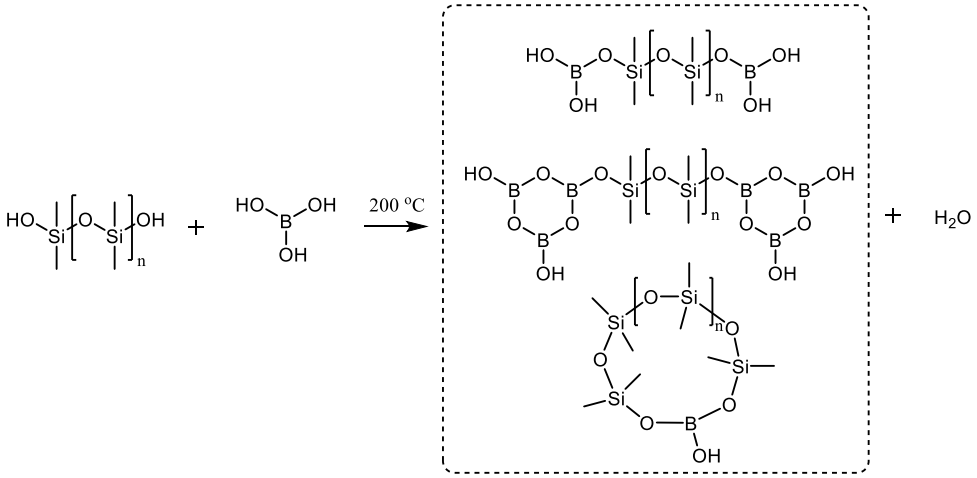

Figure 2.12 Proposed molecular structure of PBS through condensation synthesis at 200 ºC, the scheme is developed based on the reaction described by Zinechenko.[126] From the top to the bottom: linear borono-terminated (ortho-borate), linear boroxine terminated (meta-borate), and cyclic molecules.

In a more recent study[28], they supported Zinchenko's hypothesis of dynamic crosslinking through hydrogen bonding. They also showed that at a temperature higher than 150 ºC PDMS undergoes random chain scission (with the Kuhn chain length

distribution), and borono groups are being inserted at the scissored sights. On top of that, they suggested that upon dehydration, PBS starts to form trifunctional non-dynamic crosslinks via boroxine formation, which gave rise to an additional time scale on a storage modulus curve. Letting synthesized PBS rest at ambient humidity leads to hydrolysis of present boroxines into borono ends Si-O-$B(OH)_2$ with a release of excess BA (Figure 2.13); after a few cycles of filtration, no more BA residues were observed. These borono ends dynamically interact with each other through hydrogen bonding which explains the unique viscoelastic properties of PBS.

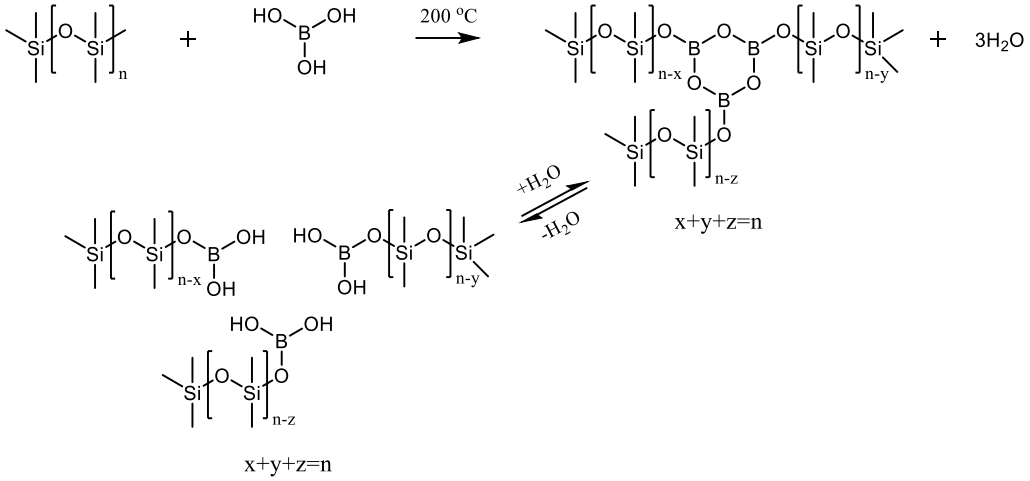

Figure 2.13 Reactants and synthesis outcomes of PBS; the scheme is developed based on the reaction described in a study by Liu[28]. They observed the formation of boroxine molecules which hydrolyze into borono-terminated molecules when equilibrated with air humidity.

2.3.3.2 Dative bonding in PBS

Dative bonding is the second type of interaction that was used in literature along with hydrogen bonding for many years as an alternative explanation for unique viscoelasticity in PBS. It is known that boronic acid can change its hybridization from sp^2 to sp^3 upon interaction with a strong nucleophile due to a vacant p-orbital of the boron atom[38,44,45]. Thus, boronic acid becomes anionic 4-coordinate species which allows it to form a fourth additional bond of dative nature with a nucleophile. This fact is behind the hypothesis that in PBS borono end group can establish reversible

interactions between boron atom Lewis's base atom (such as oxygen), which results in a sticker-like. Two types of dative bonding were proposed to be the main supramolecular interaction. One is between the boron atom and oxygen of the Si-O-Si group (Type 1), and another proposed more recently between the boron atom and oxygen of the B-O-H group from another borono group (Type 2).

In the early years of PBS research, in a study by Gridina et al.[30], they used an earlier proposed mechanism by Wick[143] of dative bonding between boron and oxygen of the PDMS backbone (Type 1) as the main one and tried to confirm that. They used various bifunctional and trifunctional boron (by n-functional, they meant molecules with $B\text{-}O_n$ or $B\text{-}Cl_n$ bonds, where non-functional were B-C bonds) containing molecules and condensed them with hydroxy-terminated PDMS at elevated temperature (> 150 ºC). The used reactants and reaction outcomes are known in Figure 2.14. Interestingly, PBS reacted with bifunctional boron compounds demonstrated very little change in viscosity, probably due to only chain extension where for network formation, trifunctional dynamic crosslinks are required. Nevertheless, solventless measurements of intrinsic viscosity showed a five-time increase in viscosity of PBS compared to PDMS precursor, which is a 9-10 time increase in MW according to Barry's method[147]. On the contrary, PBS with trifunctional boron compound formed a rubber-like polymer even at room temperature. In both cases, a new Si-O-B band on IR spectra was observed, which suggests that the formation of the polymer requires condensation. Surprisingly, PDMS condenses with B-O and B-Cl bearing compounds even at room temperature; therefore, the energy barrier of breaking these bonds is very small. Only a slight increase in MW of synthesized PBS was observed, which proves that crosslinks are temporary in nature. To verify that dative coordinative bonds are responsible for the dynamic properties, they added pyridine to PBS, which has nitrogen atoms and is more powerful than oxygen. It completely disrupted the formation of rubber-like properties in PBS due to the competitive binding of nitrogen to boron. An interesting feature of partially cured PBS was the presence of adhesive properties contrary to the cured silicone rubber.

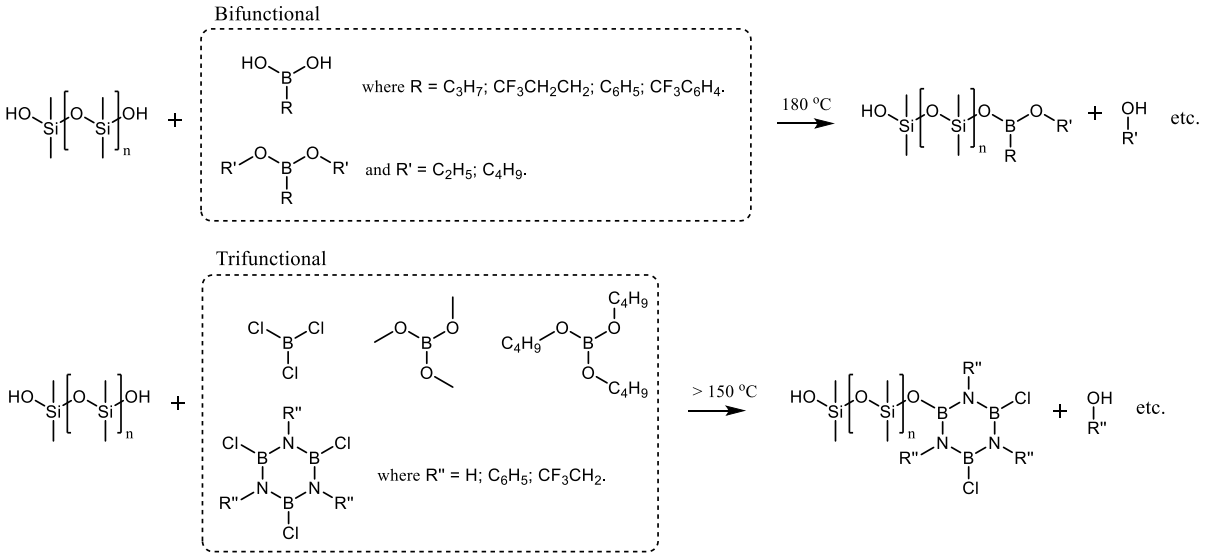

Figure 2.14 Various bifunctional and trifunctional boron compounds (defined by B-O_n- or B-Cl_n-) reacted with hydroxy-terminated PDMS; the scheme is developed based on reactions described in a study by Gridina and co-workers.[30] They found that only trifunctional boron compounds result in gelation of PBS whereas bifunctional demonstrate a mild increase in viscosity only.

In another study by Mitrofanov et al.[43] authors tried to provide additional evidence on the dative nature (Type 1) of dynamic crosslinking in PBS. They utilized two approaches to the synthesis of PBS, one was a classical condensation reaction between hydroxy terminated PDMS and BA at 160 ºC for 6 h and another was a reaction between dimethylcyclosiloxane and B_2O_3 in a blender at 240 ºC for 24 h. One sample was prepared by mechanical mixing of hydroxy-terminated PDMS with B_2O_3 without heating (Figure 2.15). All samples demonstrated a significant increase in viscosity without an increase in MW but rather a drop depending on boron loading. They employed the analysis of solution viscosities to assess how various solvents affect the association/coordination of PBS. Dioxane and acetone were found to be much better disruptors of association even at high concentrations compared to CCl_4 and chloroform, probably due to their oxygen being a stronger electron donor than oxygen in the PDMS backbone. Traces of dative bonding between acetone and boron were found on IR spectra due to the shift of the carbonyl band from 1720 to 1640 cm^{-1}, which is typical for the association of the carbonyl group. They claimed that dissociation of PBS in dry

solvent has nothing to do with hydrolysis. First, because the process is reversible (once the solvent is dried, it recovers its rubber-like properties completely), and secondly, because the line responsible for water presence in CCl_4 on IR was not there. After that, they assessed the thermomechanical properties of PBS, and the following trends were observed: increase in viscosity with an increase in boron loading (accompanied by the drop in MW probably due to chain scission); increase of glass transition temperature T_g with boron concentration; complete loss of elasticity around 90-100 ºC; absence of crystallization and melting in PBS compared to original PDMS.

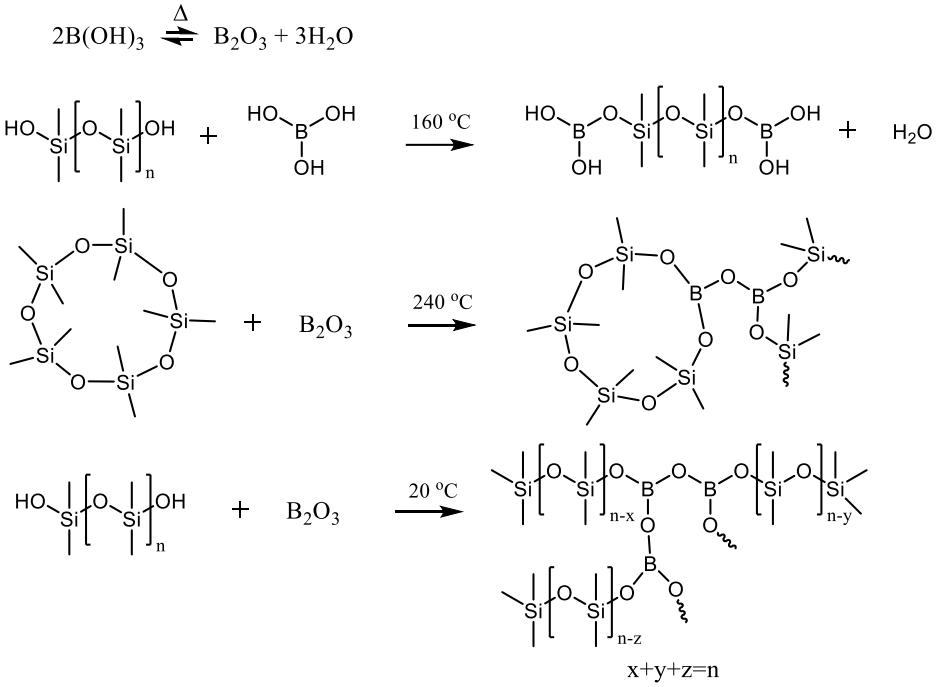

Figure 2.15 The scheme is developed based on reactions described by Mitrofanov and co-workers[43] for PBS synthesis. From the top to the bottom: reversible formation of boron trioxide from boric acid by dehydration, condensation of hydroxy-terminated PDMS with boric acid at 160 ºC, thermal cleavage of cyclic dimethyl siloxanes molecules at 240 ºC followed by insertion of boron trioxide, condensation with hydroxy-terminated PDMS with boron trioxide at room temperature with possible molecular structures of products.

Dative bonding of type 2 was proposed to exist by a Brook group. In their study[144], they proposed that supramolecular dimers are behind the dynamic crosslinking in polyboronicsiloxane, with dative bonding of type 2 playing the major role. They

synthesized PBA-PDMS-PBA type polymers where PBA is a phenylboronic acid covalently attached to PDMS through phenyl (Figure 2.16, a). At first, PBA groups were protected as boronic esters with various protective groups, which were later hydrolyzed in water which led to the formation of the elastomeric film on the water surface. The first evidence was that titration of monofunctional PDMS-PBA into bifunctional PBA-PDMS-PBA polymer was disrupting the dynamic crosslinking, which led to an almost complete loss of elastic properties. Therefore, it was concluded that one-to-one boronic acid complexation is the primary interaction between PDMS chains. Either by the formation of dimers through hydrogen bonding or dative bonding between boronic acids. Dative bonding between boron atom and oxygens in the PDMS backbone was concluded to not play a significant role in cross-linking. Also, boroxines were not found in polymers with the aid of NMR analysis. The addition of DMF (which is known to disrupt H-bonding[148]), glycerol, and TRIS to the water sub-phase prevented the formation of the solid film due to the competitive binding of their molecules to boronic acid sights after the removal of the protective group. pH was also found to influence dynamic cross-linking significantly. The 3-coordinate state is more favorable at low pH and the 4-coordinate state at higher pH, which was attributed to the less efficient interactions of anionic boron species in the presence of water. However, the contribution from hydrogen bonding versus dative bonding could not be compared or quantified.

More recently, the same research group attempted to do so in another study[42]. They used solid-state ^{11}B-NMR to distinguish between 3-coordinate boron sites, which provide only chain extension through H-bonded dimers, and 4-coordinate sites, which represent dative bonding between boronic acid PDMS end groups in telechelic and pendant PBS polymers (Figure 2.16, b). 4-coordinate dative interactions were found to be the origin of elastomer formation. Although, the presence of H-bonding was confirmed on the IR spectrum with characteristic bound OH peaks at 3300 cm^{-1}. Telechelic PBS has shown to be more solid than pendant despite PBA content. Dative bonding between boron and oxygen of PDMS backbone was rejected as a primary interaction since pendant PBS possesses much lower Young's modulus even at a much higher PBA concentration than telechelic one. This fact suggests that interactions take

place mainly at PBA sights. The further away they are from each other more effective crosslinking is. The presence of boroxines was not confirmed due to the absence of respective bands and peaks on IR and NMR spectra.

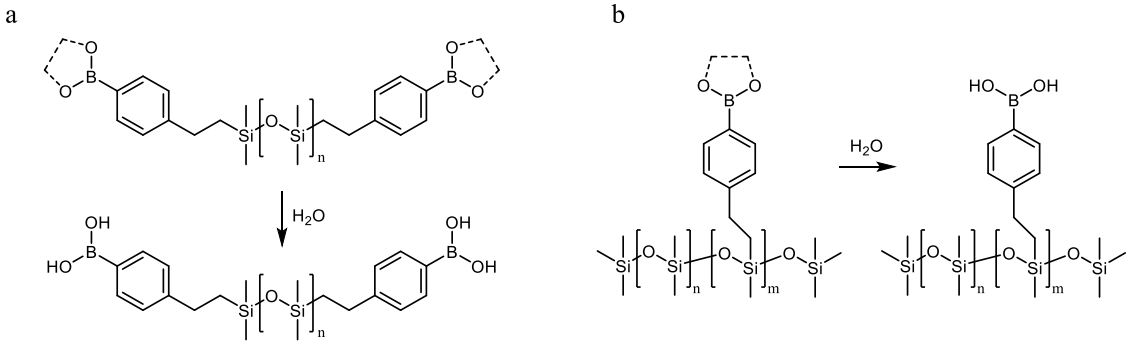

Figure 2.16 (**a**) Synthesized telechelic PBS where phenylboronic acid is covalently attached to PDMS through phenyl ring and protected ester groups; the scheme is developed based on the reaction description from ref.[144] Protective groups were later hydrolyzed in water which led to the formation of the elastomeric film on the water surface. (**b**) Synthesized pendant PBS protected with hydrolysable ester group; the scheme is developed based on the reaction description from ref. [42]

2.3.3.3 Dynamic covalent bonding

Another explanation for the mechanism of dynamic crosslinking in PBS was proposed in a comprehensive study by Bloomfield[29]. The proposed mechanism involves the endless substitution of oxygens atoms in the B-O bond with oxygens in neighboring -OH-bearing molecules, which do not involve breakage of covalent bonds but rather a ligand substitution (Figure 2.11, d). When oxygen from an R-OH type molecule aligns with the trifunctional boron crosslinking sights, oxygen lone electron pairs facilitate ligand swap resulting in an R attachment to the boron atom through oxygen. Though, it is important to highlight that in this mechanism, some amount of free -OH groups are necessary to be present to keep the dynamic equilibrium of the exchange. Otherwise, dynamic bonds would not be able to relax and reconnect; hence, they would behave as silicone rubber. However, the study that the author refers to as an inspiration for their proposed mechanism slightly differs. Their mechanism is also four-center

ligand exchange[149] but between two borane $B(OR)_3$ molecules without any -OH groups participating in the exchange. To prove the mechanism in study[29] they synthesized various PBS polymers according to Figure 2.17, where hydroxy-terminated PDMS of high quality was condensed with trimethyl borate $B(OCH_3)_3$ at room temperature with vacuum removal of methanol to facilitate condensation more efficiently. Resulted PBS, which possesses only temporary crosslinks, were named 'simple borosilicones' and the ones with both temporary and permanent 'non-simple borosilicones' due to more complex viscoelastic behavior. Simple borosilicones were shown to fit Maxwell viscoelastic model very well and the non-simple to the Fractional Maxwell model.

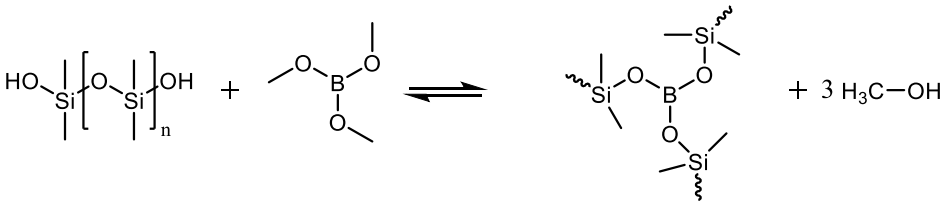

simple PBS

Figure 2.17 Synthesis scheme of simple PBS from a trimethyl borate with hydroxy-terminated PDMS which results in a trifunctional crosslinking through Si-O-B bonds and release of methanol; the scheme is developed based on the reaction description from ref.[29]

The effect of boron concentration (from 0 to stoichiometric saturation) was studied in simple PBS. An increase in boron content was accompanied by an increase in modulus with a maximum slightly before saturation. A significant increase in viscosity was observed after the boron amount exceeded the gelation threshold (50% of stoichiometric saturation for the trifunctional crosslinker according to Flory-Stockmayer theory[150,151]), which supports the hypothesis of trifunctional temporary crosslinking without chain extension through bifunctional crosslinking and/or combination with trifunctional permanent crosslinking. It was also shown that when permanent crosslinks are introduced to PBS, viscoelastic behavior changes significantly; therefore, it seems that *trifunctional transient couplings* are the main interactions in simple PBS.

The modulus of permanently crosslinked silicone rubber with a trifunctional crosslinker was found to be even lower than the modulus of PBS produced from the same MW PDMS at the same stoichiometric concentration, which is additional evidence that simple PBS is a *covalently bonded dynamic network*. The presence of both permanent and temporary crosslinks in a non-simple PBS leads to deviation from the Maxwell model; therefore, only temporary crosslinks are present in a simple PBS. PBS from higher MW PDMS (above entanglement), the addition of fumed silica (high aspect ratio filler), and mixing high MW PDMS gum to simple PBS all resulted in a deviation from the classic Maxwell viscoelastic model due to the presence of non-transient couplings which could be fit with Fractional Maxwell model.

In another study, they showed that permanently crosslinked rubber has a lower plateau and different shape of storage modulus curve[40].

To show the importance of the presence of -OH groups on the dynamic exchange, characteristic time τ_c (mean a lifetime of temporary crosslinks) was used to assess the effect of various competitive binders (molecules with free -OH groups such as water, carboxylic acid, alcohol, silanol) on dynamic crosslinking of simple PBS. After vacuum drying of PBS τ_c < 40 s once it equilibrates with the laboratory air (50% humidity) τ_c falls to 15 s or less due to catalytic disruption of the exchange with water molecules. They interfere with dynamic exchange with silanol groups by competing with them and binding to boron instead of them. Carboxylic acid was found to be even more effective at τ_c (13.6 s) reduction, probably due to a more favorable exchange between -COOH and boron oxygens than with silanol groups. Alcohol was less effective than water and carboxylic acid but still showed some reduction of τ_c. The excess of silanol groups did not demonstrate any significant effect on the disruption of dynamic exchange.

2.3.3.4 Supramolecular interactions of boronic acids

Boronic acids have gained a lot of attention in the past few years in the field of supramolecular chemistry due to the unique reversibility of the B-O covalent bond[44,152,153]. In the presence of diol boronic acid could form an ester upon dehydration;

this reaction is fully reversible and can be dynamic when in equilibria. In this scenario, dynamic exchange occurs through a dissociative mechanism where the ester bond undergoes hydrolytic cleavage first, and then free boronic acid and diol undergo re-esterification with a neighboring diol and boronic acid from another molecule. It was found that boronic esters can also participate in associative bond exchange through transesterification when an excessive number of free diols are present or even through direct diol exchange (metathesis) between the different boronic ester species (Figure 18, a)[44]. It was recently shown that metathesis in boronic esters can occur between slightly different boronic ester species in the absence of solvent and without any detectable amount of free diol, water, or residual phenylboronic acid[154]. It was found that the associative mechanism dominates in dry conditions whereas dissociative in humid[155].

Upon dehydration, in the absence of diols, boronic acids can yield cyclic trimers called boroxines[44,156] (Figure 2.18, b). There are two commonly known pathways of boroxine formation in a dry solvents/solventless environment – via direct dehydration or Lewis base ligand facilitated dehydration[44,152,156]. Boroxines can also be broken down/reformed in a dissociative fashion through hydrolysis/dehydration. It was also shown that they could participate in direct exchange through the associative mechanism (similar to transesterification of boronic esters), where boronic acids reshuffle in boroxine linkages through fast exchange with free boronic acid[157,158]. Furthermore, boroxines were found to participate in metathesis in the absence of free boronic acids[157,159].

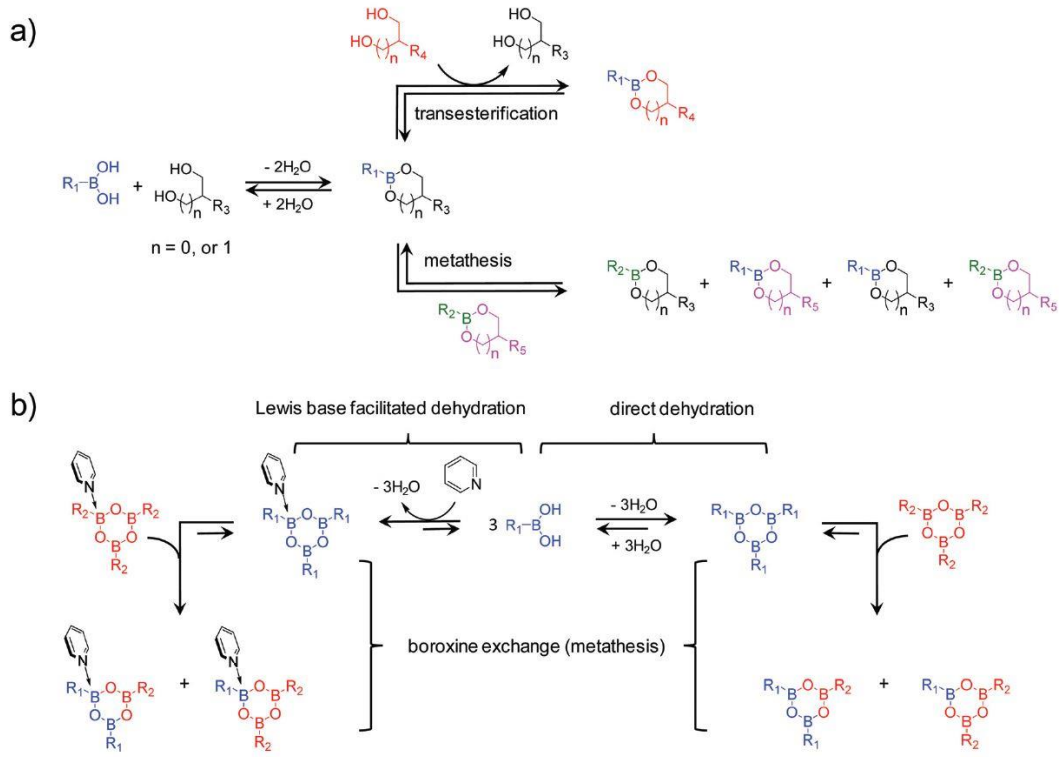

Figure 2.18. (**a**) Formation and exchange of boronic esters. The dissociative mechanism of exchange through dehydration/hydrolysis (on the left) and associative mechanism through transesterification and metathesis (on the right). (**b**) Formation and exchange of boroxines from boronic acids. The formation can occur through direct dehydration or Lewis base facilitated dehydration. The exchange of boroxines occurs through metathesis. Reprinted with permission from ref.[44] © Royal Society of Chemistry.

Both boronic species – boronic esters and boroxines share the exact same mechanism of dynamic exchange through the reformation of B-O bonds. Boronic esters are preferred in a presence of free diols whereas boroxines in the absence. The dynamic covalent crosslinking proposed by Bloomfield resembles the mechanism of transesterification of boronic esters quite well if silanol groups replace diols. This fact points out the possibility of dynamic covalent crosslinking to serve as an explanation of dynamic properties in PBS. However, in view of the existence of other mechanisms that have served as an explanation for decades, this mechanism must be carefully experimentally tested and investigated.

Chapter 3

Experimental Methodology

In this chapter, we discuss the basic principles of characterization techniques used in this thesis. Specifically, we describe working principles of employed characterization techniques for readers unfamiliar with them (including steady and dynamic rheological analysis, Fourier-transform infrared spectroscopy, gel permeation chromatography, weight drop impact test, nuclear magnetic resonance, matrix-assisted laser desorption/ionization time-of-flight mass spectrometry) and how they were used to achieve the objectives.

3.1 Characterization techniques

3.1.1 Rheological analysis

Rheology is a study on the flow of the (liquid, gas, and soft-solid) matter. The focus of the rheology is the characterization of viscoelastic properties of materials. Deformation and speed of deformation are the main variable parameters in the rheological experiments. There are different modes of deformation of the matter such as tensile, compression and shear. Conventional rheometers are operating in a shear deformation mode only in most of the cases which creates a perception that terms "rheological analysis" and "shear deformation" are somewhat similar. By rheological properties fluids can be divided into Newtonian and non-Newtonian. Newtonian fluids follow the Newton's law of viscosity (1) regardless of the deformation mode whereas for non-Newtonian fluids deviates from it:

$$\tau = \eta \frac{du}{dy}, \tag{3.1}$$

where τ is the shear stress, η is the viscosity and du/dy is the rate of shear deformation. In other words, viscosity is a constant for a Newtonian fluid at a given pressure and temperature. However, for a non-Newtonian fluids viscosity is not constant, if it increases with the shear rate it is called shear thickening and if decreases – shear thinning. Typical rheometer operates in two modes, rotational and oscillatory. Rotational mode is based on the principle of continues shear deformation of the material. By controlling the torque of the motor deformation/deformation rate values could be obtained (or vice versa). The shear stress and shear rate are derived based on the geometry of the sample holder (and torque values for the shear stress). Apparent viscosity could be obtained according to equation (1) based on the measured shear stresses and rates. Three main geometry types are parallel plate (PP), cone and plate (CP), and concentric cylinders (CC). Advantage of CP geometry is that the shear rate is normalized across a cone (shear deformation is uniformly distributed), however, the minimum gap size is limited by the cone angle and the truncation height. PP geometry allows to use much smaller gaps which prevents fluid slippage at higher rates.

In oscillatory mode, on the contrary, shear strain γ is applied in a periodical fashion (2):

$$\gamma = \gamma_0 \sin(\omega t), \tag{3.2}$$

where γ_0 is a strain amplitude, ω is an angular spend and t is time. This approach provides more details on the viscous and elastic properties of the material, as most materials are known to be viscoelastic in nature. The unique feature of this mode is that by measuring time lag between applying sin strain and the response sine curve viscous and elastic could be characterized and quantified separately. This time lag is called phase shift δ and it defines how elastic or viscous is the behavior at a given stress/strain (3):

$$\sigma = \sigma_0 \sin(\omega t + \delta), \tag{3.3}$$

where σ_0 is a shear stress amplitude. For example, in an absolutely elastic material the phase shift would be 0º meaning that the preset and response sin curves coincide, and in an absolutely viscous fluid shift would be 90º. Therefore, δ is always lying somewhere between 0 and 90 degrees since all materials are partially viscous and partially elastic. Two parameters are used to quantify the extent of viscoelastic behavior: storage and loss modulus. Storage modulus G' (4) represents elastic component and loss modulus G'' (5) the viscous component:

$$G' = \frac{\sigma_0}{\gamma_0}\cos(\delta), \tag{3.4}$$

$$G'' = \frac{\sigma_0}{\gamma_0}\sin(\delta). \tag{3.5}$$

In this report, parallel plates geometry was used for all measurements (Figure 3.2). We utilized rotational rheometer mode to characterize flow characteristics of the shear stiffening materials. Shear rate ramp was used to observed and quantify shear thickening in STFs and, also, to obtain viscosities of liquid PBS samples compare to PDMS precursors. Oscillatory mode was used to obtain viscoelastic characteristics of gel-state PBS samples.

Figure 3.1 Anton Paar MCR 501 rotational rheometer which was used in this thesis with a parallel plate spindle.

3.1.2 Drop weight impact testing

Falling weight impact testing is the method to assess response of the material to the sudden deformation. Without any additional equipment it could measure the energy required to break/damage the sample or with the aid of the load cell (or accelerometer, speed camera etc.) provide more insights on the time/spatial distribution of the impact within the sample and the response to it on the microsecond's timescale. This type of testing employs approach of basic mechanics, such as, that the impact energy E_{imp} is the potential energy of the free-falling weight m from a specific height h:

$$E_{imp} = m \cdot g \cdot h, \tag{3.6}$$

where g is a gravitational acceleration. Drop weight tests are low-velocity impacts due to constraints of the height and weight to produce velocities higher than 100 m/s. Accelerometer sensor is typically used to measure deacceleration of the impactor upon contact with the sample. The normal force and its distribution over impact time/thickness can be registered by placing the load cell beneath the sample. Two characteristics are usually used to assess the impact protective properties – peak force

and the shape of force distribution over time. Peak force value should be as small as possible, and distribution should be as broad as possible. If strain sensor is not installed displacement can be calculated from either the deacceleration or normal force. By integrating either of them velocity is obtained, second integration of which gives displacement y:

$$y(t) = \iint_{t_0}^{t} \left(\frac{F_N(t)}{m} dt \right) dt, \tag{3.7}$$

In this report, drop weight impact tests were used to assess an impact absorption of shear-stiffening materials. Hemispherical impactor of 5 kg was used for STF tests and cylindrical impactor tip of 15 mm diameter was used for PBS testing (Figure 3.3). More detailed descriptions of the setups and testing parameters will be given in a respective results chapter.

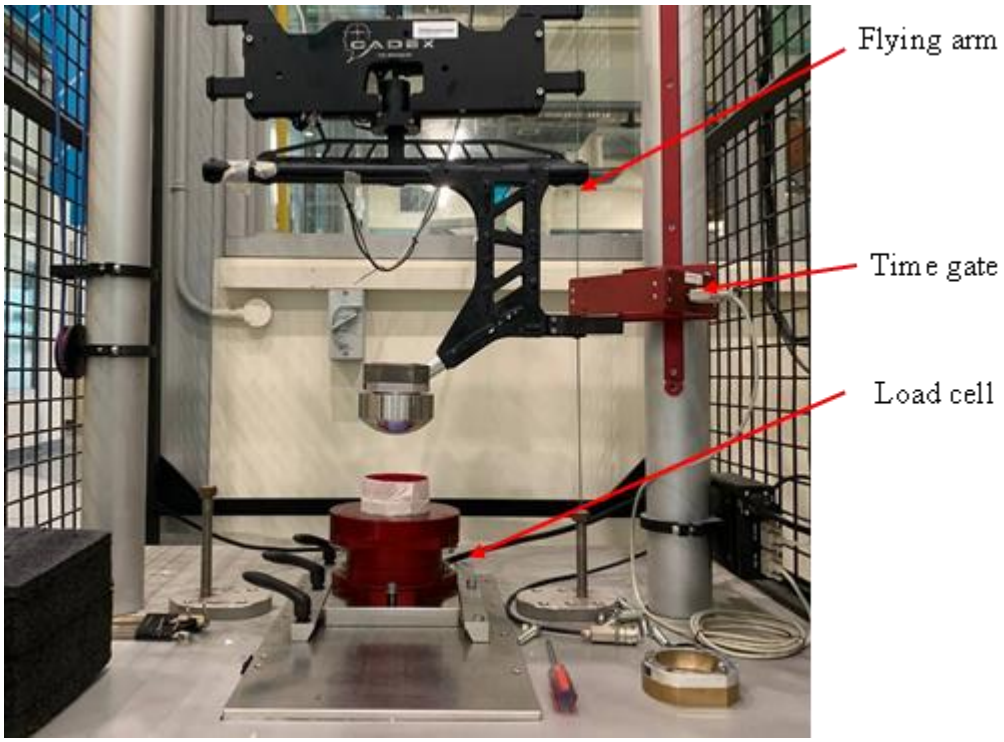

Figure 3.2 Drop-weight impact testing machine CADEX Twin Wire 1000 kg which was used in this thesis.

3.1.3 Fourier-transform infrared spectroscopy

Fourier-transform infrared spectroscopy (FTIR) is a technique which allows to obtain an absorption or emission infrared spectra of a gas, liquid or solid substances. Infrared radiation is absorbed at certain frequencies that are directly related to the energy of vibrations of interatomic bonds in a molecule. Different bonds in a molecule vibrate with different energies and therefore absorb different wavelengths of IR radiation. The position (frequency) and intensity of these individual absorption bands affect the overall spectrum, making it unique to the molecule of a particular substance. A feature of the FTIR spectrometer (unlike conventional IR) is that it collects spectral data of all wavelengths at a time. Here, a continuous source generates IR radiation in a wide range of wavelengths. The infrared light then passes through the interferometer and is directed onto the sample. Unlike dispersive measurements, first interferogram is obtained, which must be converted into an IR spectrum. Conversion of the raw data into spectrum is done by Fourier transformation.

The FTIR spectrometer is built on the principle of the Michelson interferometer. In it, the investigated radiation serves as a source of illumination, and one of the mirrors has a certain constant speed of movement. The output is a curve that describes the dependence of the receiver reading on the difference in the path of the rays. The studied radiation is divided into two waves, which pass through different optical paths, interfere, and are received by a photodetector. As a result of interference, the wave has radiation with an intensity:

$$I = Q_1 + Q_2 + 2\sqrt{Q_1 Q_2} cos\left(\frac{2\pi\Delta}{\lambda}\right), \tag{3.8}$$

where λ is the wavelength of the radiation, Q are the wave intensities in the shoulders and Δ is a path difference. If $Q_1 = Q_2 = 0.5Q$, the equation (8) becomes:

$$I = Q\left(1 + cos\left(\frac{2\pi\Delta}{\lambda}\right)\right), \tag{3.9}$$

When light with a spectral distribution $Q(\lambda)$ hits the photodetector, the reading of the photodetector $F(\Delta)$ will correspond to the sum of the reports of the spectrum components:

$$F(\Delta) = \int_{\lambda_{min}}^{\lambda_{max}} Q(\lambda)P(\lambda)\left(1 + cos\left(\frac{2\pi\Delta}{\lambda}\right)\right)d\lambda, \tag{3.10}$$

The sensitivity of the photodetector is a proportionality factor between the reading and the light flux received by the detector. If we represent the expression as the sum of two integrals, while taking into account that the terms will be equal at $F(\Delta = 0)$, and the second integral we call $F'(\Delta)$, then we get:

$$F'(\Delta) = \int_{\lambda_{min}}^{\lambda_{max}} Q(\lambda)P(\lambda)cos\left(\frac{2\pi\Delta}{\lambda}\right)d\lambda, \quad (3.11)$$

and $F(\Delta) = F'(\Delta) + F'(0), F'(\Delta) = F(\Delta) - 0.5F(0)$.

Thus, the interferogram is a dependence curve $F'(\Delta)$, that is, a signal that is recorded depending on the change in the path difference or the cosine Fourier transform of the function $Q(\lambda)P(\lambda)$. The inverse Fourier transform of the interferogram with a known sensitivity curve of the receiver makes it possible to determine the spectrum:

$$Q(\lambda) = \frac{1}{P(\lambda)}\Phi^{-1}\{F'(\Delta)\}, \quad (3.12)$$

There are several methods for obtaining FTIR spectra of an analyzed material. The most common methods are via transmission/absorption or via attenuated total reflection (ATR). Unlike transmission measurement, in ATR method the optical path length is independent of sample thickness. In ATR spectroscopy, light passes through an ATR crystal that has two main characteristics: it is optically transparent at the frequency of the incident radiation (there is little or no radiation absorption) and the material from which the ATR sensor is made has a refractive index higher than that of the environment.

Depending on the chosen optical material and how the sensor is manufactured, the number of reflections (optical path nodes) can be precisely controlled. The effective optical path length of an ATR sensor is determined by the number of internal reflections multiplied by the penetration depth of the evanescent wave. At each node, a standing wave of radiation emerges to the surface. This wave decays rapidly as the distance to the sensor surface increases. Thus, the radiation affects only the substance that is in direct contact with the sensor (Figure 3.4).

The penetration depth also depends on the specific radiation wavelength, therefore, when the sample is irradiated with modulated radiation, the position of the peaks in the spectrum will be similar to the position of the peaks in the transmission/absorption spectrum, however, the brightness of the bands will be different.

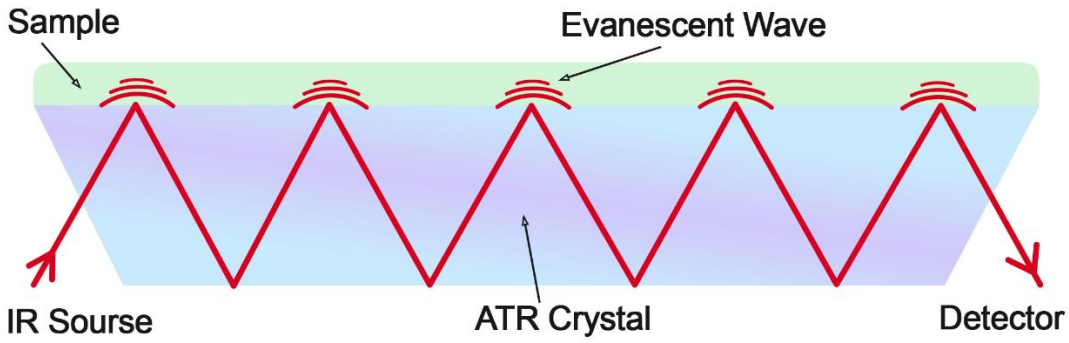

Figure 3.3 Basics of the attenuated total reflection (ATR) method of infrared spectroscopy.

In this thesis, ATR was used for a gel and solid samples, normal transmission/absorption mode was used for liquid and powder samples. KBr pellet was a reference in both cases, liquid samples were placed on KBr pellet after background scan and powder samples premixed with KBr were made into pellets.

3.1.4 Gel permeation chromatography

Gel permeation chromatography (GPC) is a type of chromatography in which the molecules of substances are separated by size due to their different ability to penetrate into the pores of the stationary phase. In this case, the largest molecules (higher molecular weight) capable of penetrating into the minimum number of pores of the stationary phase are the first to leave the column. Substances with small molecular sizes, which freely penetrate into the pores, come out last (Figure 3.5).

A sample solution is introduced into the column, the volume of which is limiting for the quality of chromatography. For analytical separations, it should not exceed 0.1% of CV (total column volume), and for preparative purification, it should not exceed 8-10% of CV. The column is packed with powder, the particles, or granules of which have pores of a certain diameter. Macromolecular substances that do not enter the pores pass between the granules, so their retention volume is equal to the volume of the column minus the volume of the stationary phase (the so-called free volume). They elute first. Molecules of medium size fit into the pores of the sorbent, but not completely. Therefore, their retention volume is somewhat higher than the free volume.

They elute second. The smallest molecules freely enter the pores together with solvent molecules. Therefore, their retention volume in the column is much higher than the free volume and approaches the total volume of the column (that is 100% CV). They elute last.

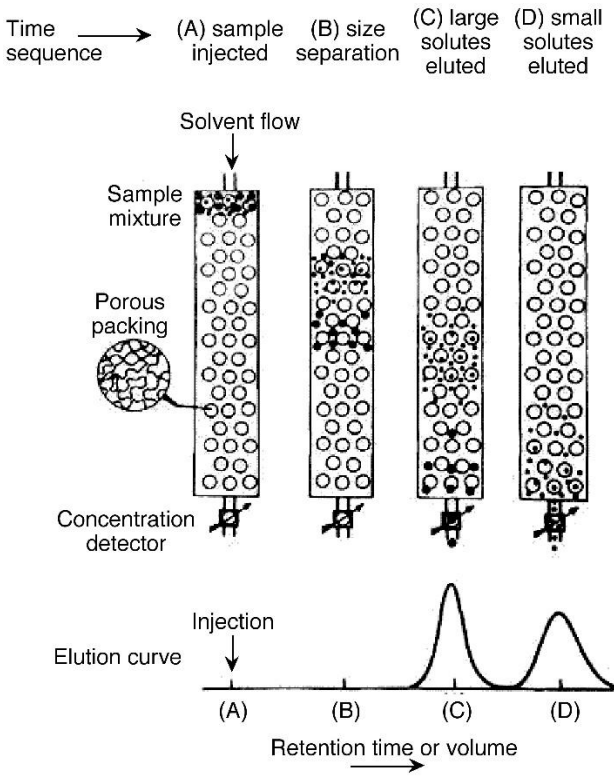

Figure 3.4 Basics of gel-permeation chromatography. Adapted with permission from ref. Copyright © 2009 John Wiley & Sons, Inc.

To correlate retention time to molecular weight of the substance calibration is required. Typically, a few calibrants of a known molecular weight (and narrow MW distribution) which also fall into the expected MW range of the analyte are run through GPC column first. At a next step calibration curve is plot based on a calibrants elution time. This curve allows to convert the retention time of the analyte sample into the MW.

In this report, monodisperse polystyrene calibrants were used for a calibration curve, HPLC grade THF was a solvent medium. After conversion of the retention time of the PBS samples into the MW, the number-average M_n and weight-average M_w values were calculated according to the following equations:

$$M_n = \frac{\sum M_i N_i}{\sum N_i}, \tag{3.13}$$

$$M_w = \frac{\sum M_i^2 N_i}{\sum M_i N_i}, \tag{3.14}$$

3.1.5 Nuclear magnetic resonance (NMR)

Nuclear magnetic resonance (NMR) spectroscopy is a method for studying chemical objects that uses the phenomenon of nuclear magnetic resonance. It is a resonant absorption or emission of electromagnetic energy by a substance containing nuclei with non-zero spin in an external magnetic field, at a frequency ν (called the NMR frequency), due to the reorientation of the magnetic moments of the nuclei. In a constant magnetic field for nuclei with a nonzero nuclear spin, energy levels are split (Zeeman effect, Figure 3.6). The energy value of splitting, and, accordingly, the resonant frequency is determined by the nature of the atomic nucleus, the electronic environment, and the nature of intra- and intermolecular interactions. Examples of nuclei with resonance are ^{1}H, ^{13}C, ^{15}N, ^{19}F, ^{29}Si, ^{31}P, etc. Chemical shifts and spin–spin coupling are the common techniques used to analyze the nuclei environment and intra/intermolecular interactions.

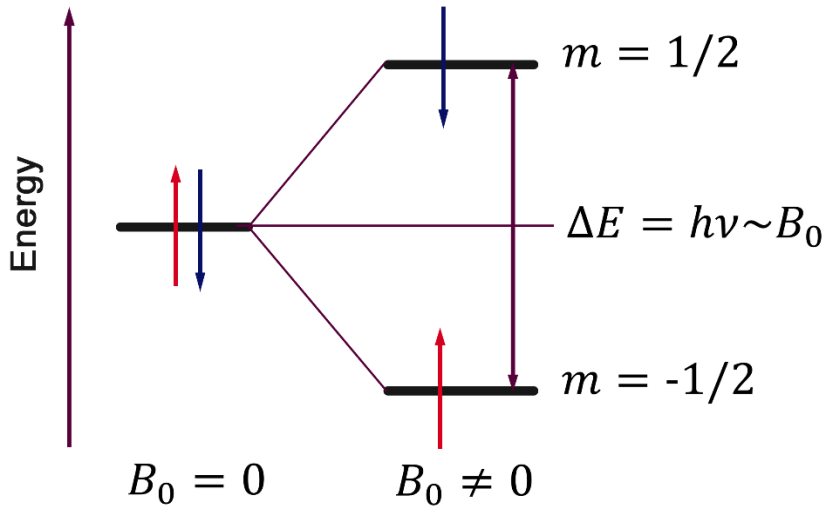

Figure 3.5 Energy levels splitting in magnetic field (Zeeman effect).

Chemical shift is the shift of the NMR signal depending on the chemical composition of the substance, due to the shielding of the external magnetic field by the electrons of the atoms. When an external magnetic field appears, a diamagnetic moment of atoms arises due to the orbital motion of electrons. This movement of electrons forms effective currents and, therefore, creates a secondary magnetic field, which is proportional, according to Lenz's rule, to the external magnetic field and oppositely directed. This secondary field is superimposed on an external magnetic field near the nucleus, and as a result, the local magnetic field in the place where the atomic nucleus is located is reduced. Therefore, the distance between the levels of nuclear magnetic energy decreases.

Spin–spin coupling is an indirect interaction between two nuclear spins through chemical bonds which results in NMR signals splitting. For example, for PMR if the adjacent nucleus to the proton is pointing toward or against the spectrometer magnetic field it will give two signals per proton instead of one. The type of splitting (singlet, doublet etc.) provides additional insights about the connectivity of atoms in the molecule.

NMR spectroscopy is divided into liquid (liquid or dissolved samples) and solid state (solid, viscous, and other samples with reduced molecular and atomic mobility). Liquid NMR spectroscopy has become widespread for the study of various organic and bioorganic substances since it makes it relatively easy to obtain high-resolution spectra. However, not any solvent can be used for a liquid NMR. Ideally, it should not have protons, therefore, deuterated solvents are typically used. The deuterium signal is used for field shimming. Shimming is a procedure for improving the uniformity of the magnetic field, which is carried out using special small electromagnetic coils built into the device (called shims), which correct the main magnetic field so that its uniformity is highest exactly in the center of the sample.

Solid-state NMR spectroscopy as an analytical method has found application after the development of special instrumental (MAS – magic angle spinning) and spectral techniques, which made it possible to obtain high-resolution spectra in solid and viscous samples. In general, solid-state NMR spectroscopy, compared to liquid-state

NMR, has a lower resolution, but much higher sensitivity due to the absence of sample dilution.

3.1.6 MALDI-ToF mass spectrometry

Mass spectrometry is a technique based on ionization of the analyte with subsequent formation of gaseous ions which are separated at the detector based on their mass-to-charge ratios (m/z). The analyte is converted into the molecular or quasimolecular ions and fragments depending on the type of ionization method used. Typically, by electron removal from analyte molecule [M] radical cations are being formed $[M]^+$ and this ions are analyzed in so-called positive mode, if electron is added radical anions are formed $[M]^-$ and analyzed in a negative mode. Quasimolecular ions are the radical cations or anions formed by addition/subtraction of another ion to the analyte radical, such as $[M+H]^+$, $[M+Cl]^-$, $[M+Na]^+$ etc. "Soft" ionization typically generate only quasimolecular/molecular ions whereas "hard" ionization may also produce fragment ions.

In a time-of-flight (ToF) mass analyzer, ions fly out of the source and enter the flight tube, where there is no electric field (field-free gap). Having flown a certain distance d, the ions are registered by an ion detector with a flat or almost flat surface. The physical principle of the ToF mass analyzer is that the potential difference U accelerates the ions in the ion source to a speed v according to the equation:

$$\frac{mv^2}{2} = zU, \tag{15}$$

For a fixed length of the field-free gap from the ion source to the ion detector, the ion flight time $t = d/v$, then:

$$\frac{m}{z} = t^2 \frac{2U}{d^2}, \tag{16}$$

The time-of-flight mass analyzer is a pulsed mass analyzer, that is, ions do not flow continuously from the ion source into the time-of-flight part, but in portions at certain time intervals. Such mass analyzers are compatible with matrix-assisted laser desorption ionization (MALDI), since in this ionization method, ions are also formed not continuously, but with each laser pulse. MALDI is a desorption method of "soft"

ionization caused by the laser radiation pulses on a matrix with an analyte. The function of the matrix is to reduce the destructive properties of laser radiation and improve the ionization of the analyte (Figure 3.7).

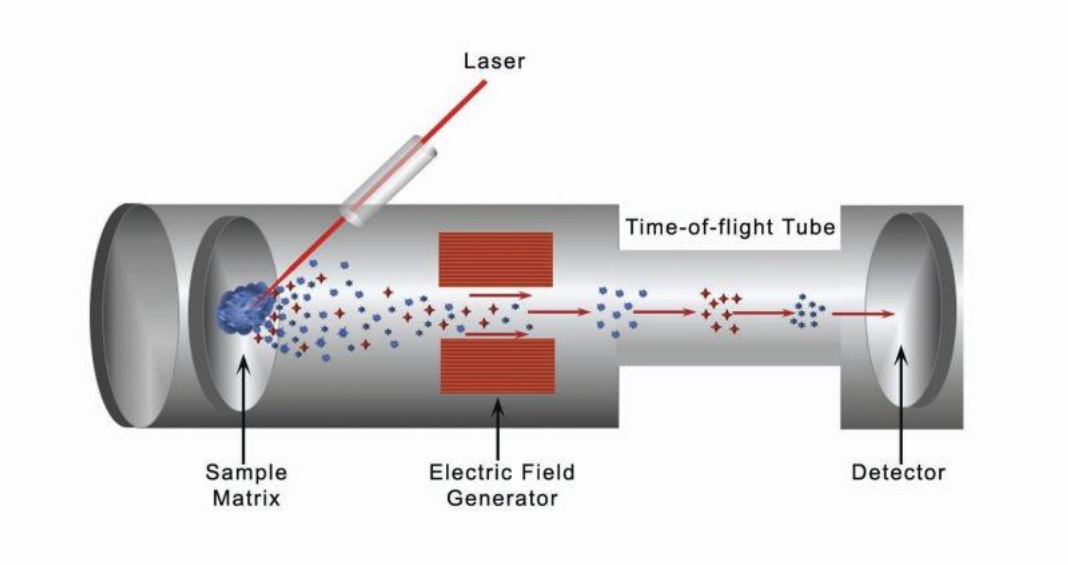

Figure 3.6 Basic principles of MALDI-MS technique with an axial time-of-flight (ToF) detector.

Chapter 4

In situ observation of shear-induced jamming front propagation during low-velocity impact in polypropylene glycol/fumed silica shear thickening fluids

In this chapter, we provide new evidence of shear jamming in polypropylene glycol/fumed silica suspensions using optical in situ speed recording during low-velocity impact and explain how it contributes to impact absorption. Flow rheology confirmed the presence of discontinuous shear thickening at all studied concentrations. Calculations of the flow during impact reveal that front propagation speed is 3-5 times higher than the speed of the impactor rod, which rules out jamming by densification, showing that the cause of the drastic impact absorption is the shear jamming. The main impact absorption begins when the jamming front reaches the boundary, creating a solid-like plug under the rod that confronts its movement. These results provide important insights into the impact absorption mechanism in fumed silica suspensions with a focus on shear jamming.

*This section published substantially as "In situ observation of shear-induced jamming front propagation during low-velocity impact in polypropylene glycol/fumed silica shear thickening fluids" in *Polymers* (DOI: 10.3390/polym14142768). Reproduced with permission, Copyright 2022, MDPI Publishing.

4.1 Introduction

Shear thickening fluid (STF) is a type of colloidal suspension that possesses a non-Newtonian behavior under shear deformation. More specifically, it is a dilatant, where its shear viscosity increases beyond a critical shear rate. The shear thickening phenomenon exhibited is reversible, meaning the material returns to its initial liquid state upon removal of the applied stress[18]. The mechanism of shear thickening was recently re-explained using the contact rheology model[16,85–88] after reconsidering the old explanation by the hydrodynamic model[83]. After reconsideration, two types of shear thickening were introduced[18]: continuous shear thickening (CST), which is a weak type of shear thickening mainly driven by hydrodynamic forces, and discontinuous shear thickening (DST), which results in a discontinuous jump in shear stress beyond a critical shear rate due to contact forces between particles. A relatively new concept of jamming by shear (SJ) was introduced as an extreme behavior of DST suspensions below jamming particles fraction ϕ_J for a range of suspensions with sufficiently strong frictional interactions[16]. SJ is a reversible transition of unjammed dense suspension to a solid-like state with finite yield stress induced by shear[89–91].

Despite the variety of studies on a cornstarch water suspension, fumed silica was found to be a preferable choice for many applications due to its lower weight per unit volume. Fumed silica is produced from pyrolyzing tetrachlorosilanes in a hydrogen–oxygen flame, forming primary particles (5–30 nm) that cool to form silica aggregates (100–500 nm). This gives it a fluffy white appearance characterized by extremely low bulk density (20–50 g/L), high surface area (125–200 m^2/g), and high aspect ratio[110]. The large surface area of fumed silica is dominated by the presence of silanol groups that are prone to form hydrogen bonds. In fumed silica/polypropylene glycol (PPG) colloidal suspensions, the terminal hydroxyl bonds, as well as internal oxygen atoms on the PPG chains, form hydrogen bonds with the abundant surface silanol groups on fumed silica. The interaction surface between PPG and fumed silica acts as a solvation layer that hinders the interaction between fumed silica particles, hence stabilizing the dispersion of fumed silica in the suspension[111].

As was shown earlier[96], interparticle hydrogen bonding can be a source of strong frictional interaction, which may lead to SJ in dense suspensions. Since fumed silica surface is silanol rich with a high area, it suggests that it may possess shear jamming behavior at high concentrations/stresses. The first evidence of SJ in fumed silica suspension was provided by Naald et al.[47], where they observed it during impact using high-speed ultrasound imaging. They found that SJ was achieved only at the intermediate molecular weights of PEG due to the optimal thickness of the solvation layer, which allows the forming of frictional contact networks rather than lubricated contacts.

Unique dynamic properties of STF have found applications in the protective field, from sports protective equipment to flexible body armor[12]. However, the origin of impact absorption has been debated for many years, especially when it comes to jamming during compressive low-velocity impact. Two main mechanisms were proposed: jamming by densification[117,118] and by shear[119,120,122,123], where the second requires sufficiently strong frictional interactions between particles, such as via hydrogen bonding[96].

In this chapter, we provide the evidence that shear-induced jamming transition is the main contributor to impact absorption in fumed silica STF. We utilize direct optical method to observe the jammed front formation and growth during impact. The big advantage of our STF is the total optical transparency due to the amorphous nature of fumed silica, which allowed us to record and track the displacements of dispersed dye particles during impact. This data was correlated with the results of the drop weight test which helped to answer a few questions related to the mechanism of impact absorption. Therefore, this study provides useful insights for the fundamental research of shear thickening and jamming as well as for engineering research to design and tailor STF for particular requirements.

4.2 Materials and experimental methods

4.2.1 Chemicals and samples preparation

Polypropylene glycol (PPG) 400 and hydrophilic fumed silica with 0.2-0.3 μm average particle size and surface area of 200 m^2/g (S5505) were purchased from Sigma-Aldrich. STF with 15%, 20%, and 25% weight fraction of fumed silica were prepared by first

weighing out PPG400 and, respectively, the amount of fumed silica required. A beaker consisting of PPG400 is mixed using a high shear mixer (Silverson L4RT), while small volumes of fumed silica are added gradually to the mixture. The mixture is stirred until all fumed silica has been evenly integrated. The beaker with the mixture is placed in a sonicator bath until all air bubbles disappear. The resultant mixture is a clear colloidal suspension, with varying viscosities depending on the weight fraction of fumed silica used. Fumed silica true density value of 2.3187 ± 0.0012 g/cm^3 was used from the literature[160] where it was obtained for hydrophilic fumed silica with the same surface area (200 m^2/g) to calculate volume fractions from the weight fractions. Based on the calculation weight-to-volume ratio is 2.086. Hence, $\phi_{15\%w} \cong 7.2\%$, $\phi_{20\%w} \cong 9.6\%$, $\phi_{15\%w} \cong 12.0\%$. However, weight fractions were used along with the manuscript in view of the greater prevalence of weight fraction values in the literature on fumed silica suspensions. Densities of STF were measured using volumetric flask/calipers and weights. The values are as follows 1.06 g/cm3, 1.10 g/cm3 and 1.14 g/cm3 for STF 15%, 20% and 25% respectively.

4.2.2 Characterization

The flow rheological properties of STF are tested using a rheometer (Anton Paar, MCR501) with 25 mm diameter parallel plates (PP-25) and a gap of 0.5 mm to ensure adequate filling of the STF over the testing disk. All tests were conducted at 25°C. A coin-sized amount of STF is poured onto the Peltier plate, followed by the lowering of the parallel plate to the set gap width. The excess STF leakages at the edge of the parallel plate are trimmed using a task wiper, ensuring that the entire surface area of the top plate is in contact with the STF. Pull-up test is designed to achieve higher shear stresses without fluid slippage. A mechanical tester, MTS Criterion Model 42, is used to measure the normal force of the STF when the submerged rod is retracted upwards. The equipment set-up is shown in Figure 4.1a, where a top pneumatic grip is attached onto the load cell and used to clamp the steel rod in place. A 3D-printed polylactic acid (PLA) sample holder with a storage diameter of 20 mm and a depth of 4 mm is also attached firmly onto the bottom steel plate using highly adhesive double-sided tape.

The schematic diagram below (Figure 4.1b) shows the starting position for the tests. The

steel rod has a diameter of 16 mm, to ensure that a fixed distance of 2 mm is observed between the rod and the bottom and sides of the sample holder. The sample holder is approximately ¾ filled with STF before the rod is lowered into the sample. After that, any excessive fluid is removed until a horizontal level is achieved. The rod is lifted at a speed ranging from 0.1 mm/s to 30 mm/s and the normal force experienced by the rod is recorded.

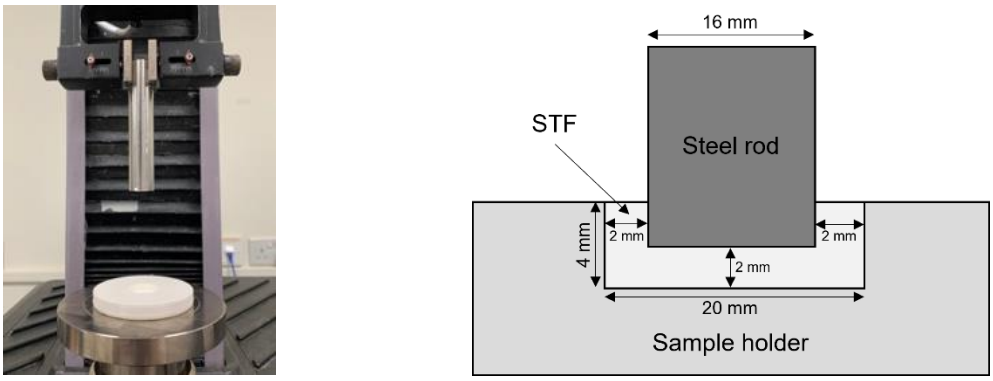

(**a**) (**b**)

Figure 4.1 Custom setup for pull-up tests: (**a**) Photo of the setup with a pneumatic grip holding the cylindrical rod at the top and the sample holder attached at the bottom; (**b**) Schematic illustration of the starting position during the pull-up test with all dimensions shown.

Drop weight impact tests on bulk samples were carried out on the CADEX twin wire flying arm machine. The illustration of the setup with all dimensions is shown in Figure 4.2a. The hemispherical impactor was attached to the flying arm with a total drop weight of 5 kg. An accelerometer and 44 kN load cell were used for deacceleration and ground reaction force registration. Flexible 3d-printed thermoplastic urethane (TPU) carrier (with 98 mm in diameter and 30 mm in height) was used as an STF holder. The setup was designed the way that the impactor tip does not touch the walls of the soft container. All STF samples were filled to the same level in a container with a total thickness of 13 mm. At least 10 times impact tests were repeated for each sample at each height to make sure that the results are reproducible and are within 10% error. Then all results were averaged. Displacement was calculated from the integration of the velocity-time plot, which in turn was obtained by integrating the force-time plot divided by the impactor weight. Impact energy was calculated from the simple equation $E = m \cdot g \cdot h$, where the impactor mass m was 5 kg

and constant, gravitational acceleration g was used as 9.8 m/s and constant and impactor height h was a variable.

Another impact test was designed to visualize and analyze the displacement of fluid during the impact (Figure 4.2b). Sheets of 2 mm thick clear acrylic glass were used for the setup which allowed to optically inspect the STF during the impact. All dimensions are present in Figure 2b, the geometry of the container and tube has been designed to securely hold the tube during the impact. The diameter of the rod (17 mm) and the weight (0.27 kg) were chosen to match the stress level of the hemispherical impact. STF was filled to the same level (31mm) and a small concentration of black SiO_2 microparticles (<0.1% by weight) were added to suspensions as a dye to track displacement of different parts of the fluid. Speed camera Phantom Miro M120 was used at 7300 fps resolution to capture the flow dynamics. MatchID digital image correlation (DIC) software was used for the flow-field displacement calculations of STF during impact. The vertical component of normal strain ε_x was calculated for each point of strain window per frame. Then, points with the same strain value were colored from red for the biggest value to yellow for the lowest. The maximum thickness of the third strain isoline (dark orange) in a vertical direction was used as a jammed front thickness value.

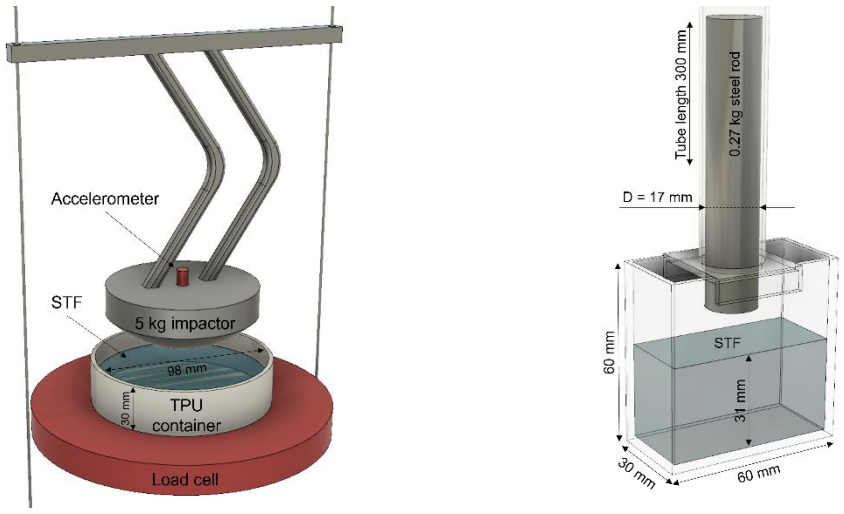

(**a**) (**b**)

Figure 4.2 Illustrations of low-velocity impact setups. (**a**) The drop weight impact setup with a custom 3d printed TPU container. All samples were filled to the 13 mm thickness level from the bottom. Height from the surface of STF to the tip of the hemispherical impactor was a controlled

parameter. (**b**) The acrylic glass setup which was used together with a speed camera for the flow field analysis during impact. All samples were subjected to the impact from the same height (327 mm).

4.3 Results and discussion

4.3.1 Rheological analysis of STF with different particles concentrations

Figure 4.3 shows rheological flow profiles of STF with three different concentrations of fumed silica (15, 20, and 25% by weight). Each graph can be split into three different zones: shear thinning, Newtonian, and shear thickening zones. The first zone is a shear thinning zone where the viscosity decreases with shear rate, the behavior in this zone is characterized by the net of three contributions: a Newtonian portion of constant viscous stress, an entropic portion of randomly colliding particles under thermal motion[161,162], and alignment of polymer chains due to polymer nature of the liquid medium. All STF demonstrated very mild shear thinning due to the low molecular weight of PPG, hence, higher conformational freedom of chains as well as an insignificant contribution from the entropic interactions. Next is the Newtonian zone with an almost invisible transition, the constant value of the viscosity in this zone represents the laminar properties of the fluid without effect from the particle's interactions[161]. In order to assess the type of shear thickening (CST or DST) present in our STF, we fitted shear stress-rate curves by power-law $\tau \sim \dot{\gamma}^{\alpha}$ in the shear thickening zone (Figure 4.3). According to Jaeger et al.[18] [1], $1 < \alpha \leq 2$ represents CST, where $\alpha > 2$ represents DST. In our case, $\alpha > 7$ for all three particles concentrations ($\alpha_{STF15\%} = 8.1 \pm 0.3$; $\alpha_{STF20\%} = 10.0 \pm 0.4$; $\alpha_{STF25\%} = 7.9 \pm 0.5$), which clearly indicates the presence of DST. Therefore, we can conclude that frictional interactions between particles are strong enough to trigger a discontinuous jump in shear stress. The nature of these strong frictional interactions is cumulative of contributions from hydrogen bonding between the silanol-rich surfaces and the highly anisotropic shape of fumed silica[47]. According to another study[46], the onset volume fraction of DST ϕ_{DST} for hydrophilic fumed silica suspension was found to be 6% which is below our lowest weight fraction (15% by weight corresponds to 7.2% by volume). Hence, this

study supports our results that DST is present in all selected weight fractions.

In the literature on STF, two parameters of flow rheology were extensively used and studied: critical shear rate and maximum viscosity. It is apparent that the critical shear rate decreases as particle concentration increase, as shown by the regions before an increase in viscosity. This supports hydrodynamic theory[107] which comes into play at the onset of shear thickening that at higher particle concentrations, stronger hydrodynamic forces are present due to shorter interparticle distance. Thus, a lower shear rate is required to overcome the repulsive forces, and shear thickening occurs at the lower shear rate at higher particle concentration. However, the difference between the values is insignificant. The points of maximum viscosity shown in Figure 4.3 increases with increasing particle concentration as frictional contact forces dominate and particle mobility is reduced. An interesting feature of maximum values is that their ratios follow the same trend as values in the Newtonian region and are roughly equal.

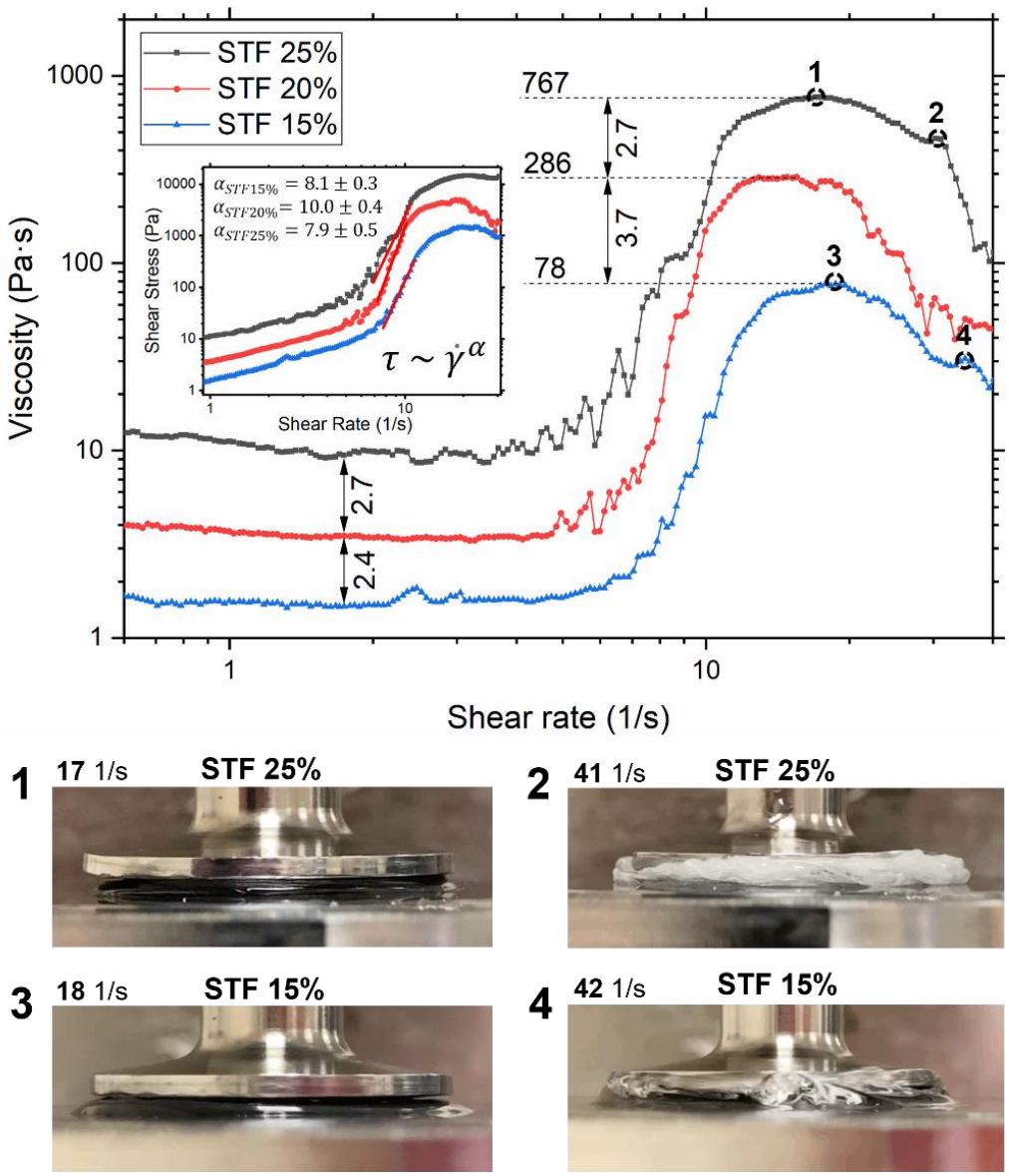

Figure 4.3 Flow rheological analysis of STF at three weight fractions. Viscosity as a function of shear rate in a parallel plates geometry with a 0.5 mm gap. Numbers on the arrows represent ratios of viscosities at different stages, the first two values at the bottom during the Newtonian stage, values on top ratios at the maximum viscosities. An additional graph inside the main is a shear stress-rate plot which was used for power-law fitting to establish the regime of shear thickening (DST or CST). (1, 3) Photos of STF 25% and 15% during flow tests at the maximum viscosity when fluid starts to slip off (17 1/s and 18 1/s, respectively), (2) when STF 25% becomes cloudy (41 1/s); (4) in contrast to STF 25%, STF 15% did not demonstrate any change in optical properties (at 42 1/s).

However, this portrayed maximum viscosity is irrelevant in depicting the true maximum viscosity of the STF as slipping occurs past a certain shear rate. Slipping occurs commonly in viscous suspensions due to the large velocity gradient between the plates and the fluid. During slipping, the fluid is no longer held between the parallel plates and the recorded viscosity will be much lower than the true viscosity[163]. Slipping decreases the surface tension between the fluid and plates. This fact combined with high centrifugal force at higher shear rates leads to loss of fluid between the plates, therefore, a drop in viscosity. Figure 4.3 (1,3) shows the STF samples confined between the parallel plates at maximum viscosity, it is observed that the STF samples started to flow out of the parallel plate boundary and onto the Peltier plate where their viscosities can no longer be recorded. It can be seen more clearly at higher shear rates (2 and 4 in Figure 4.3) that fluids slip and flow out. An interesting feature was noticed at shear rates beyond the maximum viscosity for STF 25%, the optical properties changed from transparent to translucent white. That happens because of the Tyndall effect. After a certain shear rate, particles start to agglomerate into clusters, where these clusters are large enough to start scattering visible light and make the colloidal suspension appear cloudy. The cluster formation is induced by hydrodynamic lubrication forces as was explicitly shown using fast confocal microscopy combined with simulations force measurements during rheological experiments[162]. On the contrary, STF 15% did not demonstrate any change in optical properties. Therefore, shear stress was not large enough to reach the certain size of hydroclusters for the scattering of visible light due to the lower concentration of fumed silica.

As aforementioned, we can conclude that the data recorded after slipping has occurred does not provide relevant information about the true viscosity of the STF, rendering the data after the fall in viscosity irrelevant. Shear stresses which are required to achieve a shear jammed state cannot be reached with a conventional rheometer due to failure modes[115].

In order to overcome this challenge a custom extensional test was designed as it allows to achieve higher shear stresses without any slippage of the fluid. Another advantage of extensional rheology is that it was found to be more relevant to the impact mechanics. It was shown earlier that extension of STF at rates higher than onset rates of jamming transition resembles mechanics of structural changes under impact[115]. It particularly supports the concept of jamming by shear where still and moving portions of fluid generate

strong localized shear which triggers formation of frictional networks of particles[119,164]. A modified extensional test was carried out in accordance with another study[96] with the sample holder and the rod dimensions doubled. Peak forces were recorded at each extension rate.

As seen in Figure 4.4, the general trend across all samples is an increase in peak force from 0.1 mm/s to 8 mm/s, followed by a plateau. The rate of increase in peak force, given by the gradient of the upward curve, is drastically higher with higher weight concentrations of fumed silica considering the peak force was plotted on a log scale. The ratios of plateau values resemble ratios between maximum viscosities in flow tests (Figure 4.3). Since at higher shear stresses the same trend is observed the maximum flow viscosities can be used for further interpretation of impact tests.

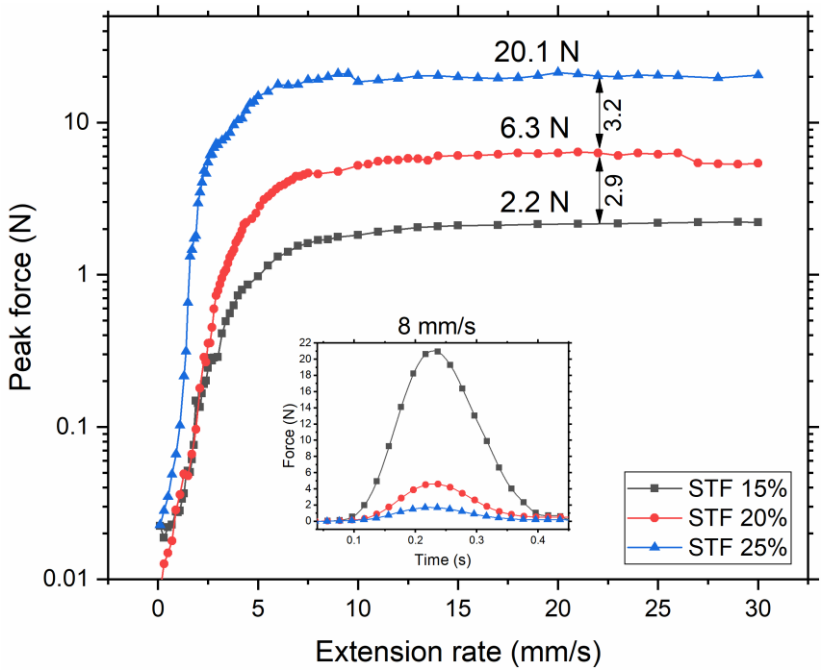

Figure 4.4 Extensional "pull-up" test, peak forces at each individual extensional rate test were plot against the rate, peak forces are plot in a log scale. Normal force profile at 8mm/s is shown in the middle of the figure, at this rate peak force values reach the plateau.

All curves reach a plateau around 8 mm/s. This value of peak force represents the maximum DST/SJ exhibited by the STF sample during the extensional tests. Comparing the peak force at 8 mm/s, the STF 25% sample shows 11.7 times higher peak force than that of the 15 % sample. In James et. al.'s experiment[96], the presence of shear jamming is

determined by a significant increase in normal force recorded at 8 mm/s. The peak force value of 12.0 N in PMMA/ITA suspension was shown to originate from SJ rather than just from shear thickening, whereas a non-SJ glass beads suspension demonstrated only 1 N of normal peak force at the same extension rate. Drawing parallels with our results (20.1 N for STF 25% at 8mm/s) it can be concluded that the high normal force in STF 25% is attributed to the presence of shear jamming. It is also worthy to note that a pulling force of 20.1 N for 25 wt% STF corresponds to stress exceeding 65 kPa, which is noticeably larger than that achieved during flow tests. This stress far exceeds stresses from the lubrication model or stresses which can be achieved with capillary forces[18,115,165]. Therefore, such high stresses originate from the frictional interaction between the particles. Sterically dispersed particles need to overcome repulsive forces to get in contact with each other which causes a drastic increase in peak force.

4.3.2 Low-velocity impact behavior of STF

Drop weight impact test was used to analyze the impact response of STF in the low velocities range. 13 mm thick layer of STF was subjected to six different impact energies based on the height of a 5 kg hemispherical impactor. Peak forces of three STF with different fumed silica concentrations are present in Figure 4.5a. The peak forces were plotted on a logarithmic scale to correlate with rheological data. At 5 J all STFs demonstrated sufficiently low and close values of peak forces suggesting that impact was within their capacity. After 5 J curves start to move away from each other. The peak force of STF 15% increased over three times at 10 J with a relatively consistent growth after. The shape of the curve, however, suggests that there is a plateau to which this curve tends. STF 20% demonstrated almost linear growth until 20 J with the same trend as for STF 15% where peaks forces increase less and may eventually reach the plateau. This suggests that after 20 J STF reaches the maximum capacity to bear the impact with the aid of DST/SJ. On the contrary, STF 25% showed an almost linear increase in the whole range of energies suggesting that the maximum capacity of impact absorption has not been reached yet. This hypothesis can be proved if we analyze individual impact profiles at 30J (Figure 4.5b). STF 25% shows an almost linear increase in force with time where STF 20% and especially

STF 15% demonstrate exponential increase with sharp peak force. Judging by the force distribution over time STF 25% starts to absorb energy first (the slope of the force curve at the start of the impact is the highest). Therefore, impact absorption is “activated” the earliest in STF 25%. It is aligned with the fact that particles at higher concertation get in contact more easily triggering DST/SJ the earliest which provides massive impact dissipation (via friction between particles). However, additional tests will be conducted to understand the nature of impact dissipation. As it was suggested by the referee liquid medium alone (PPG400) was subjected to an impact of 30 J to evaluate the impact mitigation performance of PPG400 on its own. Surprisingly, we found that STF 15% and PPG400 curves coincide, demonstrating the same peak forces and the same distributions. As it was said earlier the impact absorption capacity of STF 15% is limited to 5 J since it demonstrated a jump in a peak force at 10 J. Therefore, since impact bearing capacity was far exceeded at 30 J for STF 15% DST/SJ and/or hydrodynamic forces do not contribute to impact absorption enough to be noticed.

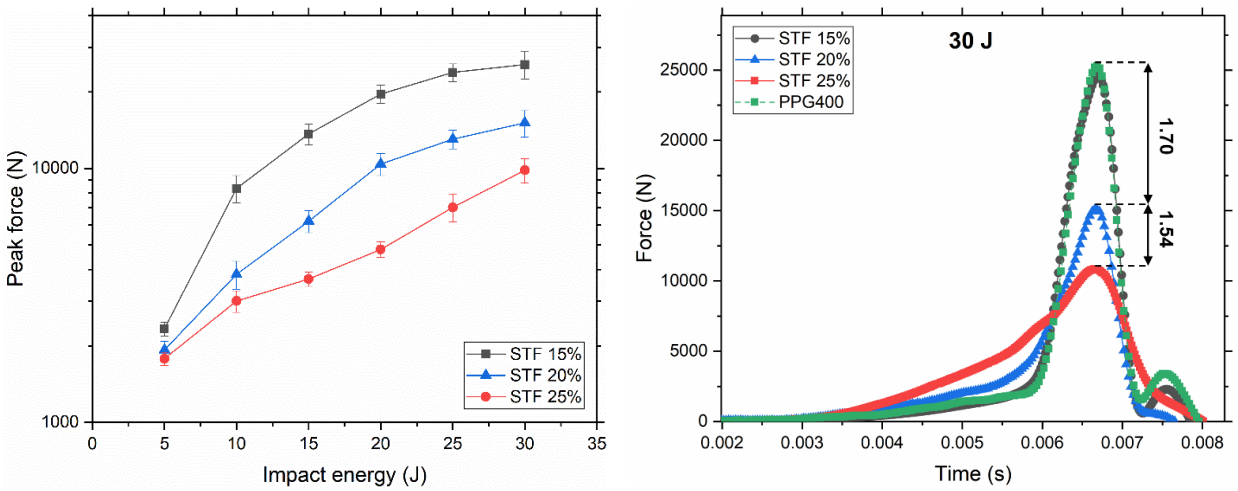

Figure 4.5 Results from the drop weight test with the hemispherical impactor. (**a**) Peak forces at six different energies with error bars. Percentages represent the weight fraction of fumed silica in STF. Each value is the average of ten tests with an error not exceeding 10%. (**b**) Normal force registered with the load cell as a function of time during 30 J impact. These curves are also the average over ten tests.

To explain this phenomenon, we conducted an impact test in a transparent container with

a speed camera. The great advantage of this type of STF is that due to the amorphous nature of fumed silica suspensions remains optically transparent at all concentrations. This allowed us to optically observe the flow of fluid during the impact. A small concentration of SiO_2 particles was added to suspensions to track displacements of different parts of fluid more clearly.

First, it was found that in the case of STF 25%, the rod started slowing down first, followed by STF 20%, and STF 15% started to slow down only near the bottom boundary (Figure 4.6a). The penetration depth of the rod linearly decreases with concentration. STF 25% demonstrated the best stopping efficiency with 19.4 mm depth, followed by 23.7 mm for STF 20%, and STF 15% gently hit the bottom at 30.6 mm depth. The speed of the rod before the impact v_0 is 2.4 m/s. The same behavior was demonstrated during the drop weigh test (Figure 4.6b) where the penetration depth of the impactor gradually increased from STF 25% to hit the bottom for STF 15%. Another resemblance between these two experiments is that the normal force starts to grow the earliest for STF 25% due to the formation of the jamming front which slows down and eventually stops the rod.

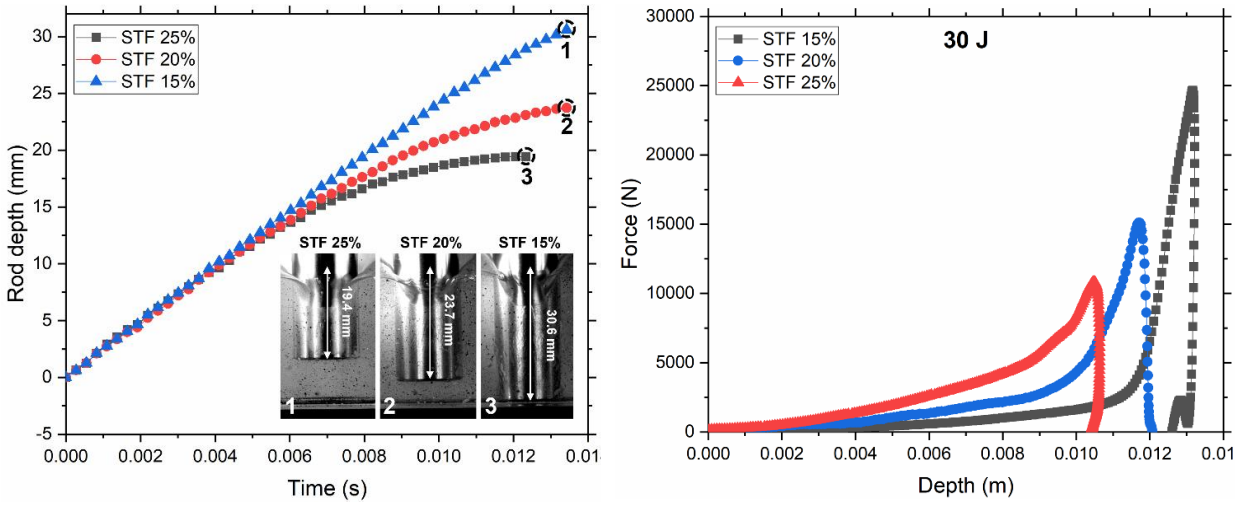

(**a**) (**b**)

Figure 4.6 Change in impactor depth for two types of impact tests and the resemblance between them. (**a**) Rod depth against time during speed camera impact test. The speed of the rod before the impact $v_0 = 2.4\, m/s$. Photographs from the speed camera when the rod is completely stopped (19.4 mm for STF 25%, 23.7 mm for STF 20%, and the rod hit the bottom for STF 15% at 30.6 mm depth). Recording of whole tests is shown in Supplementary Video 1. (**b**) Calculated force-

displacement (depth) profiles for drop weight test at 30 J. Displacement was calculated from the integration of the velocity-time plot, which in turn was obtained by integrating the force-time plot divided by the impactor weight.

The next step was to analyze the displacement of particles in suspensions during the impact. It was possible to calculate the solidification front dimensions during impact using DIC software. Jamming front thickness was plotted against the time for three concentrations (Figure 4.7). The complete videos of solid front formation can be found in Supplementary Video 1.

Three distinctive phases were observed during the impact. The first phase is the growth of the jamming front followed by the second one which is the propagation of the front. However, in the case of STF 25%, the first and second phases were combined into one. The front grew consistently all the way to the very bottom. STF 20% and 15% demonstrated propagation of the formed front to the bottom. However, the front of STF 20% kept growing in this phase whereas STF 15% did not. The third one takes place after the front reaches the boundary. The jammed layer is pushed against the boundary with the diffusion of particles to the sides due to compression. STF 25% solid front reached the boundary first followed by STF 20% and then STF 15%. We calculated jamming front propagation speed v_f at the first stage of the impact, it was found that velocities at all concentrations far exceed v_0. STF 25% $v_f = 12.3$ m/s which is 5 times faster than v_0; for STF 20% $v_f = 10$ m/s which is 4 times faster than v_0; and for STF 15% $v_f = 6.5$ m/s which is almost 3 times faster than v_0. The fact that the front propagation speed is much faster than the rod speed together with the extensional test results proves that the jamming is induced by shear, not by densification[115,120]. It should be noted that SJ was observed at all three concentrations at the impact stresses but only STF 25% could enter the SJ regime during extension tests due to much lower stresses.

In the earlier investigations of the STF under impact[120] it was shown that normal force starts to grow drastically when the jamming front reaches the boundary. In our case, the front of STF 25% reaches the boundary first creating strong resistance for the rod, which leads to a drastic increase above the normal force. This can be confirmed by analyzing the impact profile in Figure 4.3b, and it was obvious that normal force starts to grow much

faster (the slope value of STF 25% at the beginning of impact is two times higher than for STF 20% and three times higher than for STF 15%) than in the case of STF 20% and 15%. The front of STF 20% reaches the boundary later with a much thinner layer, therefore, it generates less resistance for the rod, and a significant part of the impact is transferred to the load cell. The front of STF 15% reaches the boundary the latest, with the thinnest front layer providing insufficient resistance to effectively absorb the impact; this leads to a slow peak rise of a normal force and a high value of the peak force. The visualization of the front at the moment of reaching the boundary is present in Figure 4.7 (1-3). By analyzing front thicknesses at this moment, we can directly correlate them to peak forces generated during the drop weight test (Figure 4.5b). The ratio of front thicknesses between STF 15% and 20% is 1.59 where 1.54 is the ratio between their peak forces; the ratio of front thicknesses between STF 20% and 25% is 1.61 where 1.70 is the ratio between their peak forces. Therefore, such proximity of values supports the notion that the main portion of impact is absorbed by the SJ solid plug beneath the rod pushing against the direction of the impact[118,120]. A much larger and more uniformly distributed deformation zone (in red color) can be generated by the impact rod found in the suspension with higher concentration of particles, which indicates a stronger shear jamming and more stable stress wave equilibrium in the suspension with higher particle concentration.

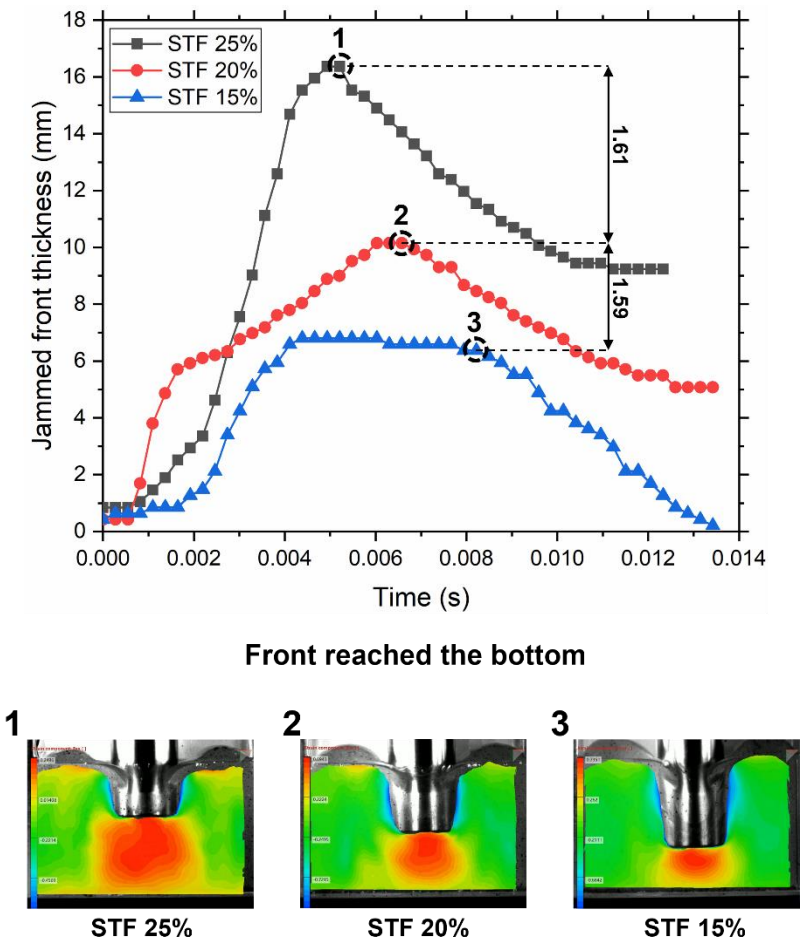

Figure 4.7 Jamming front propagation during impact. Calculated jamming front thickness during the impact of STF for three particles weight fractions. Front thickness was obtained measuring the maximum thickness of the third strain isoline (dark orange) in a vertical direction from the rod bottom surface. (1-3) Color-graded strain fields were calculated using DIC software. Red represents the highest displacement value where yellow is the lowest, green color represents no displacement. The red zone is the jamming front propagating towards the bottom at a speed faster than the speed of the rod. Captured pictures are front dimensions at the moment of reaching the bottom.

4.4 Chapter summary

Putting it all together, we confirmed the presence of DST at all weight fractions (15, 20, and 25%) using flow rheology. However, it was impossible to achieve jamming transition due to failure modes. Extensional rheology helped to reach higher stresses without fluid slippage. STF 25% demonstrated similar peak forces to another study where they

correlated it with the presence of SJ[96]. Low-velocity impact tests were conducted to study the mechanism of impact absorption and how SJ contributes. Owing to the optical transparency of fumed silica suspension, we directly observed the formation of the jamming front during impact. The speed of front propagation was calculated to be 3-5 times (3x for STF 15%, 4x for STF 20%, and 5x for STF 25%) higher than the impactor speed, which rules out jamming by densification. Therefore, it was induced by shear. Front propagation data was coupled with drop weight impact test results suggesting that the main portion of impact is absorbed once the SJ front reaches the bottom boundary. The efficiency of impact absorption was found to depend on fumed silica fraction through the thickness of the front between the rod and the bottom. The ratios of front thicknesses are almost equal to the peak force ratios which supports this hypothesis. Therefore, the high impact absorption of STF 25% over lower fractions was attributed to the formation of the SJ front growing much faster than the speed of the impactor to the boundary. This front reaches the boundary the earliest for STF 25% with the thickest jammed plug which helps to mitigate the impact most efficiently. The penetration depth of the rod reflected the impact absorption characteristics of our STF, where STF 25% demonstrated the lowest depth, followed by STF 20%, and finally STF 15%, however, STF 15% hit the boundary. This study provides new insights on a mechanism of energy absorption in PPG/fumed silica STF with direct observation of the jamming front formation during low-velocity impact. Interestingly, fumed silica suspension demonstrated SJ at $\phi \ll \phi_J$.

Key findings are summarized below:

- DST and jamming transition at as low as $\phi \cong 7.2\%$ and onwards (for the first time).
- The front propagation speed at all studied concentrations was found to be 3-5 times higher than the speed of the impactor rod, which rules out jamming by densification, and confirms that the propagation is triggered by shear.
- The main impact absorption begins when the jamming front reaches the boundary, creating a solid-like plug under the rod that confronts its movement. The efficiency of impact absorption was found to depend on fumed silica fraction through the thickness of the front between the rod and the bottom.

Chapter 5

Correlations Between Precursor Molecular Weight and Dynamic Mechanical Properties of Polyborosiloxane (PBS)

In this chapter, new correlations were discovered for five PBS synthesized from hydroxy terminated PDMS with different molecular weights. Si-O-B IR band intensities for all PBS follow the same trend with molecular weight as the number of PDMS hydroxy groups which confirms the full completion of the reaction. After synthesis, the molecular weight of PBSs remained almost the same, which indicates the absence of significant chain scissoring, polymerization, or crosslinking. This synthesis route allows to precisely control mechanical properties only based on the molecular weight of the precursor. During the rheological analysis, it was found that crossover point modulus follows the same trend as the number of PDMS hydroxy groups and Si-O-B band intensities. PBS demonstrated a linear increase in peak forces with molecular weight during the drop weight impact test. Based on results it was concluded that the low molecular weight of a precursor, hence, a high density of dynamic crosslinking is a primary requirement for effective protection against low-velocity impact.

---

*This section published substantially as "Correlations Between Precursor Molecular Weight and Dynamic Mechanical Properties of Polyborosiloxane (PBS)" in *Macromolecular Materials and Engineering* (DOI: 10.1002/mame.202100360). Reproduced with permission, Copyrights 2021, Wiley-VCH GmbH.

5.1 Introduction

Shear-stiffening gels (SSG) have attracted the attention of many researchers in the last decade due to unique viscoelastic properties, self-healing ability, ease of synthesis and affordability of raw materials.[13].The most common and utilized SSG is polyborosiloxane (PBS) which is a viscoelastic gel which behaves like a viscous liquid at low deformation rates due to dynamic relaxation of supramolecular bonds. However, once this rate exceeds the critical value, stickers do not have enough time to relax and reconnect, therefore, these temporary connections lock and behave as permanent crosslinking points.[13] During this transition, PBS changes its behavior from viscous to rubbery. This behavior is fully reversible.

One of the most important factors affecting properties of PBS is the molecular weight of PDMS chains. Molecular weight defines the density of dynamic crosslinks, hence, shorter chains results in a stronger shear-stiffening effect. However, the relationship between molecular weight and rheological properties is not as straightforward as it seems. Tang et al.[35] assessed the effect of molecular weight of hydroxy terminated PDMS on a resulting rheological property of PBS. They found that plateau elastic moduli first decreased and then increased with the molecular weight of the precursor due to a decrease in the number density of supramolecular interactions and dominance of topological entanglements (for molecular weights higher than entanglement molecular weight $M > M_e$). Seetapan et al.[124] demonstrated the same trend but for a narrower range of PDMS molecular weights, they found that relaxation time decreases with the precursor's molecular weight. There is no doubt that the molecular weight of the precursor is one of the most important parameters affecting all final mechanical properties. However, rheological analysis was the only type of mechanical investigation in these studies. An additional mechanical investigation needs to be done since rheology covers only a narrow range of testing conditions, resulting in unknown behavior in many real-world applications.

One of such real-world applications of PBS is impact protection. Due to unique self-healing and shear-stiffening properties, PBS was found to be particularly useful in impact protective equipment, such as D3O^{TM} foam, which is one of the most known applications of PBS in the market (it is PU foam with PBS as an additional protective compound).[77]

PBS is also found in other foam-based composites,[81,82] Kevlar-based composites,[20,40] and double network composites.[36,37,124] Despite the wide range of various PBS composites for impact protection, the potential of PBS itself has hardly been studied. This might be due to complications with the molding of PBS for real applications since it flows at low deformation rates. Wang et al.[17] investigated PBS filled with magnetic particles under high strain rates using modified Split Hopkinson Pressure Bar (SHPB). They found that energy absorption was attributed to two transitions, from liquid to elastic and elastic to glassy. The transition from the rubbery to the glassy state could be studied only using impact techniques such as weight drop impact tests and SHPB as it happens at rates unachievable by a conventional rheometer. This transition is a result of the simultaneous breakage of many supramolecular interactions.[20,141] It significantly contributes to overall energy absorption when rates exceed the critical value at which supramolecular bonds break.[17,32] In another study, Zhang et al.[125] demonstrated that during a low-velocity weight drop test, the impact area expanded five times when a PBS layer is used, which is a result of the stiffening front formation under impact. Moreover, they observed the formation of cracks which was found to be beneficial for impact absorption. However, the emphasis of these studies was put on testing conditions, not on a synthesis. Therefore, there is no clear explanation on how the density of dynamic crosslinking is correlated with impact absorption. This gap might originate from the scientific gap between chemistry research of PBS focusing predominantly on the synthesis part and mechanical research, which focuses on applications and testing conditions.

In this chapter, we are trying to bridge these two areas of PBS research by finding correlations between the molecular weight of PBS precursors (which defines dynamic crosslinking density) and dynamic mechanical properties using infrared spectroscopy, oscillatory rheological evaluation, and weight drop impact testing. This correlation would allow for the tailoring of mechanical properties of PBS based on the molecular weight of precursors for impact protection applications. The focus of this study is on how the density of supramolecular interactions affects impact protection since it has not yet been proven and is critically important for performance.

5.2 Materials and experimental methods

5.2.1 Chemicals and samples preparation

Five different hydroxy terminated PDMS were purchased from the Sigma-Aldrich company. Precursors were picked based on their kinematic viscosities (25, 65, 750, 2550-3550 and 18000-22000 cSt). Tetrahydrofuran (THF) of HPLC grade, boric acid, toluene, and hexane were purchased from Sigma-Aldrich and were used as received, without purification.

Dean-Stark water trap was used for synthesis of polyborosiloxane (PBS) as it was necessary to shift the chemical equilibrium of the reaction by taking out water from the system. First, hydroxy terminated PDMS which was used as a precursor was dissolved in toluene using magnetic stirrer for one hour. After that, BA was added in the deliberately excessive amount with respect to stoichiometric ratio (to avoid polymerization or crosslinking of the polymer) and stirred with dissolved PDMS for another hour. Next step was to heat up solution to temperature at which BA converts into pyroboric acid with release of water. However, the solution can only be heated to the boiling point of the solvent, in this case 110 ºC for toluene. Toluene was necessary for the reaction as BA easily hydrolyzes back by reacting with evaporated water and recrystallizes, forming big crystals. To prevent evaporated water coming back to the solution which can suppress the reaction, a Dean-Stark water trap was used. Another reason for using the water trap was to allow toluene to come back in to the system as the reaction temperature was above boiling point, forming azeotrope with water. System was kept at 140 ºC for 48 hours. After the synthesis step, PBS was extracted by evaporating toluene at reduced pressure and 60 ºC using rotational evaporator. Last step was to add hexane to extract PBS from the round-bottom flask with subsequent drying for 24 hours. Five different PBS samples were synthesized based on their precursors' molecular weight using the same procedure. For simplicity, synthesized samples were named PBS with the number accordingly to the kinematic viscosity of their PDMS precursors (PBS 25, PBS 65, PBS 750, PBS 2550, and PBS 18000).

5.2.2 Charaterization

Molecular weights of PBS and their precursors were characterized using gas permeation chromatograph (GPC) Agilent 1260 Infinity with TOSOH TSKgel GMHHR-M column. Results can be found in Table 1. Samples were dissolved in HPLC grade THF at a concentration of around 1-5 mg/ml, then they were filtered using 0.22 μm syringe filters. GPC of all samples were run in THF at 35 ºC with a flow rate 1 ml/min. Monodisperse polystyrene calibrants were used for a calibration curve.

A Fourier Transform Infrared Microscope (FTIR) Perkin Elmer Frontier equipped with Universal Attenuated Total Reflection (ATR) was used for functional group analysis. PBS samples were analyzed without any preparation, where PDMS precursors were prepared in a pellet form due to their low viscosity. A small drop of PDMS was added into the KBr powder and grinded before being placed into the hydraulic press to form a pellet. Each sample was scanned for a total of 32 times with a force gauge of 60.

Dynamic mechanical analysis (DMA) of synthesized samples were done using a modular compact rheometer Anton Paar MCR 501 in oscillatory mode. 25 mm steel parallel plates geometry was used with a set 0.5 mm gap for all tests. Low-amplitude frequency sweep tests were performed with 1% strain amplitude value in a range from 0.1 to 300 rad/s at 25 ºC.

Impact protection evaluation of PBS samples were carried out on the CADEX twin wire flying arm drop weight test machine with 44kN load cell. Cylindrical tip of 15 mm in diameter was attached to the flying arm with an overall weight of 1.6 kg. The illustration of setup is shown on Figure 5.1. The height of the dropping weight was the controlled parameter. Displacement values were calculated by first integrating force-time plot divided by arm weight to obtain velocity. Following that, a velocity-time curve was integrated to obtain displacement.

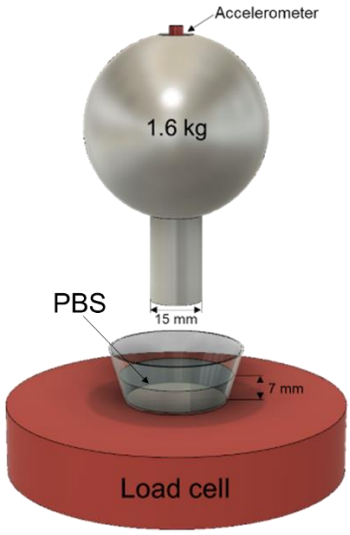

Figure 5.1 Drop weight impact test setup for PBS testing.

5.3 Results and discussion

5.3.1 Synthesis and FTIR analysis

Synthesis of PBS samples was done by heating the boric acid and hydroxy terminated PDMS in toluene at 110 ºC for 48 hours. A Dean-Stark trap was used during the reaction to prevent produced water from returning into the system as it could form an azeotrope with toluene, which would suppress the condensation reaction.[130] It was noticed that most of the evaporated water was collected in the burette within the first few hours. Tang et al. [2] demonstrated that the reaction had been completed in 12 hours at 120 ºC using an FTIR analysis of Si-O-B absorption peak intensity (1340 cm^{-1}) at different reaction times. After 12 hours, the intensity of the peak stayed constant which could be an indicator of the completion of the reaction. However, due to the difference in a synthesis approach, in our case, the system was kept for 48 hours to ensure the reaction was complete.

After extraction and drying steps, PBS samples were analyzed using gel permeation chromatography (GPC). The results of the GPC analysis are shown in Table 5.1, the molecular weights of the precursors are given for comparison. The molecular weight of PBS 25 remained unchanged, which indicates the absence of polymerization or crosslinking between PDMS chains on the one hand and the absence of chain scissoring

on the other. In the case of PBS 65 and PBS 750, the molecular weight slightly decreases with an increase in the polydisperse index. This suggests that there is minor chain scissoring, however, polymerization and crosslinking are absent. PBS 2550 and 18000 demonstrated similar molecular weight values with an increase in PDI, which indicates the absence of noticeable chain scissoring or polymerization. In the study by Liu et al.[28] it was shown that molecular weight of PBS dropped more than ten times after synthesis at 190 ºC due to chain scissoring. Therefore, it can be concluded that there are no traces of significant chain scissoring or polymerization for all samples.

Table 5.1 Molecular weight evaluation of PDMS precursors and synthesized PBS samples.

Precursor name	M_n, kg/mol	M_w, kg/mol	PDI	Number of -OH groups, mol/g [a)]
PDMS 25 cSt	0.7	1.0	1.4	2.9×10^{-3}
PBS 25	0.7	0.9	1.3	-
PDMS 65 cSt	6.3	9.0	1.4	3.2×10^{-4}
PBS 65	3.5	6.8	2	-
PDMS 750 cSt	28.8	36.7	1.3	6.9×10^{-5}
PBS 750	18.8	32.7	1.7	-
PDMS 2550-3570 cSt	38.3	54.4	1.4	5.2×10^{-5}
PBS 2550	35.2	63.0	1.8	-
PDMS 18000-22000 cSt	61.5	94.5	1.5	3.1×10^{-5}
PBS 18000	54.3	111.3	2	-

[a)] Calculated based on M_n of precursors, $N_{OH} = 2/M_n$.

At the next step, the change in IR transmittance was analyzed using an FTIR spectrometer. It was expected to see a change in two peaks in PBS samples compare to PDMS precursors. In Figure 5.2, a synthesized PBS 25 sample was compared with its precursor (PDMS 25) in terms of IR transmittance. First, PDMS 25 spectra demonstrated two O-H peaks, one corresponds to a non-hydrogen bonded (free) band with a peak at 3700 cm^{-1} and another corresponds to an intermolecular hydrogen bonded band with a peak at 3290 cm^{-1}.[166] Based on the intensity difference of these two peaks PDMS hydroxy end groups are susceptible

to intermolecular hydrogen bonding with each other. O-H bands fully disappear in PBS due to condensation reaction between PDMS and BA hydroxy groups.[126] This reaction leads to a formation of Si-O-B bonds which links PDMS chains together. A new Si-O-B band is formed with a peak at 1335 cm^{-1} together with a B-O-B band with lower intensity at 1380 cm^{-1} (Figure 5.2) due to a partial condensation reaction between BA molecules.[126] The Si-O-B band represents a covalently linked borono group to the PDMS chain ends. These groups behave like stickers due to their supramolecular interaction. Therefore, the unique shear-stiffening properties of PBS are the results of the presence of these sticker groups.[28,35,130]

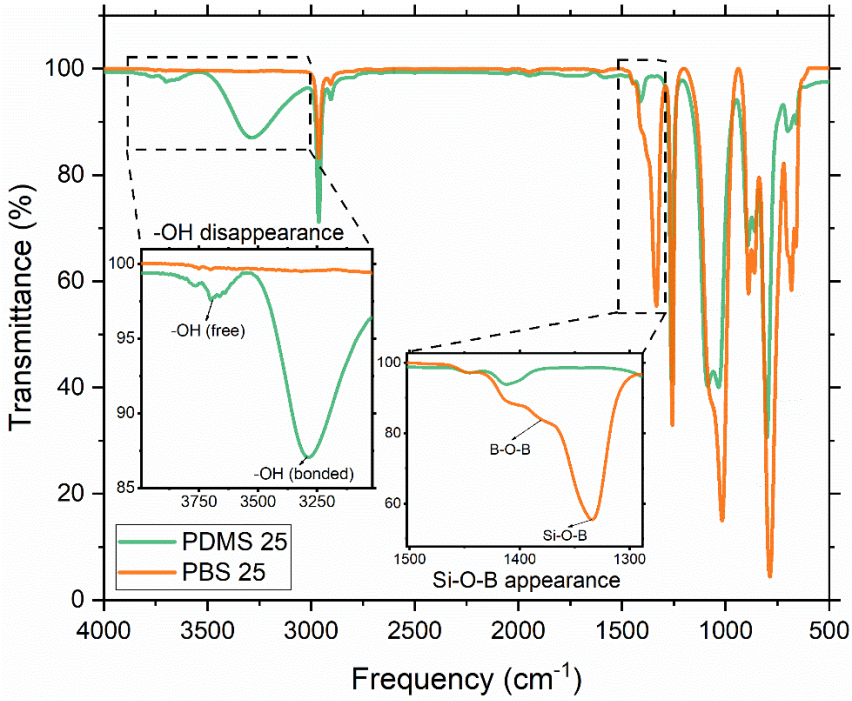

Figure 5.2 FTIR spectrum of PBS 25 plotted against PDMS 25

Zinchenko and co-workers[126] proposed three possible structures which can be formed during this reaction (Figure 5.3). Structure I is the result of the direct condensation reaction between hydroxy ends of PDMS and BA where the other two involve additional polymerization of BA molecules which may result in a formation of cyclic PBS molecules (structure III). The presence of a B-O-B shoulder on Figure 5.2 is evidence of additional polymerization between BA molecules which may result in the formation of structure II.

However, it was suggested in a more recent study[28] that polymerization of BA molecules is based on a condensation/hydrolysis equilibrium. It means that BA polymerization/depolymerization depends on the humidity and is reversible. But BA ends covalently linked to PDMS remain the same despite the external conditions.

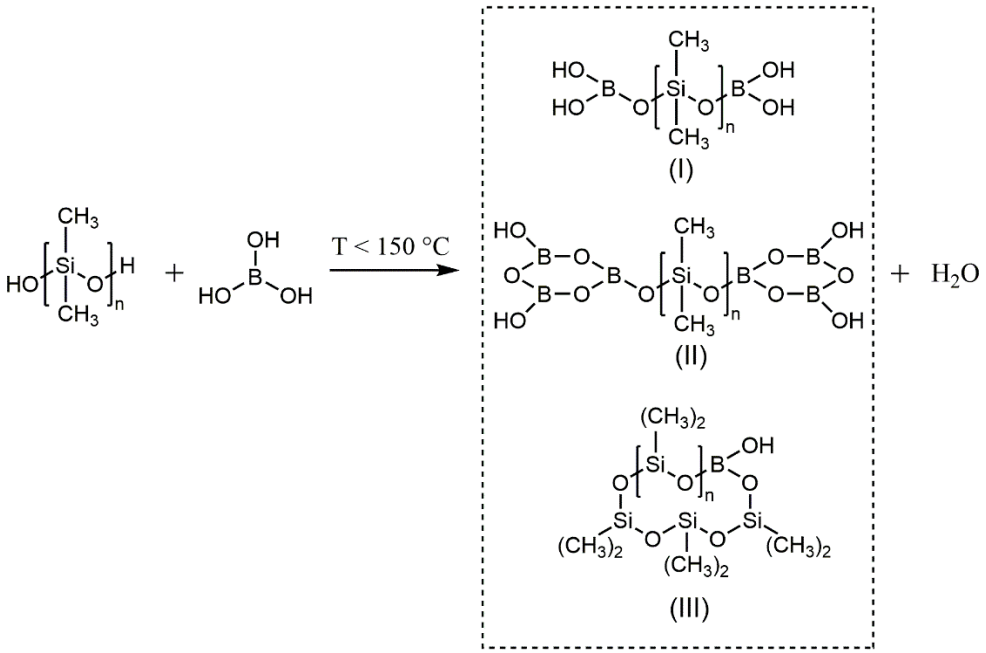

Figure 5.3 Chemical reaction of PBS synthesis with three possible structures proposed by Zinchenko and co-workers.[126]

Boric acid can also act as a crosslinker for PDMS chains, one BA molecule can react with one, two, or three chains at the same time. However, in the case of condensation synthesis this depends on the stoichiometry between the hydroxy groups of BA and PDMS. Since in our case BA was added in a knowingly excessive amount, there was no additional polymerization via BA bridges which was confirmed by GPC. All PBS samples were easily dissolved in THF and chloroform which is additional evidence of the absence of the covalent 3D network. In one study,[37] where the same synthesis route was used molecular weight less than doubled due to lower amount of BA closer to stoichiometric ratio. In another work,[167] where PBS was synthesized using Piers-Rubinsztajn reaction, the molecular weight was increased by slightly more than two times and was dissolvable in common solvents.

The same trend was observed for the rest of the synthesized samples and their precursors in the IR spectrum. Therefore, we can conclude that in our PBSs only structures I and II are present. The next step was to analyze the difference in intensity of Si-O-B band peaks between PBS samples. This difference can be clearly seen in Figure 5.4a, where intensity gradually decreases from PBS 25 to PBS 18000. $Si(CH_3)_2$ peak was chosen as a reference peak as it barely changes during the reaction.[28] PBS 25 showed the highest intensity of Si-O-B peak due to low molecular weight, hence, a large number of covalently linked sticker groups. The same was observed for the B-O-B peak which is an indication of additional polymerization of BA into bigger complexes such as Structure II in Figure 5.3. PBS 65 is next by intensity due to a lower number of sticker groups with barely visible B-O-B shoulder. Peak intensities of three other PBS are very close to each other but demonstrate much lower intensities visible using magnification.

If we consider how the number of hydroxy groups in PDMS is changing with molecular weight and compare it with the change in Si-O-B peak intensities, there would be a clear correlation (Figure 5.4b). Hydroxy content N_{OH} is a reciprocal function of molecular weight M_N:

$$N_{OH} = 2/M_N, \tag{5.1}$$

as well as Si-O-B peak transmittance follow the same relationship. Therefore, we can conclude that number of sticker groups, hence, the density of supramolecular interactions increases with the number of hydroxy groups of PDMS. This correlation confirms the hypothesis that the main reaction is the condensation between hydroxy groups of BA and PDMS and that there is minor to no scissoring of PDMS chains. This discovery allows one to precisely control properties of the PBS only based on the molecular weight of its precursor. This correlation can be further used for the analysis of mechanical properties.

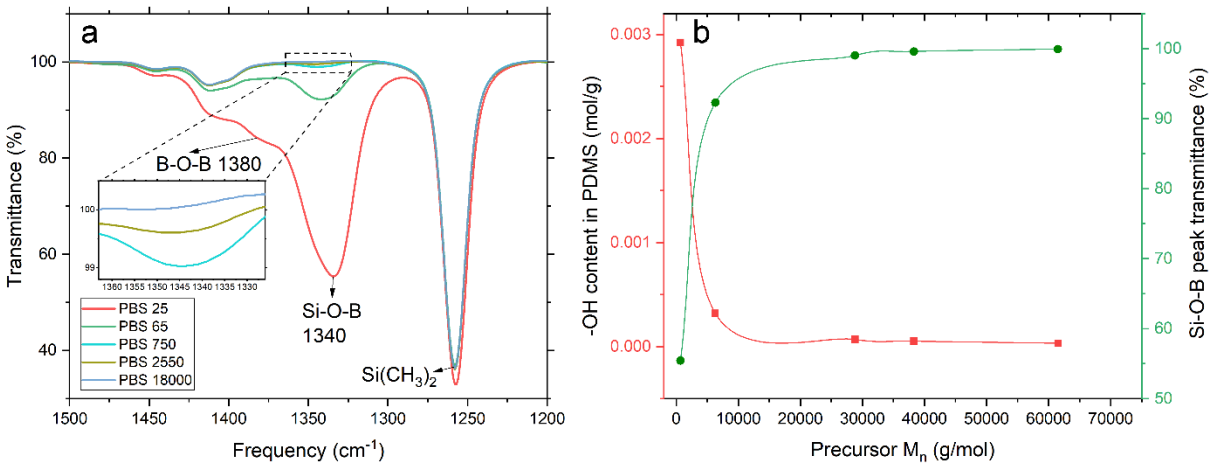

Figure 5.4 (**a**) FTIR spectrum of five synthesized PBS samples with change in Si-O-B peak intensity. (**b**) Correlations between number average molecular weight of precursor, -OH content and Si-O-B peak FTIR intensities.

Another important aspect of the synthesis is the temperature. It was shown before[28,126] that PDMS chains possess random scission at temperatures higher than 150 ºC in the presence of BA. Scissored ends react with BA, introducing $B(OH)_x$ sticker groups to PDMS chains. However, since it is a random process, it is hard to predict obtaining properties of PBS. Therefore, in this study, PBS was synthesized from hydroxy terminated PDMS at a temperature lower than 150 ºC, to precisely control the final properties of synthesized PBS since only hydroxy ends participate in the reaction. This approach allows one to assess most of the properties only based on the molecular weight of the precursor.

One type of supramolecular interaction present in PBS is the Si-O: B dative bonding which is covalent in nature but is reversible. Oxygen from the main PDMS backbone shares an electron pair with boron atoms.[13,128] This type of interaction acts as a temporary crosslink with the ability to relax and reconnect. Two bands at 865 and 700 cm^{-1} represent fingerprint bands of this type of bonding on the IR spectra (Figure 5.5).[128,167] Another type of supramolecular interaction is the hydrogen bonding between sticker groups, this interaction exists only in the presence of an unreacted hydroxy group in BA molecules. This interaction is represented in two bands at 890 and 681 cm^{-1}.[37] These two frequencies are fingerprints of the B-O-H band and are present in pure BA (Figure 5.5). Intensities of these two peaks change in the same fashion as the Si-O-B band from the highest value for PBS 25, to almost invisible peaks starting from PBS 750 due to the absence of polymerization and

crosslinking.

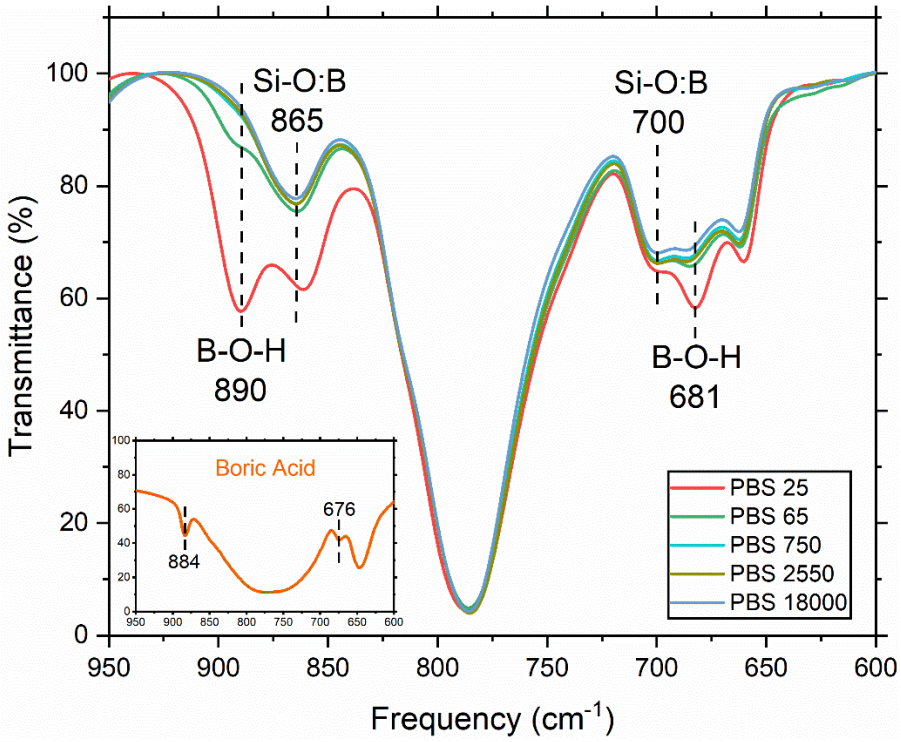

Figure 5.5 FTIR spectra of PBS in the fingerprint region with two bands representing Si-O: B dative bonding and two bands representing B-O-H band which is prone to form hydrogen bonds with each other.

An illustration of the diagram of all interactions is shown in Figure 5.6 based on the obtained results and the literature. It was confirmed that the density of supramolecular interactions decreases with increasing molecular weight of the precursor due to borono modification of the chain ends with no significant chain scissoring, polymerization or crosslinking.

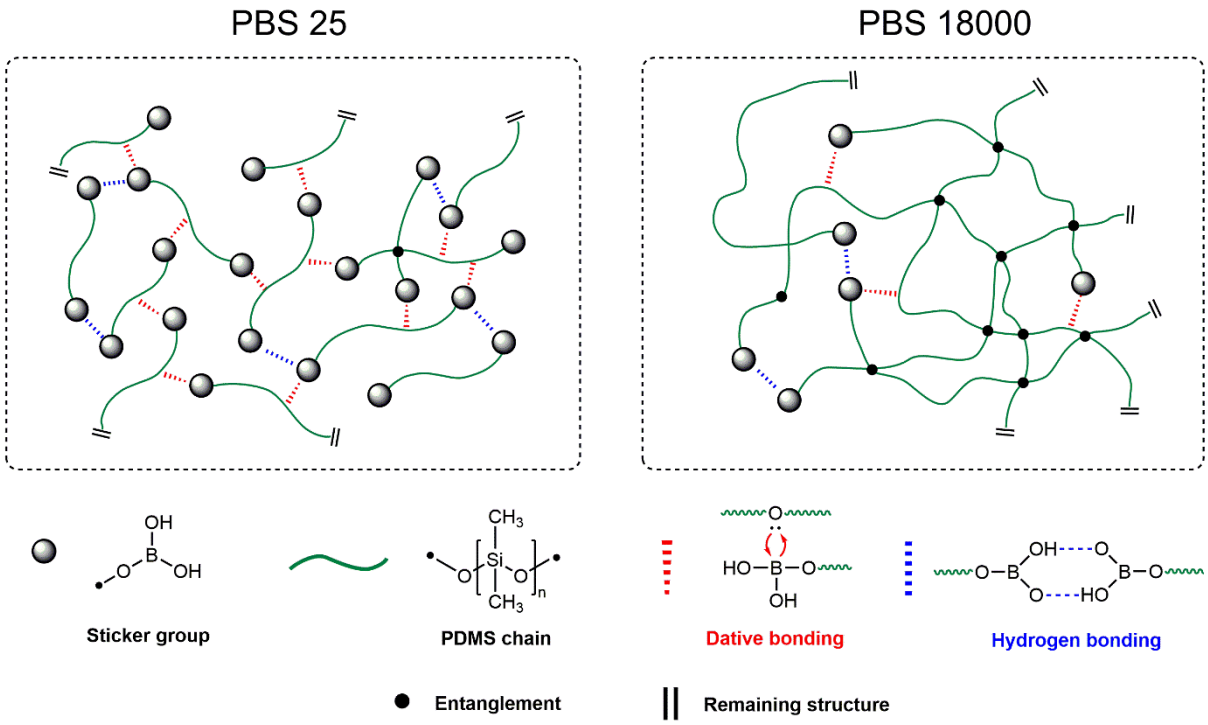

Figure 5.6 Schematic illustration of molecular structures and interactions of PBS 25 and PBS 18000.

5.3.2 Oscillatory rheological analysis

In this study, synthesized samples were analyzed using oscillatory shear tests to assess the influence of a number of sticker groups of PDMS on dynamic properties. Results of dynamic mechanical analysis (DMA) of all five PBS samples can be found in Figure 5.7 where storage *G'* and loss modulus *G"* represent elastic and viscous components of PBS, respectively. The crossover point (CP) represents the intersection between *G'* and *G"* or, in other words, transition frequency at which elastic component starts to dominate. Before comparing differently synthesized PBS with each other, it is important to explain the chemical reasoning for such unique viscoelastic behavior. PBS is known in literature for its frequency-dependent viscoelastic behavior (or shear-stiffening behavior), at low frequencies PBS demonstrates liquid-like behavior with higher values of *G"* than *G'*. However, after transition frequency, *G'* takes over and starts to dominate, resulting in a solid-like behavior at higher frequencies. This change from viscous to elastic behavior is attributed to the Si-O: B dative bonding[13,128,130] and hydrogen bonding of sticker

groups[14,17,35] or, in other words, reversible supramolecular interactions. At low frequencies, there is enough time for stickers to relax and reconnect, allowing PBS to flow and behave as a viscous liquid. However, once frequency exceeds the transition value, stickers "lock" and recombination is no longer possible, which is when PBS starts to behave as an elastic solid (like chemically crosslinked rubber).

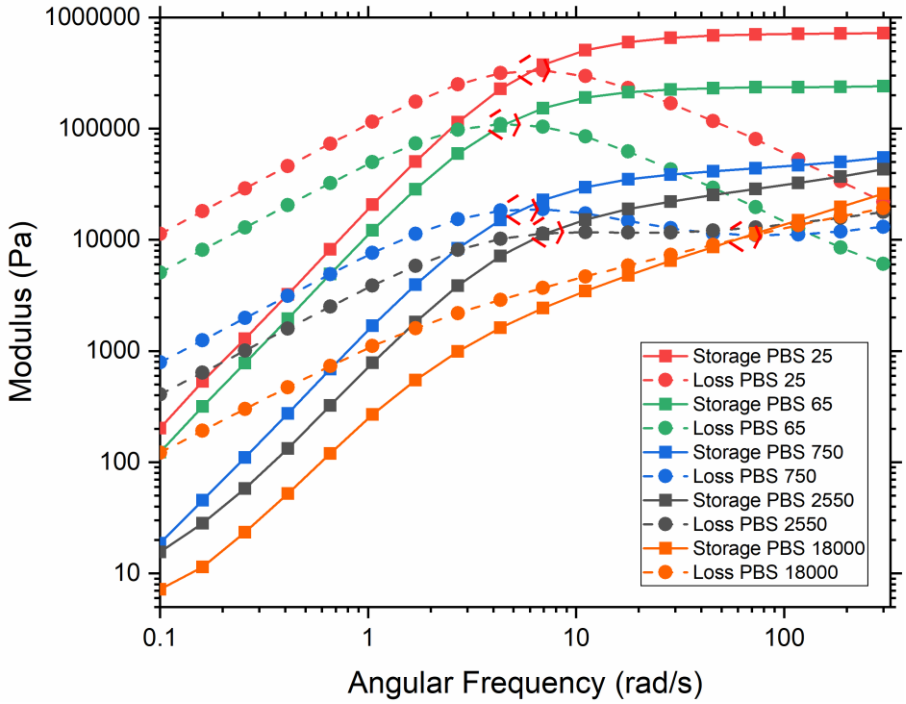

Figure 5.7 Storage modulus *G'* and loss modulus *G"* of five synthesized PBS samples obtained during small amplitude oscillatory test.

Analysis of loss and storage modulus of all PBS samples should be split into two parts, before CP and after. All loss modulus curves before CP demonstrate similar behavior with the same slope value but gradual elevation from lowest to highest viscosity, hence, the molecular weight of the precursor. A similar trend was observed for storage modulus curves. Before CP, all PBSs are in a viscous state without contributions from supramolecular interactions as they have enough time to relax and reconnect. Thus, the position of curves is defined by their viscosity. The difference is easier to see using *tan(δ)* which represents the ratio between *G'* and *G"* at a specific frequency (Figure 5.8a). The curves are almost the same before CP but start to differ after CP. Reversed CP frequency is a relaxation time

τ_c which characterizes the time scale of the process, and, in our case, the time for stickers to relax and reconnect. Obtained τ_c are 1.04 s, 1.40 s, 1.21 s, 0.90 s, and 0.10 s for PBS 25, 65, 750, 2550 and 18000, respectively. Starting from PBS 65, relaxation time decreases which is in line with other studies.[124,125] This trend is observed because, with a higher number of stickers, more time is required for them to relax and reconnect. However, PBS 25 deviates from this trend. The reason can be found in the theory of supramolecular polymers. Rubinstein and Semenov[168,169] developed a model for the prediction of the relaxation time of unentangled supramolecular polymers. In their model τ_c is proportional to the effective jump time of stickers τ_b times square number of active stickers per chain. Since PBS 25 and 65 have the same number of active stickers per chain (we assume each chain has two stickers) the only difference is τ_b value. This value depends on how easy it is to find a vacant sticker point to connect to. PBS 25 is able to find neighboring stickers more easily due to their higher density, which significantly reduces relaxation time. However, this model can be applied only for unentangled supramolecular polymers.

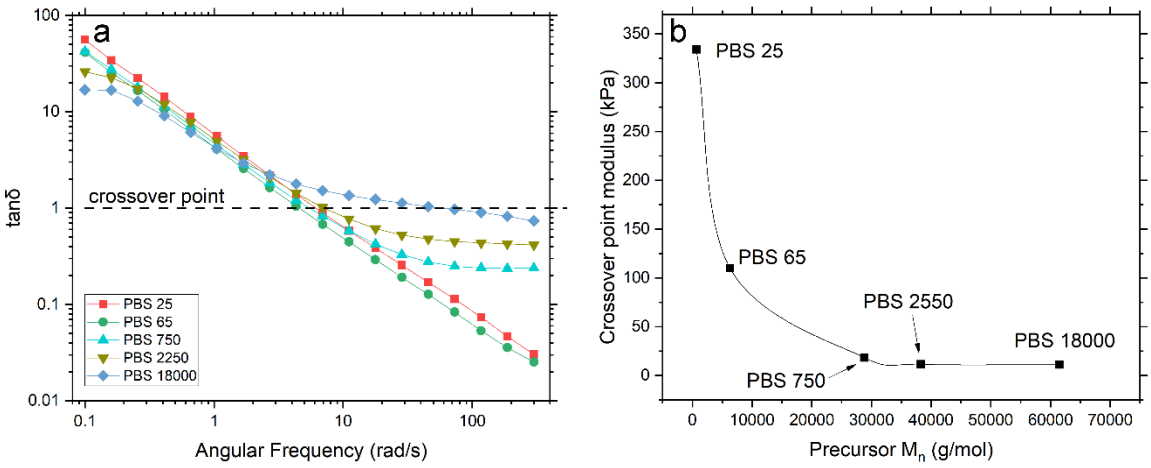

Figure 5.8 (**a**) Tan(δ) curves for all PBS samples. (**b**) Relationship between crossover point modulus and molecular weight of precursors.

After CP viscoelastic behavior between PBS starts to differ, PBS 25 and 65 demonstrated a typical viscoelastic behavior of liquid well described by Maxwell model (spring connected in a series with a dashpot), however, the rest of PBS deviates from this model due to appearance of topological entanglements.[124,130] Precursors of PBS 25 and 65 are below entanglement molecular weight (M_e = 12 kg/mol)[170,171] where the rest are above

which justifies their deviation from the model. Consequently, the behavior of PBS 25 and 65 is defined only by supramolecular interactions but starting from PBS 750 contribution of entanglements to the viscoelastic behavior gradually increases (due to an increase in entanglement density and decrease in the number of stickers). The presence of the plateau elastic modulus G_e is an essential feature of the Maxwell model, as it characterizes elasticity of PBS when all physical crosslinks lock and behave as chemical crosslinks. Analyzing the storage modulus curves of PBS, only PBS 25 and 65 have a clear plateau, while for the rest, the slope gradually increases from PBS 750 to PBS 18000. The same behavior is typically observed in most of the polymers above entanglement molecular weight due to the chain reptation.[172] Observed decrease in the rubbery plateau level (on a Figure 5.7) from PBS 25 to PBS 18000 is due to a change in the mesh size of the network (as the density of supramolecular interactions defines the mesh size).[31]

Since only two PBS show plateau of elastic modulus, CP modulus value was used for the molecular weight correlation plot (Figure 5.8b). The graph aligns with the number of hydroxy groups in the precursor and Si-O-B IR band intensity (Figure 5.4b). It follows the same reciprocal relationship as molecular weight increases, hence, the number of stickers. This correlation provides additional evidence of the importance of the supramolecular mesh density on rheological properties. Therefore, the lower the molecular weight of the precursor, the stronger the shear-stiffening performance. In another study,[28] where PBS was synthesized via a different route (via thermal chain scissoring), the value of the crossover point modulus coincides with the value in our work between two PBSs of close molecular weights (rPBS1 from their work and PBS 65 from ours). This fact supports the hypothesis that the mechanical properties of PBS are largely determined by molecular weight, regardless of the synthesis route. This knowledge would be very useful for designing the synthesis of PBS with respect to mechanical requirements.

5.3.3 Impact protective properties of PBS

All tests were carried out using a weight drop impact tester with a total weight of 1.6 kg and a cylindrical steel impactor with a diameter of 15 mm. All samples were subjected to the same impact energy of 1.6 J. Impact profiles are presented in Figure 5.9a. PBS 25 and

65 demonstrated the best protective capabilities with low peak forces of 900 N and 960 N, respectively, and broad force distribution over time, which is a sign of good impact protection. However, with higher molecular weight, PBS showed much higher peak forces (1680, 1790, 2350 N for PBS 750, PBS 2550, PBS 18000, respectively) and narrower distributions. The increase in force fluctuations arises from the repeated impact during the loading and inertia effects of the system.[173] Despite the oscillations, the first peak is the most crucial for protection because it represents the response to the impulse and the most energy is absorbed during it.

To correlate impact performance with molecular weight, we can plot peak forces versus the molecular weight of precursors (Figure 5.9b). There is a clear rise of the value which agrees with the original hypothesis that stronger shear-stiffening (due to higher density of supramolecular interactions) provides better impact protection. During the impact, mechanical energy is absorbed on a "locking" and breaking of supramolecular bonds. However, with an increase in molecular weight, the number of supramolecular bonds drops, and the entanglements start to contribute to the overall energy dissipation with subsequent dominance.

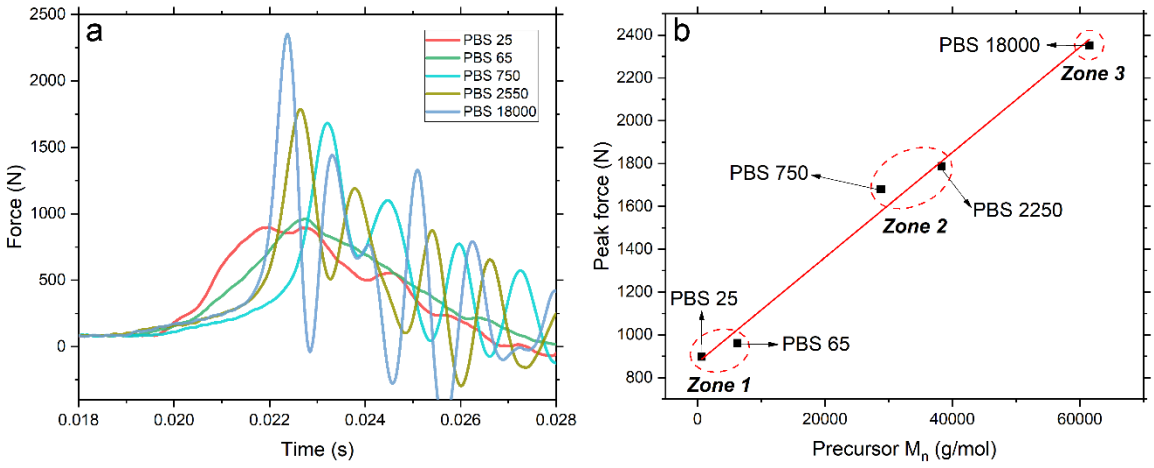

Figure 5.9 Drop weight impact test: (**a**) Normal forces of all PBS samples (impact energy 1.6 J), (**b**) linear increase in peak force with the molecular weight of precursors with three different zones corresponding to the specific molecular weight range (red line is a linear fit of all data points to highlight the trend).

The graph can be split into three zones. The first zone corresponds to the low molecular

weight of precursors (hence, PBS), the second to middle molecular weight, and the third to high molecular weight. The first zone represents the range of molecular weights which showed the best peak impact reduction, followed by almost twice the less effective zone of middle molecular weight and the least effective third zone with 2.5 higher peak force. Recalling Figure 5.4b, it was found that the number of sticker groups falls in a reciprocal relationship with molecular weight. Based on this fact, we can conclude that the peak force is increasing with a decreasing number of stickers.

For a better understanding of PBS behavior under the impact, displacements were calculated using accelerometer data by the integration of acceleration, followed by the integration of calculated velocity divided by the mass of the dropping weight. The results are presented in Figure 5.10a. Based on the maximum displacement values, PBS 25 showed the lowest penetration depth due to the strongest shear-stiffening effect among other PBSs. However, the rest of the samples did not show any clear trend.

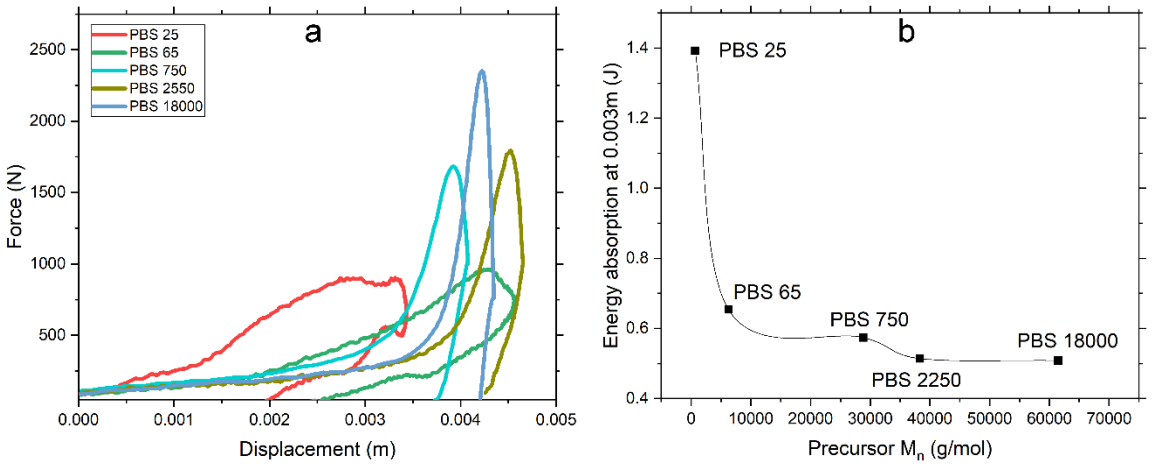

Figure 5.10 Drop weight impact test: (**a**) Force plotted against calculated displacement values, (**b**) the correlation plot of energy absorption at 3 mm indentation depth with the molecular weight of precursors.

Another important task was to analyze the change in force with a penetration depth as it represents the spatial distribution of the impact. Force displacement curves were integrated from the contact to 3mm penetration depth to obtain energy absorption. These values were plotted against the molecular weight of the precursor to show the difference in energy absorption at specific depths (Figure 5.10b). The plot shows the same trend as for the

number of sticker groups (Figure 5.4b) and CP modulus (Figure 5.8b). Stronger shear-stiffening behavior results in higher impact absorption due to more energy being spent on a phase transition, during which supramolecular bonds "lock". That explains the exceptional impact absorption of PBS 25 with the highest density of supramolecular interactions. Despite lower impact absorption, PBS 65 demonstrated close peak force, which means that the same amount of energy was absorbed, but over a larger area. Higher penetration depth confirms that. We need to remember that the thickness of the specimen affects impact absorption a lot, therefore, a lower thickness of PBS 25 would be required compared to PBS 65 for effective impact protection. This could be highly beneficial for reducing the size and weight of protective equipment.

Another interesting feature of the graph is how the unloading curve for these three samples is changing. PBS 25 and 65 showed a similar return where it is gradually decreasing from PBS 750 to PBS 18000. In this case, this return represents elastic recovery following the impact. It agrees with the fact that more dynamic crosslinking points are substituted with topological entanglements with the increase in molecular weight, which are partially viscous in nature. That results in a more liquid-like behavior with less recovery.

5.4 Chapter summary

Five different PBSs were synthesized from hydroxy terminated PDMS with different molecular weights and boric acid. They were synthesized at lower than random chain scission temperature (T < 150 ºC) in toluene using a Dean-Stark trap to separate toluene from water, as they tend to form an azeotrope. GPC analysis confirmed the absence of significant chain scissoring, polymerization, or crosslinking during reaction. Based on an FTIR analysis, the disappearance of a hydroxy group and the appearance of a new Si-O-B band has been confirmed. It was found that intensities of this band, hence, the number of dynamic crosslinks correlate with the number of hydroxy groups in PDMS, thus together with GPC results confirming the absence of chain scissoring.

During the rheological analysis of PBS, it was found that crossover point modulus correlates with molecular weight in the same fashion as Si-O-B IR band intensities. This confirms the hypothesis that Si-O-B bands represents density of supramolecular

crosslinking and that they are the primary reason for the unique shear-stiffening behavior of PBS. The plateau of elastic modulus was found to be ceasing with an increase in the molecular weight of the precursor due to the domination of topological entanglements. A clear plateau was present only in PBS 25 and PBS 65, for the other three samples slope of the storage modulus after the transition was found to gradually increase with the molecular weight.

A linear increase in peak forces was discovered during a low-velocity impact test, which corresponds with the rheological and IR evaluation of PBS. Zone 1, which corresponds to the molecular weight range from PBS 25 to 65, was shown to be the best for synthesis, in terms of shear-stiffening performance. It was found that energy absorption at a 3mm penetration depth was following the same reciprocal trend with molecular weight as the CP modulus and Si-O-B band intensities. PBS 25 showed the best impact protection with the lowest peak force and penetration depth. These results confirm the primary importance of molecular weight, hence, the density of dynamic crosslinking for protective properties of PBS.

Newly discovered correlations between molecular weight and dynamic mechanical properties highlight the importance of proper synthesis design and provide guidelines for researchers to tailor PBS properties based on molecular weight for specific applications. However, some research questions remain, such as the origins of supramolecular bonds which were debated in the literature due to contradictions with experimental data, as well as the contribution of rubbery-glassy transition at higher strain rates to total impact protection.

Results of this project significantly contribute to the research of impact absorption of SSG with the following key findings:

- Condensation synthesis allows precise control of the final properties of PBS by the right choice of PDMS precursor molecular weight.
- The density of dynamic crosslinking in PBS can be characterized by the intensity of the Si-O-B IR band.
- Crossover point modulus, normal peak force, and energy absorption are in a linear relationship with the number of dynamic crosslinks.

- Efficiency of impact dissipation is defined by the dynamic crosslinking density together with the required energy to break all dynamic bonds.

Chapter 6

Mechanism of dynamic crosslinking in Polyborosiloxane (PBS)

This chapter provides novel insights into the mechanism of dynamic crosslinking in PBS which has been debated for 70 years. The formation of Si-O-B dynamic covalent bonds with their associative exchange with neighboring hydroxyl-bearing moieties (free silanol, water, alcohol, etc.) is behind gelation and unique viscoelastic properties of PBS. FTIR and solid-state ^{11}B NMR analysis demonstrated no evidence of hydrogen or dative bonding. The formation and breakage of Si-O-B bonds have a low energy barrier, therefore, can be easily formed and exchanged at room temperature. Viscoelastic properties can be tuned by the right choice of boron B-O functionality which results in n-functional dynamic crosslinking through $(\text{-Si-O})_n$-B bonds.

6.1 Introduction

Polyborosiloxane (PBS) has been known for more than 70 years, yet the origins of its unique properties are still in debate in the literature. PBS was first produced as the main ingredient of a famous putty toy – Silly Putty™, back in 1947 by a researcher from Corning Inc.[142]. Many years later, researchers started paying attention to the intriguing viscoelastic properties of PBS and how they can be utilized for various applications, such as impact protection[13], flexible electronics[174–177], sensors[33,39,135,138,178,] etc. Early investigations into the mechanism revealed that unique stiffening behavior originates from the presence of dynamic bonds that form upon reaction with boron compounds (boric acid, trimethyl borate, etc.). Several mechanisms of dynamic crosslinking were proposed during these 70 years of research, such as hydrogen bonding between borono end-groups[28,126,127], dative bonding between boron and oxygen[42,43,143], boroxine formation, and oxygen ligands exchange[29]. In parallel, a whole new brunch of boron chemistry research has been developed, which brought new insight into the possible mechanism of boron reversible crosslinking in polymers[44,152,156]. Some of the most elaborated mechanisms are the reversible formation of boronic esters and boroxines. Boronic esters could be formed through dehydration of boronic acid in the presence of available diol groups; this reaction is reversible and can be even dynamic if the system is in equilibrium[153].

Furthermore, these esters could participate in a transesterification exchange with externally added diol molecules or even directly exchange between themselves (metathesis)[38,44,45,146,179]. Boroxines could also reversibly be formed through dehydration and participate in metathesis[44,156]. In both cases, the addition of Lewis base could facilitate and tune rates of boronic transesterification[180] and boroxine metathesis[44,158]. However, the vastness of boron chemistry complicates the determination of the dominant exchange mechanism in PBS.

This chapter aims to resolve the contradiction between various proposed mechanism of dynamic crosslinking in PBS and classify them from unlikely present to dominant. Various synthesis conditions, hydrolysis, and solution studies paired with FTIR and solid-state ^{11}B NMR are used to probe the possible contribution from different mechanisms. Besides, the

effect of B–O functionality on the viscoelastic properties of different MW PBSs is analyzed, providing additional hints on the mechanism.

6.2 Materials and experimental methods

6.2.1 Chemicals and samples preparation

Hydroxy terminated polydimethylsiloxane (OH-PDMS-OH) with three different kinematic viscosities (25, 65, and 750 cSt), boric acid (BA), phenylboronic acid (PBA), toluene, hexane, isopropyl alcohol (IPA), dimethylformamide (DMF), tetrahydrofuran (THF) of HPLC grade, chloroform, acetone, DI water, pyridine, and sodium sulfate were purchased from Sigma-Aldrich and used as received, without further purification.

Straightforward condensation between hydroxyl groups of OH-PDMS-OH and boron compounds was picked for the synthesis of PBSs. For a synthesis at room temperature (RT), PDMS oil was mixed with BA using a magnetic stirrer in a beaker until the magnetic bar could no longer rotate. Stoichiometric concentration between hydroxyl groups of BA and PDMS was calculated based on gas-permeation chromatography (GPC) MW data. For synthesis with heating Dean-Stark apparatus was used for all reactions to shift the chemical equilibria by taking away the water from the solution. Toluene was used as a solvent media as it forms an azeotrope with water produced during the condensation reaction. The geometry of the apparatus prevents any water from coming back into the system due to the density difference between water and toluene. They phase separate, and water stays at the bottom of the condenser tube where toluene is at the top, allowing it to flow back to the reactant solution. For each reaction, 10 g of OH-PDMS-OH was used and stirred in 150ml of toluene for 1 hour prior to the reaction, then a stoichiometric amount of boric compound was added to the solution (1:1 ratio between hydroxyl groups of PDMS and respective boric reactant) and stirred for another 30 minutes. The solution is heated to 140 ºC to make sure that all water produced during the reaction reaches the condenser. However, the actual reaction temperature is the boiling point of toluene which is 110 ºC. Such a low temperature of reaction prevents any degradation or any damage to the PDMS main chains. PDMS chains are prone to random chain cleavage at temperatures above 150 ºC and in the

presence of BA[28,] which we try to avoid due to the less controlled outcome of the reaction. The heated mixture was kept stirring for 24 hours to make sure all hydroxyl ends reacted. Six samples were synthesized B25, B65, B750, P25, P65, and P750. Samples were labeled according to the kinematic viscosity of PDMS and the first letter of the boronic compound. For example, in B25, B represents the fact that BA reacted with PDMS 25; P750 that phenylboronic acid reacted with PDMS 750. RT label was added to samples synthesized at room temperature without apparatus, such as B25RT. Upon completion of the reaction, some amount of water was found in the condenser tube with the highest amount after synthesis of PBA-based PBS (P25, P65). In the next step, we allowed the solvent to cool down to avoid hydrolysis with air moisture before drying it in the fume hood. After drying, some visible amounts of white solid residues were seen in samples, probably due to partial hydrolysis of boronic compounds. All samples were refined by dissolving them in hexane and filtering in a few cycles through 0.22 μm PVDF filters.

6.2.2 Characterization

A solvent study was performed by dissolving B25 in six different solvents (IPA, hexane, chloroform, acetone, DMF, and DI water), and the time to complete dissolution was measured. 2 g pieces of B25 gel were simultaneously placed in small bottles with 10 ml solvent and magnetic bar inside, then bottles were closed, the timer was started when the magnetic stirring of the solution began.

Gel permeation chromatography (GPC) was used for a determination of number-average molecule weight M_N of synthesized samples and PDMS precursors. Agilent 1260 Infinity with TOSOH TSKgel GMHHR-M column was used. Samples were dissolved in THF at 1 mg/ml prior to analysis and were run at a 1 ml/min flow rate. Monodisperse polystyrene calibrants were used for a calibration curve.

A Perkin Elmer Frontier Fourier transforms infrared (FTIR) microscope was used for the functional group analysis in Attenuated Total Reflection (ATR) mode. Spectra for each sample were scanned a total of 32 times with a force gauge varied (from 20 for liquid samples to 60 for gels and powders).

Rheological characterization was performed on Anton Paar MCR 501 rotational rheometer. 25 mm parallel steel plates were used for both oscillatory and flow analysis. Low amplitude

frequency sweep tests were performed for dynamic characterization of gel samples with a 0.5 mm gap setting and 1% strain amplitude. Liquid samples were analyzed in shear rate ramp tests with a 0.3 mm gap. All tests were conducted at ambient humidity and 25 ºC

Matrix-assisted laser desorption/ionization mass spectrometry with a time-of-flight detector (MALDI-ToF-MS) was used for a molecular weight analysis of individual chains in a positive linear mode. Super-DHB was used as a matrix, potassium iodide (KI), as an ionization agent to accelerate the ionization of analyte molecules. Both super-DHB and KI have dissolved in 1:1 v/v THF and water solution; analyte samples were dissolved in THF only. First, 1 µl drop of 10mg/ml super-DHB solution was placed on a sample pellet, followed by 1 µl drop of 1 mg/ml sample solution and 1 µl drop of 10 mg/ml KI solution right after. The slow evaporation of water promoted co-crystallization between analyte and matrix molecules.

All ^{11}B MAS NMR measurements were performed at 16.4 T using a Bruker 700 MHz Avance III HD spectrometer operating at a Larmor frequency of 224.7 MHz. All data were acquired using a Bruker 3.2 mm HXY probe which enabled MAS frequencies of 10 kHz. All 1D ^{11}B MAS NMR data were acquired with quantitative single pulse experiments using selective ('solids') $\pi/12$ pulses of 0.8 µs duration and delays of 200 s. Each spectrum was referenced against the IUPAC recommended reference of 15 % boron trifluoride etherate ($BF_3.Et_2O$) in deuterated chloroform ($CDCl_3$)(δ_{iso}= 0.0 ppm) via a secondary reference of sodium borohydride ($NaBH_4$) (δ_{iso}= -42.06 ppm).

6.3 Results and discussion

6.3.1 Synthesis and hydrolysis of B25

Synthesis of PBS gel is typically done through either condensation between hydroxyl groups of a boron compound and hydroxy-terminated PDMS[29,34,130] or grafting of boron compound into scissored PDMS sights due to high temperature facilitated chains cleavage[28,126]. The outcome of these reactions is the formation of Si-O-B bonds. Apparently, the formation of this bond in the presence of hydroxyl end groups has a low energy barrier and could happen even at room temperature (RT) based on a few reports[29,30,43]. However,

in a second scenario, these bonds cannot be formed at RT without Si-O-Si bonds cleavage first due to the absence of available condensation sights. Surprisingly, in most of the studies, condensation at RT has never been considered a reaction condition.

We reacted PDMS 25 with BA at RT with just mechanical stirring. After two hours of stirring in an open beaker, gel formation started to be observed. Once the magnetic bar could no longer rotate, the stirring stopped, and the gel rested in ambient humidity for a few hours. After that, the FTIR spectrum of the resulted gel (B25RT) was collected and analyzed.

Complete disappearance of bounded -OH band (3281 cm^{-1}) was discovered, which is very distinctive in PDMS precursors due to the high concentration of silanol groups. Also, the appearance of new bands in the B-O trigonal asymmetric stretch region (1400-1300 cm^{-1})[181] was noticed (Figure 6.1, a). A new strong peak around 1334 cm^{-1} is a B-O asymmetric stretching band which serves in the literature of PBS as an indicator of boron attachment to siloxane chain through Si-O-B covalent bond [28,126,182].

FTIR is extremely useful in detecting the presence of different boron species (trigonal and tetragonal) due to the high sensitivity of the B-O band in IR. It was shown that tetrahedral BA species have different B-O vibrational bands (asymmetric stretching in the range 1050-850 cm^{-1} and symmetric in the range 700-850 cm^{-1}) from a trigonal (asymmetric stretching in the range 1450-1300 cm^{-1} and symmetric in the range 1050-950 cm^{-1}) and this difference is IR visible[181]. None of the tetrahedral B-O bands are present in B25, whereas trigonal B-O is well pronounced (Figure 6.1, a), which rules out the possibility of the presence of dative bonds of any kind.

Boric acid in a free state possesses C_{3h} symmetry which gives only one strong peak in the B-O asymmetric stretching zone[181]. However, if a BA proton is substituted with a heavy atom, then the symmetry is lowered to C_{2v} (Figure 6.1, c). This reduction in symmetry leads to the double generation of the B-O asymmetric stretching band on an FTIR spectrum. Substitution of two protons keeps the symmetry of this vibration but generates vibration of slightly different energies[181]. Substitution of all three phonons by one type of atom brings original symmetry, although a frequency shift is expected. In the case of PBS, the general symmetry is broken due to the long flexible siloxane chains, although it is close to C_{3h} in the nearest proximity to the boron centers. Broadening and some splitting of the FTIR

asymmetric stretching are expected owing to the variety of siloxane conformations in PBS. To analyze the peaks in the trigonal B-O asymmetric stretching range, the FTIR spectra were deconvoluted using Gauss function fitting (figure 6.1b). The two low-intensity peaks at 1404 and 1414 cm^{-1} originate from the siloxane vibrations and are present in the spectrum of PDMS precursors (green line in Figure 6.1b). In contrast, the broad peak at ~1320-1380cm^{-1} only appeared in the PBS spectra and was assigned to trigonal B-O asymmetric stretching modes in good agreement with the literature [181]. Fitting allowed resolving three components a broad one centered at 1363 cm^{-1} and two relatively sharp peaks: 1331 and 1348 cm^{-1}. According to the literature [126,128,130], the latter is associated with the B-O-Si bond stretching and confirms the bond formation between PDMS and BA. The origin of the broad peak at 1368cm^{-1} is more questionable. Apart from the main condensation reaction between silanol groups and BA, a second condensation can occur between BA molecules with the formation of B-O-B bridges or even boronic acid anhydrides (boroxines).[28,126,128] In some references[28,126], 1368 cm^{-1} band was assigned to B-O-B bond stretching, for example, in boroxines. At the same time, the peak is located within the B-O-Si bond range as well, and the increased FWHM can be related to the siloxane conformations as discussed above. The FTIR analysis alone does not allow for confirmation nor to negate the formation of the B-O-B bond, which will be discussed in complex with other methods.

Quadrupolar line shape fitting of solid state ^{11}B NMR data helped to reveal details on the boron coordination environments and boron species present and in B25. Analysis of boron NMR revealed the presence of BA anhydride in BA precursor (BO_3 ring in Figure 6.2). However, we cannot say for sure if they are present in B25 or not. The width of the peak does not allow resolving distinct features. But based on the peak position, we can say for sure that no four-coordinate boron species are present in the B25 sample or BA, which supports the previous finding from the FTIR analysis.

The formation of boronic anhydrides requires an excess concentration of BA (3 times higher than the stoichiometric concentration for boroxines). However, considering that all hydroxyl moieties (Si-OH and B-OH) disappeared as a result of condensation and that stoichiometric concentrations were chosen, we can conclude that boroxines or any other boron anhydrides are highly unlikely to be present in B25.

For comparison, we synthesized another sample (B25) with heating in toluene in a Dean-Stark apparatus for 24 hours at 140 ºC. Surprisingly, spectra of B25 and B25RT matched one to one. This fact suggests that condensation proceeds along the same path, both at room temperature and when water boils away with its intake from the system. The formation of Si-O-B bonds proceeds rather through cleavage of B-O bonds and consequent attachment of boron instead of hydrogen in the silanol group due to the dynamic nature of B-O bond[153]. Synthesis of PBS from trimethyl borate supports this hypothesis since methanol is released during condensation due to the high stability of the C-O bond[29]. However, the high energy of the B-O bond (537.6 kJ $mol^{-1,}$ which is even higher than Si-O bond energy 422 kJ mol^{-1})[183–185] implies that the formation of Si-O-B probably does not involve actual covalent B-O bond breakage but rather ligand substitution instead. This is aligned with the fact that ligand substitution is observed in boronic esters. They were shown to participate in associative exchange either through transesterification (in the presence of free diols) or metathesis, which certainly occurs without any bond cleavage[44].

To confirm that the formation of gel is directly related to the appearance of Si-O-B bands on the FTIR spectrum, we poured the same concentration of BA powder directly onto PDMS oil in the FTIR sample holder without mixing and let it rest for 15 minutes (sample B25RT2). The appearance of the small peak at 1334 cm^{-1} was noticed (Figure 6.1, a), together with the appearance of small cloudy zones of higher viscosity around the BA clusters. A small peak was noticed at 1200 cm^{-1} peak in B25RT2, which is the -OH vibration band of B-OH[43,181]. This peak completely disappears in the fully reacted sample (B25 or B25RT), suggesting that B-OH species are not present in PBS.

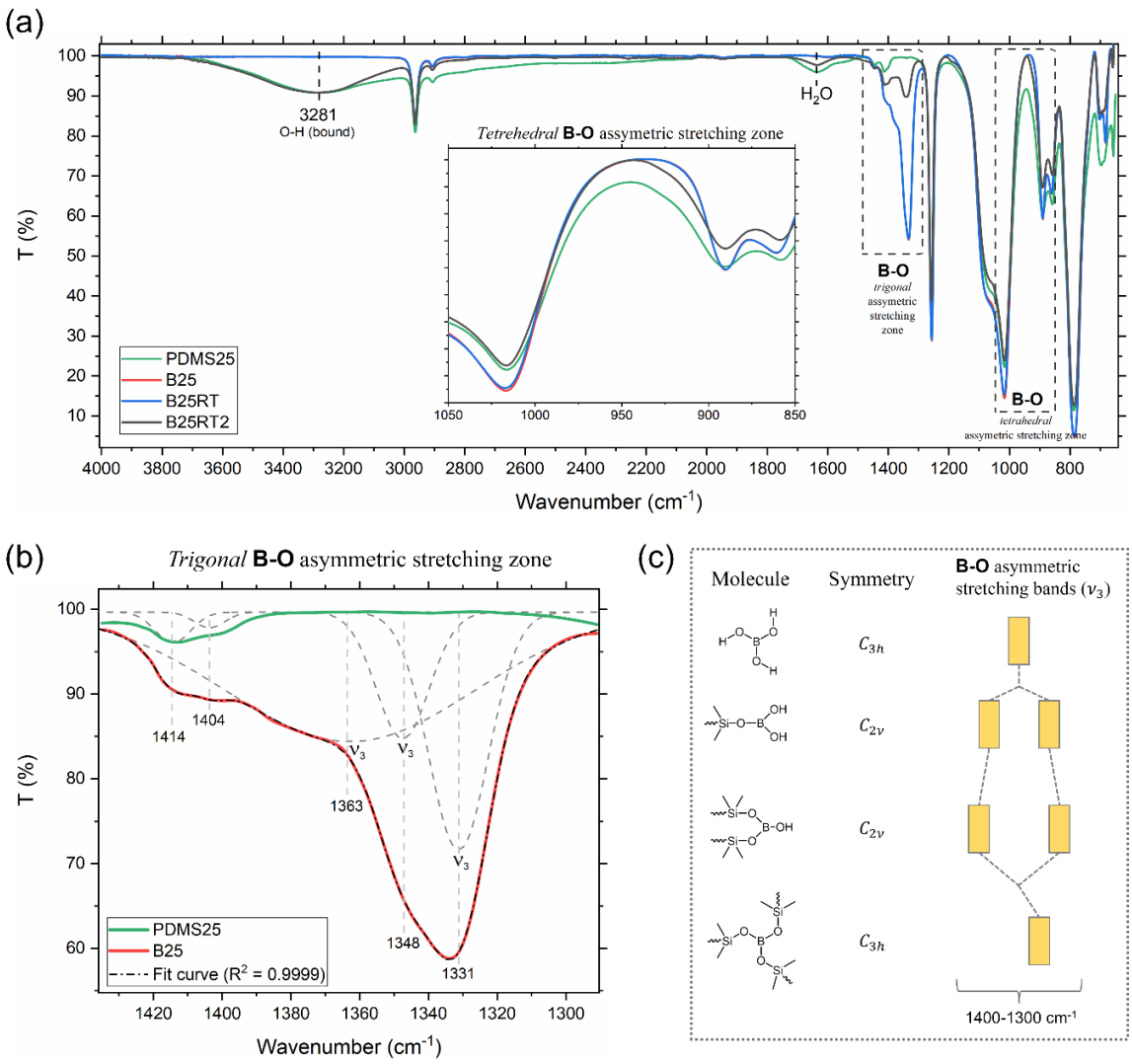

Figure 6.1 (**a**) FTIR spectra of PBS samples synthesized at room temperature (B25RT), with heating in toluene in a Dean-Stark apparatus (B25), 15 min after addition of boric acid to PDMS25 without any stirring (B25RT2), and precursor (PDMS25). The inset is the zoomed-in plot in the tetrahedral B-O asymmetric stretching zone. (**b**) Gauss function fit of B25 spectra in a trigonal B-O asymmetric stretching zone with $R^2 = 0.9999$. (**c**) Splitting of asymmetric B-O stretching band based on a symmetry of boron compound (free BA, one, two, and three protons substituted BA molecules).

The result of the condensation reaction between hydroxyl groups is the formation of water. Since it was found that condensation in PBS can take place without severe dehydration, we assume that some amount of water should still be present in bulk. We tried to manipulate the kinetics of condensation reaction based on the assumption that the addition of a water

absorber could significantly accelerate formation of gel. Surprisingly, addition of water absorber (Na_2SO_4 salt) did not noticeably accelerate a gel formation in comparison to the sample without it during reaction at RT. The results from the literature[128] and our own research demonstrated that even heating at a high temperature does not significantly accelerate a gel formation.

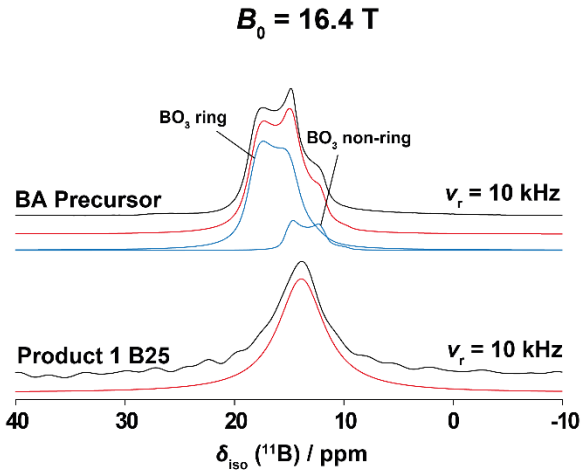

Figure 6.2 1D spectrum of boric acid alone (BA precursor) and B25 acquired at 16.4 T with 10 kHz spinning. The line shape is fit using the quadrupole parameters (CQ = 2300, 2400 kHz, η = 0.2) that were obtained from solid-state ^{11}B-NMR, with red curves being a sum of the fits. BO_3 ring corresponds to the three-coordinate boroxine species and the BO_3 non-ring to the other three-coordinate boron species. Chemical shifts δ_{iso} = 16.0 and 19.3 ppm (BA), 13.9 ppm (B25).

Another approach how to affect gel formation was tried by the addition of pyridine to a mixture of BA and PDMS25. Only partial formation of gel was observed after 4 hours of intensive stirring due to interference from pyridine molecules. After a few days, phase separation of BA powder and PDMS oil was observed without any gel present. In a study by Gridina et al.[30], they suggested that the addition of pyridine suppresses the formation of gel in PBS since nitrogen is a more powerful electron donor than oxygen. Hence, boron favors the formation of dative bonds with nitrogen over siloxane's oxygen. However, their explanation was based on the belief that dative bonding between boron and oxygen of siloxane backbone is the only type of dynamic bond present in PBS. The addition of Lewis bases (including nitrogen-bearing molecules like pyridine) to boronic acid is known to facilitate the formation of boroxines[156,158,186] and boronic esters[187] (in the presence of diols)

as well as accelerate their transesterification rates[180]. In our case, nitrogen from pyridine molecules possibly datively bond to boron atoms converting it to a 4-coordinate anionic state, which somehow disrupts dynamic exchange. For now, we can only say that presence of nitrogen does suppress the formation of gel, but the reason will be elaborated on further. After that, we tried to assess the effect of BA concentration on the kinetics of reaction at RT. At 30% of the stoichiometric saturation concentration, gelation was not observed at all. This fact is aligned with the knowledge that for a trifunctional crosslinker (and we assume that BA is) gelation threshold is 50% of a stoichiometric saturation concentration[150,188]. At an excessive 300% concentration, the gel is completely formed after 2 hours of stirring, whereas at 100% of stoichiometric saturation, gelation started to be observed in 4 hours only. This could probably be explained by the rich availability of B-O functional sights at excessive concentrations. Notably, the FTIR spectra of samples at 100% and 300% completely match one to one.

To understand how the absence or presence of water affects the properties of PBS, we conducted a hydrolysis study on a B25 sample which was synthesized through intensive dehydration in a Dean-Stark apparatus in toluene for 24 hours. The resulted gel was clear at first, but after equilibration with a laboratory moist, some amounts of white solid residues appeared. They are most probably BA powder released due to partial hydrolysis of B-O bonds based on reports of the others[28]. However, after a few filtering cycles, no visible amount of BA was detected.

After hydrolysis of B25 in THF/water (10:1) solvent and consequent solvent evaporation, it became much softer and stretchy; a small but wide peak around 3300 cm^{-1} appeared back with B-O asymmetric stretching bands remaining almost unchanged (Figure 6.3). Out of curiosity, we added water directly to a B25 sample, rested it on an FTIR sample holder, and gave it 20 minutes to interact. Same small -OH stretching band appeared too (coming probably from the water itself) and had no significant effect on the Si-O-B band. Long exposure of B25 to water (either by placing the sample in water or adding an excessive amount of water to THF solution) results in a complete loss of gel-like consistence with phase separation of BA from the oil phase. The explanation will be given further in light of the proposed mechanisms.

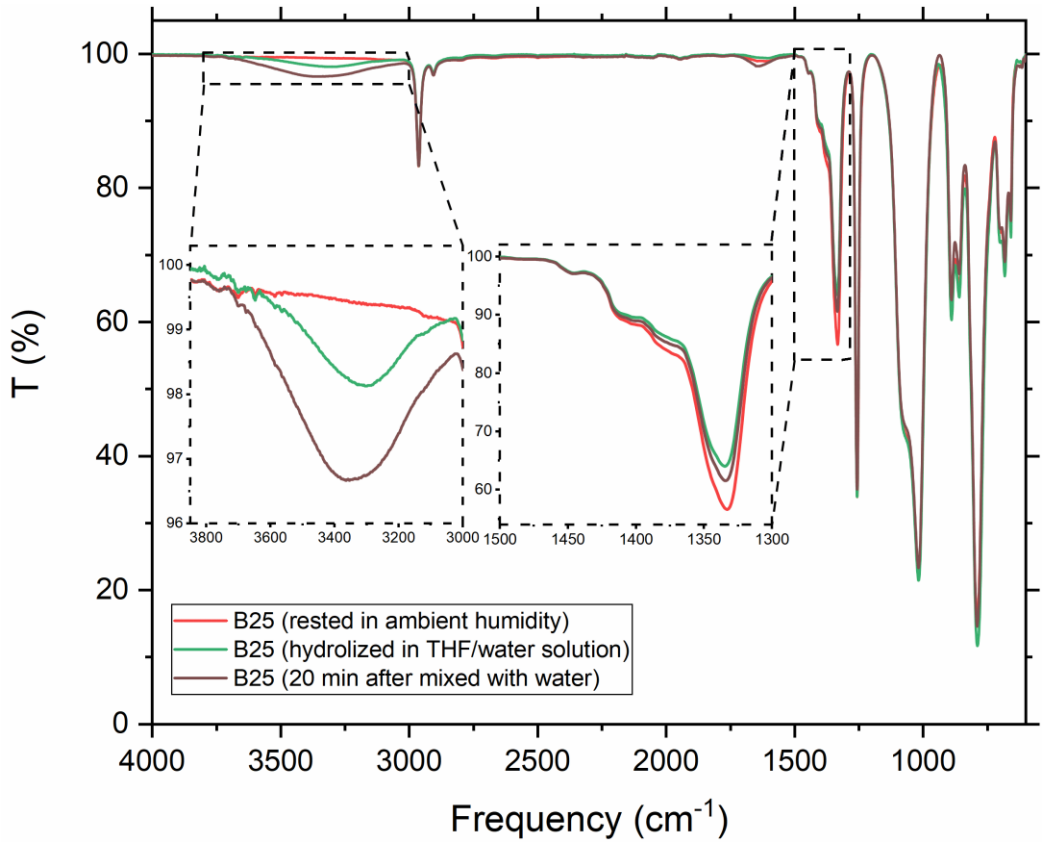

Figure 6.3 FTIR spectra of three PBS samples: B25 equilibrated with the laboratory moist, B25 hydrolyzed in a 10:1 solution of THF/H_2O, and B25 directly mixed with water after 20 minutes.

The fact that dynamic bonds break down in THF was further analyzed using a MALDI-ToF mass spectrometer, which can give the exact molecular weight of individual chains. First, a droplet of the prepared dilute solutions of PBSs in THF was cast on the sample holder right after a droplet of matrix solution (1:1 THF DI water), then a droplet of the ionizing agent in the same solvent was deposited on top. After that, the solvents are supposed to evaporate slowly, allowing the sample and matrix to co-crystalize. We need to point out that during the co-crystallization phase, PBS was exposed to water (for around 10 minutes) which may cause hydrolysis and loss of dynamic bonds.

Obtained MS spectra of B25 matched PDMS precursors spectra without a noticeable change in distribution (Figure 6.4). This points out on hydrolysis of boron crosslinks which happens upon contact with water or even by THF molecules themselves. This serves as solid proof of the ease of Si-O-B bond breakage. However, further investigation needs to be done.

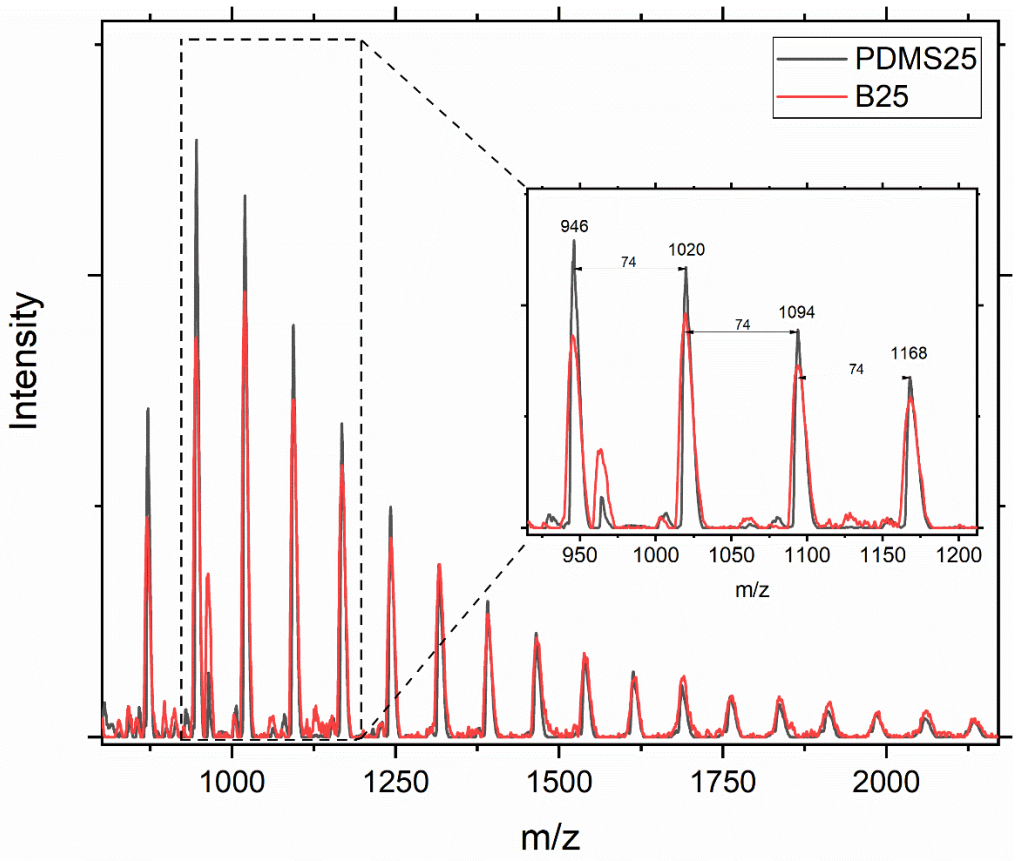

Figure 6.4 MALDI-ToF-MS spectra of the precursor (PDMS 25) versus PBS product (B25). Peaks coincide due to hydrolysis of B25 upon contact with water during the co-crystallization stage.

The ability and efficiency of breaking dynamic crosslinks by different solvent molecules was analyzed next (Table 6.1). Six solvents of different nature were chosen for the study (IPA, hexane, chloroform, acetone, DMF, and DI water). IPA was found to be the best solvent since it dissolved PBS the fastest with no sign of BA residues, followed by chloroform and hexane. Some amount of BA powder was seen at the bottom of chloroform solution, whereas hexane solution had no visible amount of residues. Acetone goes next, but it took much longer for it to dissolve PBS (without any visible residues after). Water demonstrated an interesting effect on PBS; at first, it did not show any effect on PBS, but after it was left for a few days, it completely hydrolyzed PBS (emulsion of silicone oil alone in water, spherical droplets easily coalescent or breakdown if shaken). DMF, surprisingly, demonstrated no effect on the PBS even after a week.

Table 6.1 Dissolution study of B25 in various solvents.

Solvent	Molecule structure	Polarity index	Relative time until B25 is fully dissolved	Presence of BA residues
IPA		3.9	5 min	Very little
Chloroform	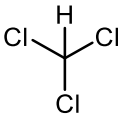	4.1	25 min	Yes
Hexane		0.1	30 min	No
Acetone		5.1	2 hours	No
DMF	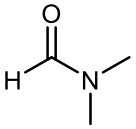	6.4	No effect at all even after 48 hours	-
DI water	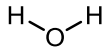	10.2	No effect for the first 12 hours; completely hydrolyzed in 48 hours	No

The efficiency of IPA as a solvent can be explained by the fact that being moderately polar, it is able to diffuse into PBS bulk, partially hydrolyzing Si-O-B bonds (with a release of some BA) and partially disrupting exchange by competing with silanol groups. Chloroform, being more polar, seems to enter the bulk at a slower rate and subsequently hydrolyze boron crosslinks to a greater extent. Since no residues are seen in hexane solution, BA probably remains attached to PDMS molecules (due to the non-polar nature of hexane and polarity of BA, the precipitation of a solid phase would be easily visible). This explains why after solvent evaporation and filtration PBS regains its viscoelastic properties completely. Acetone being more polar than IPA and chloroform takes the longest time to penetrate through hydrophobic PDMS surface. It is difficult to say whether it hydrolyzed boron crosslinks or not and to which extent since they are not visible but released BA theoretically could be dissolved in acetone. Most probably, DMF did not show any effect due to the high polarity index. On the contrary, despite water molecules being even more polar, it managed to penetrate inside and hydrolyze all Si-O-B bonds back into hydroxy terminated PDMS and BA. The smaller size of water molecules makes them more mobile, which gives them

benefits in the long run; hence, in a few days, they managed to reach the bulk hydrolyzing PBS completely.

6.3.2 Effect of the number of B-O bearing functionalities

To probe the effect of B-O functionality, we reacted three hydroxy terminated PDMS with stoichiometric concentrations of phenylboronic acid, which is bifunctional (two B-O bonds), whereas boric acid is trifunctional. All three products did not demonstrate gelation but an increase in viscosity only. After samples were filtered and dried, their apparent viscosities were measured in a shear mode with parallel plate geometry (Figure 6.5). All of them demonstrated Newtonian behavior in the measured range of shear stresses which makes it easy to compare their apparent viscosities since values are independent of shear rate. Apparent viscosities, as well as results of GPC analysis, are shown in Table 6.2. Despite the increase of apparent viscosity 4-8 times with respect to silicone oil precursors, the number average molecular weight M_N of PBSs was found to be similar to the precursor values. This fact confirms that the increase in viscosity is solely the result of dynamic crosslinking, which breaks down in THF, as well as an absence of scissoring, growth, or permanent crosslinking in PDMS chains after synthesis. However, bifunctional crosslinking results in chain extension only, which in our case explains the absence of gelation.

The viscosity of P25 increased by a factor of 4, which, according to Barry calculation method[189] corresponds to an increase in MW by the factor of 8; hence, for P65 and P750 16 times and 14 times, respectively. Similar results were published by Gridina et al.[30] where they reacted PBA and many other boron compounds with hydroxy-terminated PDMS. In their case, the intrinsic viscosity of PBS from PBA has grown 5 times which corresponds to ten times increase in MW. They suggested that PBA and other bifunctional boron compounds (n-functional was defined by the number of B-O or B-Cl bonds per molecule) provide linear chain extensions only. On the contrary, PBS synthesized from trifunctional boron compounds reached the rubbery state, which suggests that trifunctional crosslinking occurs directly through the B-O bond. Bloomfield, in his work[29], suggested that gelation of PBS is the result of trifunctional dynamic crosslinking through the formation of covalent

Si-O-B bonds, which participate in dynamic exchange with each other.

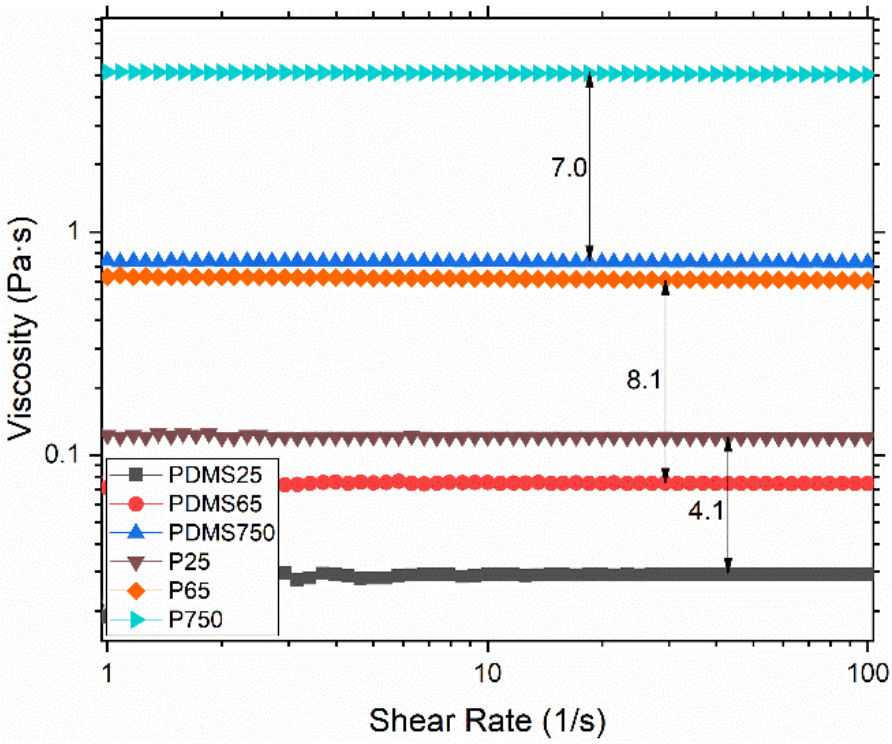

Figure 6.5 Apparent viscosities as a function of shear rate. In the selected range of rates, all PBA-based PBS demonstrated Newtonian flow. Numbers indicate an n-times increase in apparent viscosities with respect to the silicone oil precursor.

Table 6.2 Viscosities obtained in Newtonian region. Number average molecular weight of precursors and synthesized products.

	Apparent viscosities, $Pa \cdot s$		M_n, kg mol^{-1}	
Sample	PDMS	P	PDMS	P
25	0.029	0.121	0.60	0.56
65	0.076	0.618	1.25	1.14
750	0.74	5.14	14.49	18.22

FTIR analysis of synthesized samples demonstrated the disappearance of strong bounded O-H stretching peak around 3300 cm^{-1} and the appearance of new intensive peaks in the zone of trigonal asymmetric B-O stretching (1400-1300 cm^{-1}), same as in B25 (Figure 6.6, a). However, the Gauss fitting of peaks in this zone revealed two additional vibrational bands (Figure 6.6, b) at 1316 and 1297 cm^{-1}. The 1315 cm^{-1} band is missing in the spectra

of the PBA precursor; however, we assigned it to the organic vibrations of the phenyl ring in good agreement with the literature[190]. The absence of the peak in the spectrum of the PBA may be due to its crystalline form. The 1297 cm^{-1} band originates from in-plane C-H deformations of the phenyl ring, which is also observed on the PBA spectrum. The same three B-O asymmetric stretching bands (ν_3) from B25 are observed in P25. These bands originate from the Si-O-B bonds, which supports the hypothesis of bifunctional chain extension through Si-O-B bonds in P25. These band intensities change accordingly to the concentration of Si-O-B bands in the same fashion as was shown in Chapter 5, with approximately the same ratios between them (Figure 6.6, a). The fact that the broad ν_3 band ~1368 cm^{-1} is present in P25 implies that this band is not an indicator of boroxines/other anhydrides stretching due to the impossibility of their formation together with condensation with silanol groups in P25 (either one since there are only two available hydroxyl groups in PBA).

Additionally, these bands have not been present on the FTIR spectrum from another study[42], where they modified chain ends of siloxane with phenylboronic acid through an ethylene bridge attached to the phenyl ring. Therefore, these peaks are inherent to the case when a boron atom is attached to a silicone atom through oxygen.

The rest of the new peaks appeared with small intensities and at the same positions as in PBA, which suggests that some amount of unreacted PBA fraction remained in bulk. Two tiny in-plane B-OH bending band peaks were also seen in P25, which come from attached (1140 cm^{-1}) and free PBA molecules (1184 cm^{-1}).

None of the tetragonal B-O asymmetric stretching bands (1050-850 cm^{-1}) are present on the P25 spectrum, which was also confirmed using solid-state ^{11}B-NMR (Figure 6.6, c). Only a single peak of trigonal boron state was observed; however, P25 exhibits a pronounced ^{11}B chemical shift difference compared to B25. This is probably due to the B speciation in this product being coordinated to phenolic moieties or similar C-containing/organic species.

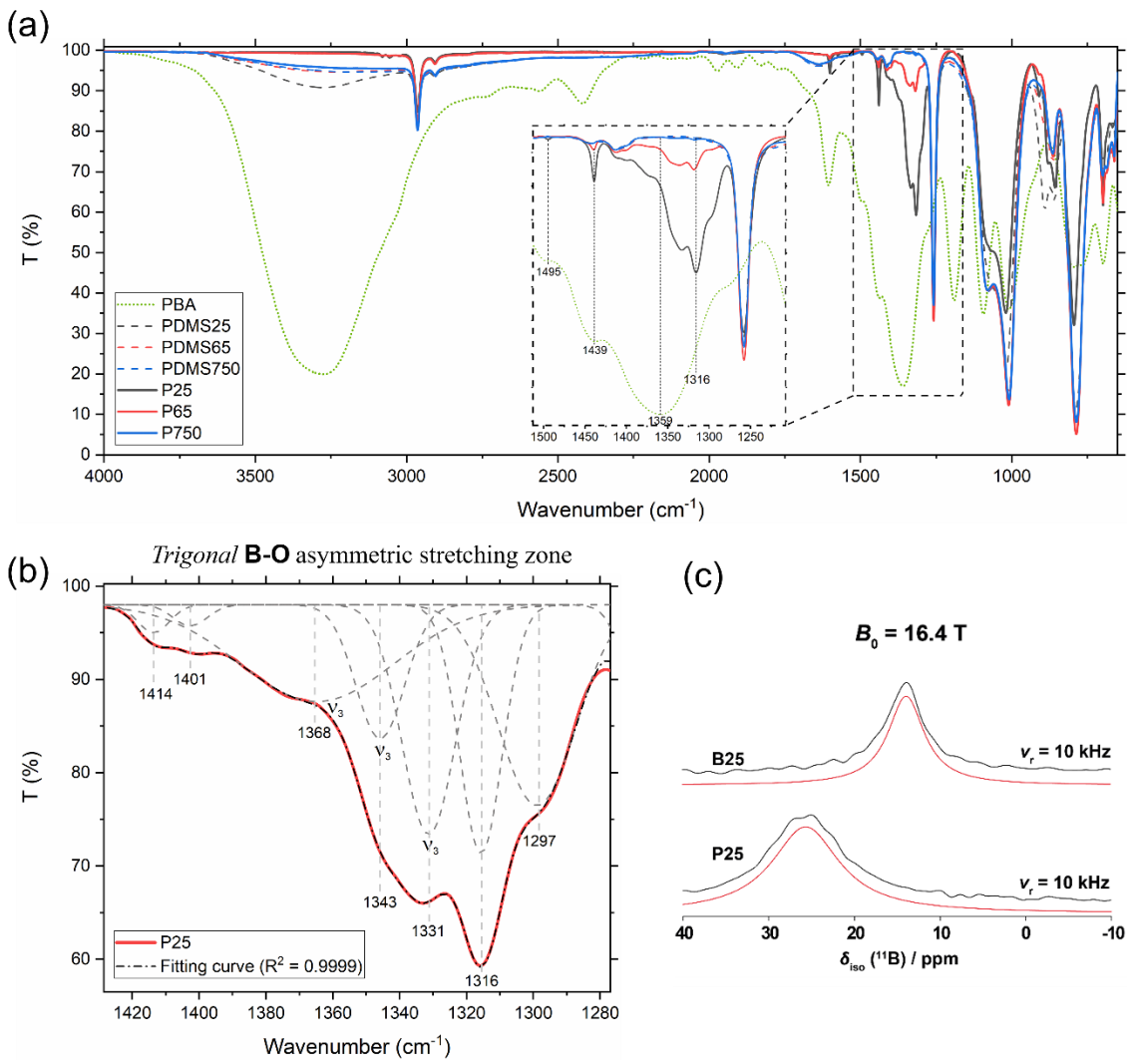

Figure 6.6 (**a**) FTIR spectra of PBS samples synthesized with bifunctional phenylboronic acid (PBA) from different MW PDMS. The inset is the zoomed-in plot in the 1200-1500 cm^{-1} range. (**b**) Gauss function fit of P25 spectra in a trigonal B-O asymmetric stretching zone with $R^2 = 0.9999$. (**c**) 1D spectrum of P25 versus B25 acquired at 16.4 T with 10 kHz spinning (black curve). The line shape is fit using the quadrupole parameters (CQ = 2300, 2400 kHz, η = 0.2) that were obtained from solid-state ^{11}B-NMR (red curve). Chemical shifts δ_{iso} = 16.0 and 26.0 ppm (P25), 13.9 ppm (B25).

6.3.3 Discussion on the mechanism of dynamic crosslinking in PBS

Hydrogen bonding

One of the first proposed mechanisms which is accountable for a dynamic crosslinking in

PBS was hydrogen bonding between hydroxyl groups of BA[127]. Later it was found that dimeric hydrogen bonding between two boronic acids is the preferred way of interaction over monomeric bonding due to sterical advantages[45]. However, the presence and active contribution of H-bonding to dynamic properties were debated in the literature of PBS.

We discovered that gelation in PBS is the result of a condensation reaction between silanol groups and boric acid, which leads to the complete disappearance of both Si-OH and B-OH vibration bands on FTIR. Besides, if hydrogen-bonded dimers would even exist in PBS, they could only provide linear chain extension, which would not result in gelation and unique rubber elasticity at higher deformation rates. Furthermore, a detailed analysis of viscoelastic properties of PBS by Bloomfield[29] in comparison to permanently crosslinked silicone rubber with the same crosslinking density showed that all dynamic crosslinks in PBS are of covalent nature. All facts together allow us to rule out hydrogen bonding as a possible explanation for the mechanism of dynamic crosslinking in PBS.

Dative bonding

Boric acid is a mild Lewis acid and, therefore, is able to change its hybridization from sp^2 to sp^3 in the presence of Lewis base. Upon this change, BA undergoes the transition from trigonal to tetragonal state where it can form a fourth bond (dative) with the atom donating electrons (such as oxygen or nitrogen)[44,45,152]. The ability of boron forming dative bonds with oxygen was proposed as another explanation of dynamic crosslinking in PBS alongside H-bonding. It was believed that the dative bonding takes place between a boron atom and oxygen of siloxane chains only[30,31,37,43], until it was found that boron can form dative bonds with the oxygen of another BA molecule[42]. In addition, dative bonds are identical to covalent in terms of length and strength, which makes it difficult to distinguish between them[191]. Hence, sometimes they are called “coordinate covalent”.

Based on the results of this project, we can state with confidence that static dative bonds are not present in our PBS samples because of the absence of 4-coordinate boron species on ^{11}B-NMR in addition to tetragonal B-O bands on FTIR. Therefore, dative bonding cannot be used as an explanation of dynamic crosslinking in PBS, and other mechanisms should be considered.

Boroxines and boron anhydrides

During pyrolysis, BA undergoes three-step dehydration. First, around 104 to 140 ºC BA converts into metaboric acid (HBO_2)[184], heating above 180 ºC leads to further dehydration with subsequent formation of pyroboric acid ($H_2B_4O_7$), and further heating to higher temperatures leads to the formation of boron trioxide (B_2O_3)[192]. Boroxine is technically a metaboric acid when all three hydroxyl groups are substituted with another atom or group. Hence, it was believed that they could be present in PBS upon dehydration synthesis. According to Liu et al.[28], boroxines can form in PBS when the sample is significantly dehydrated, but once the sample is exposed to air moisture, these boroxines hydrolyze into BA, and thus excessive powder is seen after some time in the air. We observed separation of BA when dried PBS was equilibrated with the laboratory moisture; however, the proposed B-O-B IR band did not change in intensity in our case. Also, the presence of boroxines in PBS was correlated with the appearance of an additional time scale on the loss modulus and the absence of a clear rubbery plateau[28]. But in our case, these features were not found (Figure 5.7), which indicates the absence of boroxine complexes in the air-rested samples. Besides, the absence of free hydroxyl moieties at a stoichiometric concentration of BA implies the unlikeness of the presence of boroxines or other anhydrides. Therefore, even if some amount of boroxines could be present, they play a minor role in dynamic crosslinking.

Dynamic covalent bonding

The dynamic nature of the covalent B-O bond is a well-established fact that allows efficiently unitizing boronic acids as a building block of supramolecular assemblies and polymer[44,45,152,153]. Boronic esters and boroxines are the most studied B-O-containing compounds which could participate in dynamic exchange through both dissociative mechanisms (upon hydrolysis/dehydration[44]) and associative (transesterification[44,157,158] or even metathesis[154,157,159]). It was found that for boronic esters associative exchange mechanism dominates in dry conditions whereas dissociative in humid[155].

A similar concept was recently proposed by Bloomfield[29] as a possible explanation for dynamic properties in PBS. He suggested that BA acts as a trifunctional crosslinker upon reaction with PDMS, where newly formed Si-O-B bonds participate in an associative

exchange with each other through ligand exchange of oxygen atoms with neighboring silanol moieties. This mechanism resembles transesterification exchange in boronic esters, which takes place in the presence of an excessive amount of free diols[44]. Therefore, it would be correct to call the mechanism proposed by Bloomfield a dynamic covalent bonding. Based on the results from this chapter, this mechanism ticks all the boxes as an explanation for the experimental data and observations. We demonstrated the absence of other types of dynamic bonds (hydrogen ad dative) as well as a minor role of boron anhydrides if they are present. Ease of Si-O-B formation through condensation at room temperature and almost instant hydrolysis upon contact with water point out a low energy barrier of Si-O-B formation/breakage. The high energy of the B-O bond hints at a ligand exchange rather than the actual bond breakage. The efficiency of alcohol, carboxylic acid, and water molecules in disruption of dynamic bonds in PBS suggests that hydroxyl-bearing moieties interfere with the dynamic exchange by competing with silanol groups. The absence of gelation at concentration < 50% from stoichiometric saturation for trifunctional crosslinker paired with the rheological analysis of low-MW PBS gels in chapter 5 (perfect fit to Maxwell viscoelastic model) implies that all dynamic crosslinks are of the same nature and are trifunctional. The fact that they are n-functional (where n represents the number of B-O groups in a boron compound) or trifunctional in the case of boric acid was supported by the synthesis of PBS from bifunctional PBA molecules, which demonstrated linear chain extension without signs of gelation. In a recent work by Chen and co-workers[193] they suggested that self-healing of their PBS occurs through the associative exchange of oxygen atoms in neighboring Si-O-B bonds. However, no description or reason was given why they suspect this self-healing mechanism over others.

Considering all facts together, we believe that the initial formation of Si-O-B bonds occurs through a dissociative mechanism, which requires shifting condensation reaction equilibria towards product formation (hence, non-instant in the absence of aggressive dehydration). Once a necessary number of Si-O-B bonds are formed, they participate in an associative bonds exchange with each other through oxygen ligand exchange with hydroxyl bearing moieties (silanol, alcohol, water, etc.). However, the kinetics of Si-O-B bonds associative exchange together with the possibility for metathesis (in the absence of hydroxyl exchangers), needs to be investigated further.

6.4 Chapter summary

The gelation of PBS results from condensation of the majority of silanol groups with hydroxyl groups of the boronic compound with subsequent formation of n-functional (-Si-O)$_n$-B bridges (where n is defined by the number of B-O functionalities of boron compound). This reaction proceeds through ligand substitution of oxygen atom in B-O sights of boron compound (oxygen of silanol group exchanges with the oxygen of boron compound), which has a low energy barrier and happens even at RT.

Kinetics of condensation is hardly affected by dehydration (through heating in a Dean-Stark apparatus or addition of Na_2SO_4 as a water absorber); however, excessive concentration of BA was found to accelerate the formation of the gel. On the contrary, the addition of nitrogen-bearing molecules like pyridine was shown to suppress the gelation of PBS.

Hydrolysis of PBS results in breakage of the Si-O-B bonds due to the boron preference of water molecules over silanol groups, disrupting dynamic exchange. Hydrolysis is instant in polar PBS solution upon addition of water but relatively slow when water is in direct contact with PBS bulk. In the first case, water has direct access to boron sights whereas in the second hydrophobic PDMS chains repeal water molecules until they diffuse in the bulk. A small amount of water leads to only partial hydrolysis of the boron compound with its subsequent phase separation (-Si-O-B- + H_2O → -Si-OH + HO-B-). In contrast, a large amount of water can lead to complete hydrolysis of all Si-O-B functionalities with a loss of gel-like consistency. Alcohols moderately polar and non-polar solvents have been found to be better PBS solvents than ketones (IPA > chloroform ≈ hexane > acetone) with no effect from amides. The effectiveness of solvent is an interplay between their polarity (if too polar, PDMS repeals the solvent molecules) and the type of oxygen-bearing group (-OH is the best due to higher reactivity towards B-O oxygen exchange).

Based on the analysis of rheology from Chapter 5 and research, all dynamic crosslinks are of the same nature; they are all temporary (with the same lifetime), they all participate in the exchange and are of covalent nature. No hydrogen bonds (absence of Si-OH and B-OH bands), dative bonds (absence of 4-coordinated boron species), or anhydride complexes

(like boroxines) were found in PBS. The recent explanation of dynamic crosslinking given by Bloomfield[29] suits our results the best, which suggests the transient nature of the boron crosslinks to be due to oxygen ligand exchange reaction between -OH bearing molecules (like free silanol groups, water, alcohol, etc.) and covalently attached boron trifunctional crosslinks through B-O functionalities. This mechanism also resembles well-established dynamic covalent bonding, which is observed in boronic esters; the only difference is that in our case, silanol groups are involved in crosslinking and exchange instead of diols. However, due to the complexity of the matter, further research is needed to confirm this mechanism and explore the possibility of the metathesis exchange. As well as examine the possibility of tuning the kinetics of the exchange reaction by manipulating the content of molecules containing free hydroxyls.

The discovery of dynamic covalent bonding as a preferred mechanism of gelation and exchange in PBS provides vast opportunities for developing new siloxane-boron smart materials based on a choice of hydroxy functionality of boron compound, type of boron crosslinker, the concentration of silanol moieties, etc. Secondly, found low energetic barrier of gelation through dynamic covalent substitution at room temperature allows to reduce cost and simplified production of PBS due to a heat-free synthesis routine (versus conventionally used high-temperature synthesis). Thirdly, discovered mechanism favors better prediction of mechanical properties based on supramolecular structure and aids the development of more precise models for computer simulation experiments. Last but not the least, a better understanding of the dynamic crosslinking mechanism expands the fundamental knowledge in supramolecular chemistry. That brings up the potential for the future development of novel materials and technologies.

Chapter 7

Conclusions and Recommendations

Chapter 7 concludes the finding of three results chapters, including (1) in situ observation of jamming front propagation during low-velocity impact in polypropylene glycol/fumed silica STF and how it contributes to impact dissipation; (2) correlations between the molecular weight of precursor and mechanical properties in polyborosiloxane (PBS) with special attention to impact absorption; (3) Mechanism of multifunctional dynamic crosslinking in PBS. The potential of STF and SSG to replace conventional protective materials is being discussed with ideas about their composites as bulk protection.

7.1 Conclusions

7.1.1 Impact absorption in fumed silica STF

Many studies have been devoted to the mechanism of thickening in the most famous representative of STF - a dense suspension of cornstarch in water. However, this STF has not found wide application in the field of protection due to the instability of the suspension and rapid biodegradation of cornstarch particles. In search of alternatives, fumed silica suspension in polar low molecular weight polymers has attracted the attention of researchers as a better candidate without the aforementioned shortcomings.

Here, we explored its impact absorption potential in bulk and the mechanism behind it. Oscillatory rheology revealed the presence of discontinued shear thickening (DST) starting from volume fraction $\phi \cong 7.2\%$, which is the prerequisite for shear jamming (SJ). For the first time, using novel optical in situ speed recording of impact, it was found that jamming can be triggered at as low as $\phi > 7.2\%$. Image correlation analysis of the flow field during impact has shown that the jamming front grows 3-5 times faster than the speed of the impactor, which confirms that its prorogation is triggered by shear, not by densification (Figure 7.1).

To demonstrate how jamming can be used for the benefit of bulk impact protection, we paired analysis of the flow field with the data from the accelerometer and load cell during drop weight tests. It was discovered that fumed silica jamming front forms a solid-like plug beneath the rod, which grows faster than the impactor speed and leads only to minor impact dissipation. However, once the front reaches the bottom boundary, it generates a huge normal force that opposes the impactor penetration, and that is when the main impact dissipation begins. At a higher volume fraction, the front grows faster, hence, reaching the bottom early, which creates the plug of a particular thickness (Figure 7.1, A-C). This thickness defies the efficiency of impact dissipation.

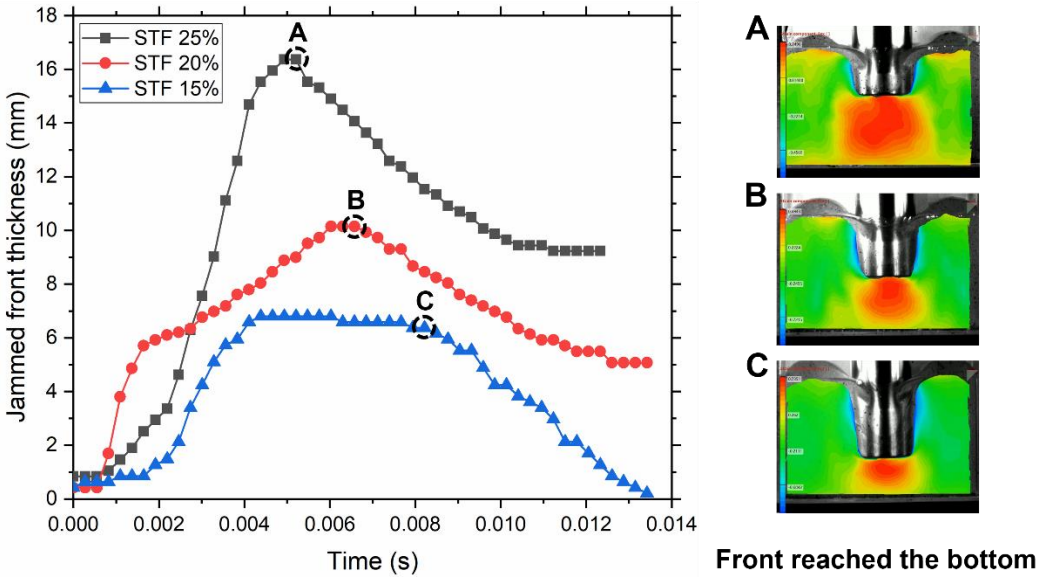

Figure 7.1 Jamming front prorogation during low-velocity impact in fumed silica/polypropylene glycol.

In this work, the importance of SJ for effective impact absorption was demonstrated. This expands the potential for using STF as bulk protection which was previously limited to fabric impregnation. In addition, the findings of this project suggest shifting the focus of researchers from studying the shear thickening alone to SJ and how it can be used to its maximum potential. The results of this study are of interest to a broad readership, including researchers who develop soft protective solutions (especially for sports applications), who study impact absorption in STF, and who work with the physics of granular suspensions.

7.1.2 Effect of MW on the impact absorption of PBS

Polyborosiloxane (PBS) has been previously successfully employed as a functional filler in protective composites due to its strong shear-stiffening properties. However, the potential of its bulk protection has been rather unexplored. In the second results chapter, we tried to evaluate low-velocity impact dissipation in PBS bulk and how the density of dynamic crosslinking contributes to it. It was discovered that the stiffening performance of PBS can be controlled by the molecular weight of PDMS precursors due to a straightforward condensation reaction between hydroxy end groups of PDMS and boric

acid. Introduced boron sights behave as dynamic crosslinks, hence, are responsible for the shear-stiffening properties. New correlations were discovered for five PBSs synthesized from hydroxy-terminated PDMS of various molecular weights. Si-O-B IR band intensities were used as a quantitative parameter of dynamic crosslinking densities. After synthesis, the molecular weight of PBSs remained almost the same, which indicates the absence of significant chain scissoring, polymerization, or cross-linking. This synthesis route allows precise controlling of mechanical properties based on the precursor's molecular weight. During the rheological analysis, it was found that crossover point modulus follows the same trend as the number of PDMS hydroxy groups and Si-O-B band intensities. PBS demonstrated a linear increase in peak forces with molecular weight during the drop weight impact test (Figure 7.2, a-b). The reason for this dependence is directly related to the number of dynamic bonds in the polymer, which “lock” in place upon impact. Their greater number in low-MW PBS (Zone 1) provides better energy dissipation (through stiffening transition and breakage of dynamic bonds) than in PBS with higher MW (Zone 3), as shown in Figure 7.2, c. Therefore, the low molecular weight of a precursor, hence, a high number of dynamic crosslinks, is a primary requirement for effective protection against low-velocity impact.

We set out to understand the mechanism of dynamic crosslinking in PBS due to the large number of contradictions found in the proposed explanations in the course of the study, with the aim of subsequently using this knowledge to improve the protective properties. Dynamic covalent bonding, well known from the research on boronic ester, is shown to be the most probable mechanism behind the unique viscoelastic properties of PBS. The closest explanation was given by Bloomfield[29] recently, which states that the dynamic nature of boron crosslinks is due to oxygen ligand exchange reaction between -OH bearing molecules (like free silanol groups, water, alcohol, etc.) and covalently attached boron trifunctional crosslinks (or tetrafunctional in case of THDB) through B-O functionalities. The mechanism of initial gelation, which is the result of condensation between silanol and boron hydroxyl groups, was found to be of the same nature as the dynamic exchange of Si-O-B covalent bonds, which makes it easy for them to form (even at room temperature) and vulnerable to break (during hydrolysis or with the addition of -OH bearing molecules).

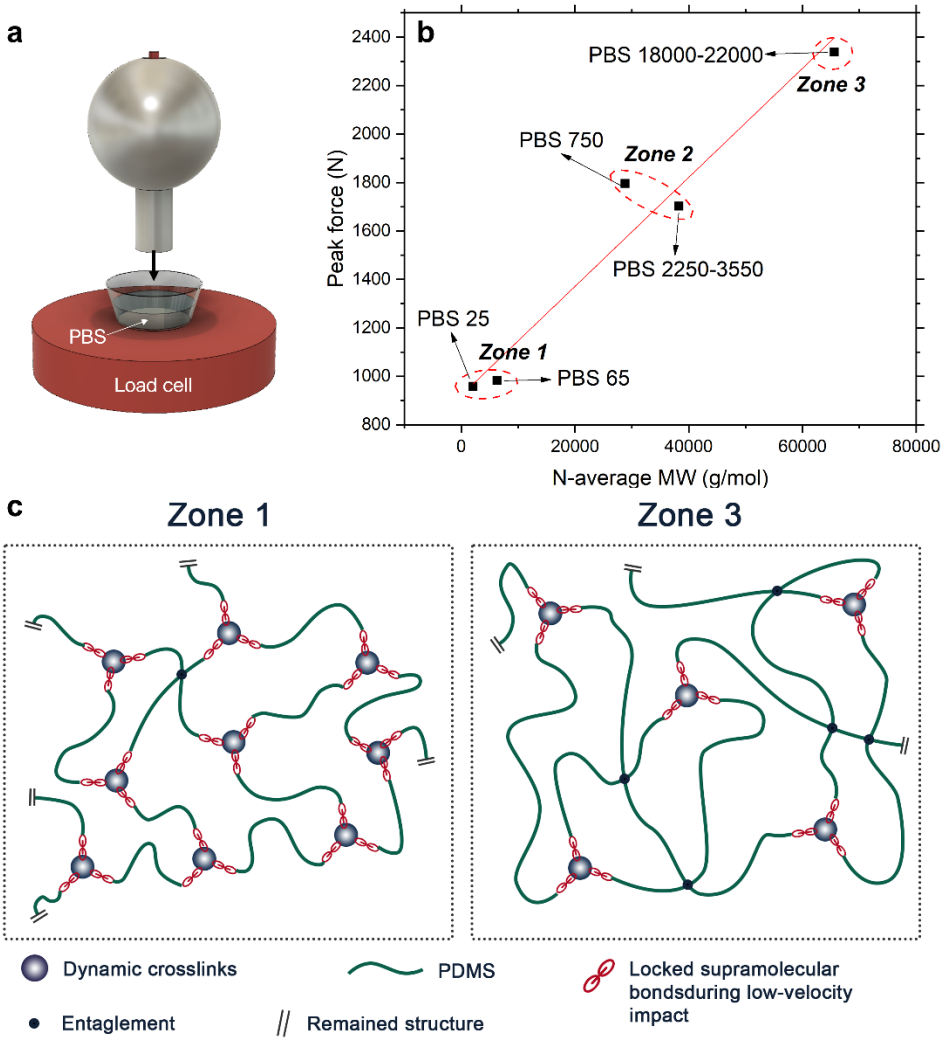

Figure 7.2 Drop weight impact test of PBS samples. a) Illustration of the testing setup; b) peak forces generated during impact test against MW of the PBS with three distinctive zones; c) schematic illustration of the molecular structure in Zone 1 (on the left) and Zone 3 (on the right) during low-velocity impact.

Based on the results of our own study and literature review, we concluded that dynamic crosslinking does not involve hydrogen bonding, dative bonding, or formation/exchange of boron anhydrides but is solely the result of associative dynamic exchange of Si-O-B covalent bonds.

It was also found that the viscoelastic properties of PBS are largely dependent on the B-O functionality of the boron compound. Tetrafunctional boron crosslinker demonstrated the highest rubbery plateau, which confirms the highest number of dynamic bonds, followed by trifunctional boric acid. In contrast, bifunctional phenylboronic acid provided only chain extension without any signs of gelation. Therefore, mechanical properties could be tuned by the right choice of boron functionality, which results in n-functional dynamic covalent bonds $(\text{-Si-O})_n\text{-B}$.

However, the exact mechanism of oxygen exchange in the Si-O-B bond remains unknown. It might involve an intermediate 4-coordinate state of boron atom of a short lifetime which bonds to neighboring oxygen with subsequent detachment – 3-coordinate → 4-coordinate → 3-coordinate. Oxygen can be provided by the hydroxyl groups (as proposed by Bloomfield) or from another Si-O-B bond (metathesis as suggested in another study[149] and was proven to exist in boronic esters[154] and boroxines[156,157]). Hence, further investigation is needed as well as examining the possibility of tuning the exchange reaction kinetics by manipulating the content of molecules containing free hydroxyls.

7.1.3 Comparison between STF and SSG, the potential for the substitution of conventional elastomeric foam

Two types of shear-stiffening materials - fumed silica suspension (STF) and PBS (SSG) have been studied alone in the previous chapters. However, it is of interest to compare their impact mitigation performance as both of them seem to be promising candidates for a substitution of a preexisting protective solution. The 11 mm thick layer of STF and SSG has been subjected to impacts of various energies along with the EVA foam of the same thickness, which is a typical cushioning material in sports protective equipment. To be concise only peak forces are shown here, which is enough to make a preliminary conclusion on the comparison (Figure 7.3).

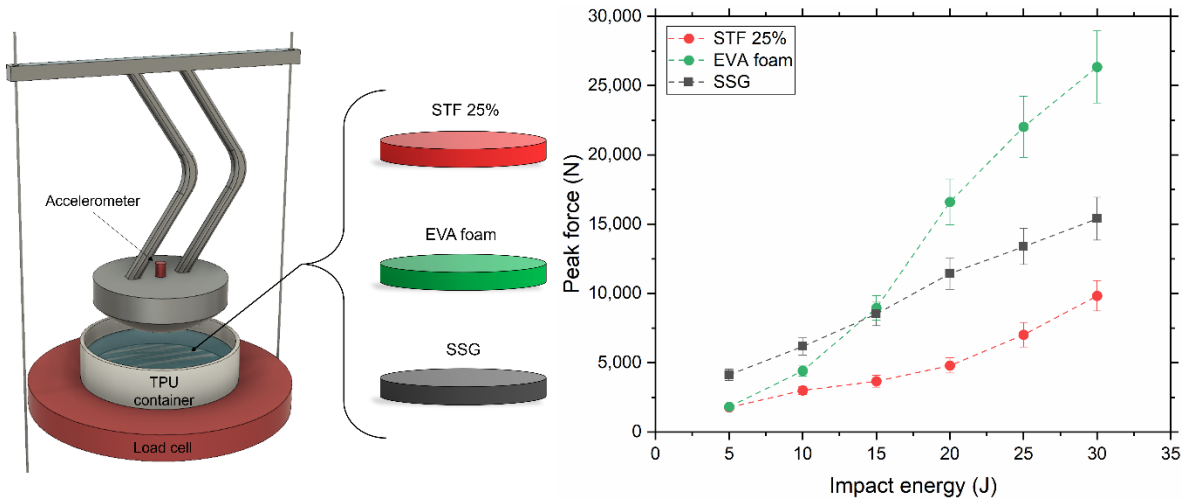

Figure 7.3 Illustration of drop weight impact setup for testing 11 mm thick layers of STF 25%, SSG, and EVA foam sample in a TPU container. On the right, peak force values at different impact energies; each data point is an average value over ten tests.

The effectiveness of this EVA foam protection is capped at 10 J; at higher energies, the maximum compression (when cells are collapsed) is reached, so the foam could only provide a viscoelastic dissipation from the EVA polymer bulk. Thus, peak forces are significantly higher starting from 15J. STF 25%, on the contrary, demonstrated significantly lower peak forces on the whole range of energies, making it superior to competitors. SSG showed consistent linear growth of the peak forces despite higher values at 5 and 10 J. It bypasses the effectiveness of EVA foam impact mitigation at 15 J, which makes it superior at higher impact energies.

An interesting feature of SSG, which can be highly beneficial for some applications, has been discovered; specifically, the reduction of SSG sample thickness to half or even a quarter leads to only a minor decline in impact dissipation (Figure 7.4). The 11 mm sample displayed the most consistent results throughout the six different energy levels with the lowest peak forces. The 11 mm SSG sample is the only sample that showed instantaneous elastic recovery after deformation occurred. Interestingly, a change in thickness does not change the trend but instead shifts the values to higher values. The thickness of SSG at 5.5 mm and below showed a marginal difference in shock attenuation properties, making the 2.7 mm thickness highly preferable in scenarios where thickness is preferred over performance. Despite the minimal thickness of SSG 2.7 mm, it is still more efficient at

higher impact energies than EVA foam. Besides, as was mentioned earlier, the efficiency of impact dissipation in STF is more sensitive to the layer thickness due to the mechanism in which a solid plug of jammed particles beneath the impactor generates high resistance only when it reaches the bottom boundary. The higher thickness of the plug guarantees higher impact dissipation through particle friction. Therefore, SSG could have an advantage over STF in a scenario where lightweight, thin protection is essential.

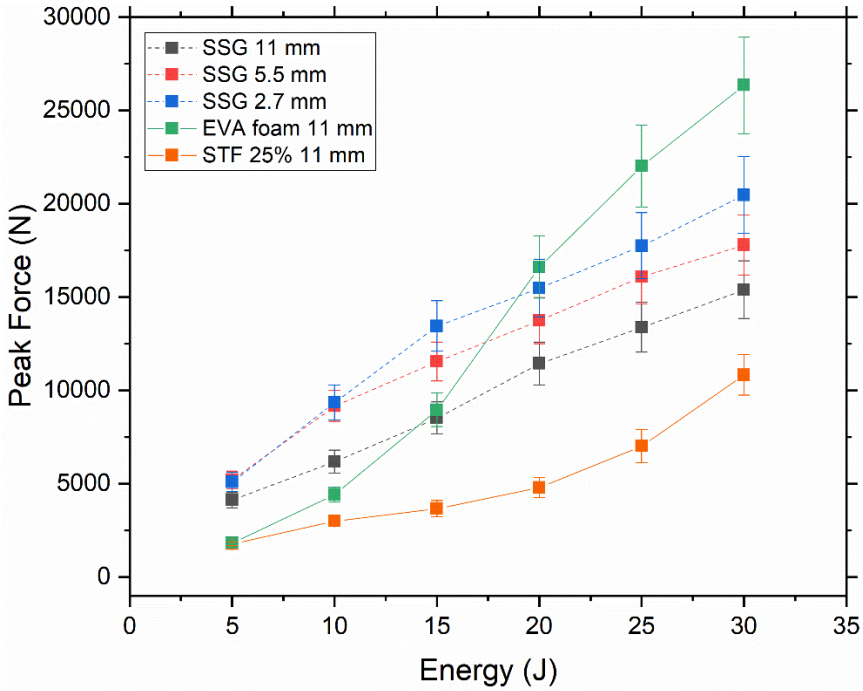

Figure 7.4 Results of the drop weight impact test for three SSG layers thicknesses (11, 5.5, and 2.7 mm) versus EVA foam and STF 25%. Peak forces are generated at different impact energies; each data point is an average value over ten tests.

7.2 Future Work

7.2.1 Challenge of their usage as a bulk for protection

Shear-stiffening materials (both STF and SSG) have been proven to be promising replacements for conventional protective materials. However, their use in the form of bulk protection is associated with several difficulties; one of the main ones is their fluidity in the absence of deformation, which leads to loss of shape or leakage from the protective

composite. This makes it impossible to use them in open structures and requires them to be sealed or encapsulated.

7.2.1.1 Encapsulation of STF

It was shown that jamming is highly beneficial for impact dissipation in fumed silica STF. However, to effectively utilize jamming for impact protection, the design of the structure is of critical importance. Specifically, the distance from the impact point to the boundary normal to impact (it defines the length of the plug of jammed particles, which constitutes the main impact dissipation), hardness of the boundary, and matrix structure need to be considered.

STF cannot be used on its own for bulk protection due to fluidity in the absence of impact. This poses another challenge for finding the proper technique and material for the sealing sheath (encapsulation). We tried to utilize the 3D printing encapsulation approach where STF was filled in the cylindrical sample with an internal 3D structure at the end of the printing right before the last layer. After it was filled to approximately 90% of the available volume, the printing was resumed, and the last layers sealed STF inside. This approach allowed to manipulate the topology of internal structure. Two classic lattice structures were chosen; one structure was honeycomb (closed-cell lattice structure), and the other was gyroid (co-continues TPMS structure). Both infill structures are presented in Figure 7.5 (a). In the case of the honeycomb structure, all cells are disconnected, and the fluid is locked in each cell. On the contrary, in the gyroid structure, there is an interconnected internal structure, and fluid can flow and be redistributed easily within the volume of the sample. STF 15% (15%w of fumed silica in PPG400) was used as a model fluid due to the difficulty of filling a more viscous liquid. Therefore, we need to take note that the model fluid is far from the most effective impact dissipation STF.

An unfilled honeycomb structure demonstrated a lower peak force compared to a filled one (Figure 7.5, b), likely due to the incompressible nature of fluid which restricted the buckling of the structure (which is the main mechanism of absorption in honeycomb structure[194]) and transferred energy directly to the load cell. The gyroid structure shows an opposite dependence. The filled gyroid structure significantly reduces peak force compared

to the unfilled samples. In this case, having the freedom to flow and to redistribute allows to absorb more impact since STF acts as it should, and the impact load is distributed in all directions. Another possible reason is that STF resists the deformation motion of the gyroid structure. Since STF has a much higher viscosity than air (for empty structures), friction is much greater, which requires more energy to be used to deform the structure. As an analogy, one can imagine a spring in the air, and in a viscous fluid, more work needs to be done in a viscous fluid to deform the spring. Therefore, the co-continues topology seems to be more suitable for shock absorption in flexible composites. However, walls of the FDM printed parts are known to possess limited durability in comparison to molded ones due to only partial fusion between layers[195,196]. The walls of the composites were the weakest points; high internal pressure generated during compressive impact tore the weakly bonded layers apart, which led to STF leaking out (Figure 7.5, c).

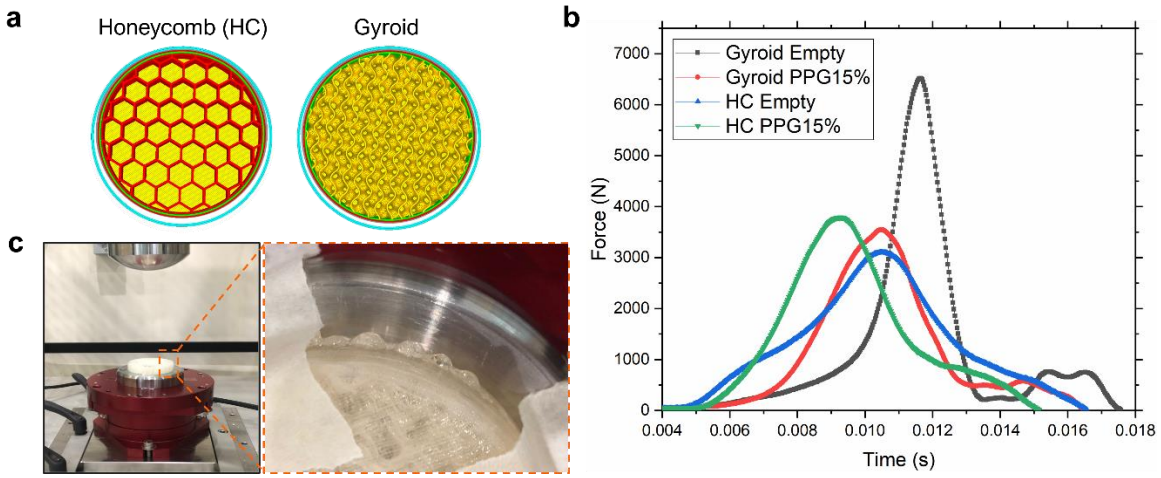

Figure 7.5 (**a**) 3D models of the honeycomb (closed-cell topology) and gyroid (continues topology) structures; (**b**) drop weight test results of the FDM printed composites from a self-produced PEBAX filament subjected to 7.5 J impact, two types of samples were produced for each structure – one, empty (unfilled) and another filled with STF 15% (PPG/fumed silica); (**c**) Photos of composites testing setup (on the left), broken walls of the matrix with STF leaking out (on the right).

Other encapsulation solutions should be considered which can withstand significantly greater impact loads without breaking. Some other approaches have been tried in the literature, such as Zhang et al.[71] developed an approach on how to produce double-wall

STF capsules. Premixed STF with 5%w of polyethyleneimine (PEI) is loaded into the syringe, then droplets of this mixture are instilled in the mixture of diisocyanate prepolymer and solvent. The shell is formed during the reaction of PEI with diisocyanate (polyurea shell), and the rest of the compounds are used to adjust the density, viscosity, and polarity of the mixture (Figure 7.6).

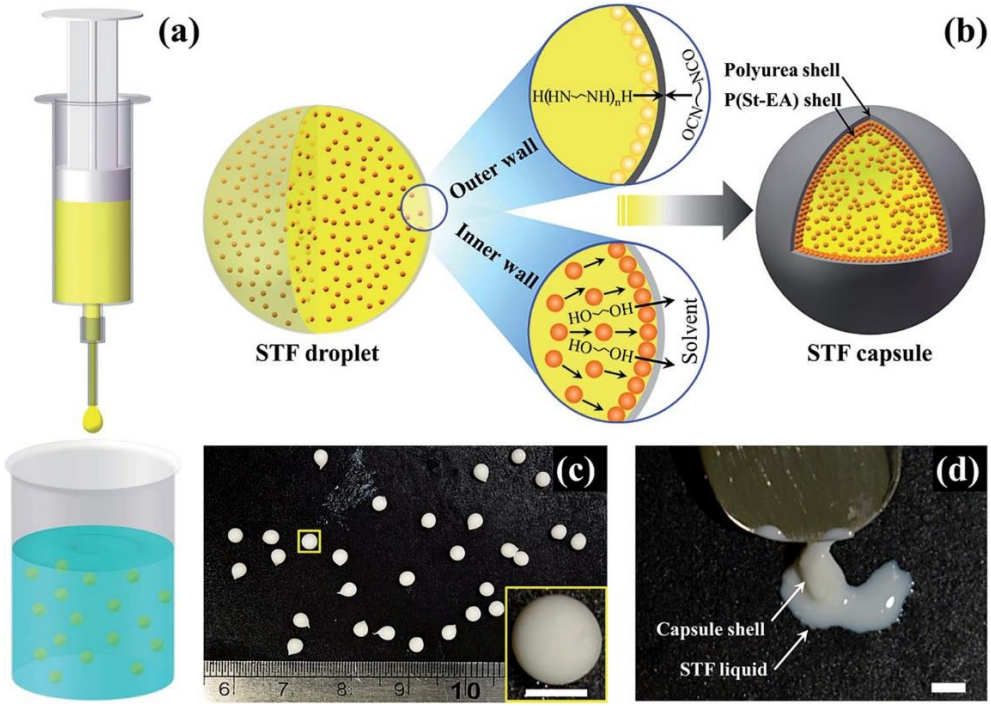

Figure 7.6 (**a**) Schematic of the setup used for STF encapsulation. (**b**) Illustration showing the formation mechanism and structure of the outer and inner walls of the STF capsule. (**c**) Optical image of the obtained capsules with one enlarged in the inset. (**d**) A broken STF capsule Reprinted with permission from reference [71]. © Royal Society of Chemistry

Lui et al.[197] used the orifice coagulation bath method for STF encapsulation. As described in Figure 7.7, prepared STF was put in a hydrophobic medium to form a W/O emulsion first; then, this mixture was poured into a hydrophilic medium to form a W/O/W emulsion. The last step was to inject droplets of the overall mixture into a $CaCl_2$ solution which triggered crosslinking of the sodium alginate external shell.

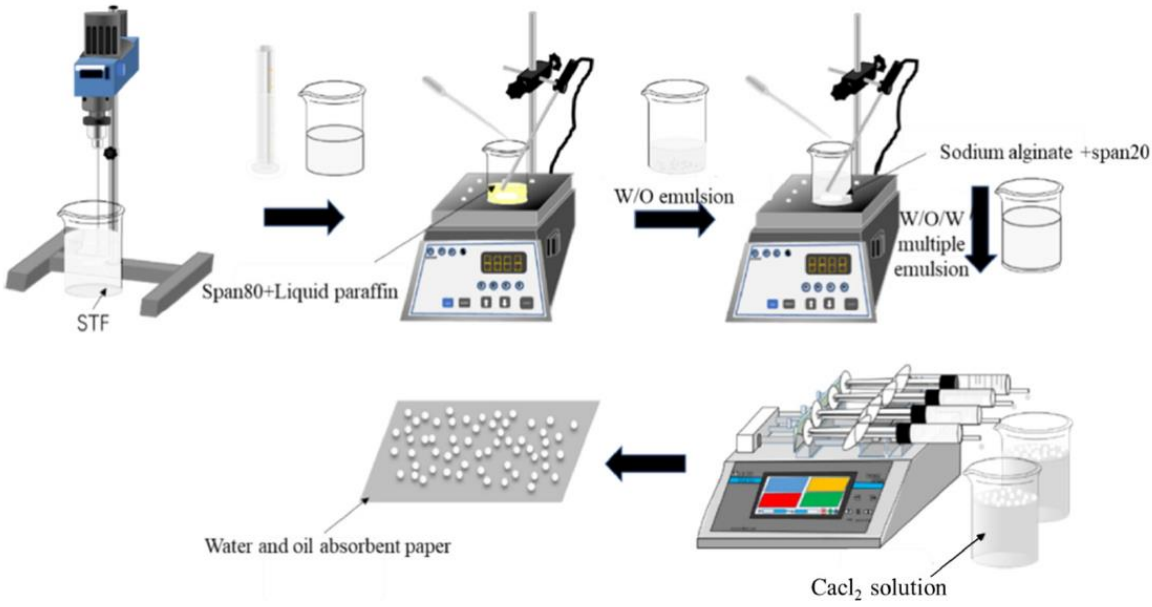

Figure 7.7 Orifice coagulation bath method for STF encapsulation. Reprinted with permission from reference [197] © 2020 Elsevier Ltd.

Though in both encapsulation approaches resulted, capsules were fragile and could not withstand repetitive impacts. These capsules could provide one-time protection only or be used to transport STF into another composite as it was used by Liu et al.[64] where the produced STF capsules with sodium alginate shells were incorporated in polyurethane foam on a stage of mixing polyol with isocyanate. This creates a great challenge to produce a durable yet flexible shell for STF capsules.

Another approach that was suggested in the patented work[198] is to create an emulsion with a liquid or liquid-like substance which can be solidified. For example, mix STF at a high volume fraction (around 40%) with silicone oil and a trifunctional crosslinker, and then cure the mixture to form a silicone/STF composite.

Soutrenon et al.[199] impregnated open-cell foam with STF under vacuum and using compression/relaxation cycles and then coated the foam with silicone to create an encapsulation shell. Caglayan et al.[200] directly mixed STF with polyol at low concentrations (1 and 2%w) prior to foaming via a reaction between isocyanate and polyol.

We believe that polymerization of the STF outer shell in W/O emulsion systems has the best flexibility in adjusting synthesis parameters and picking suitable chemicals. However, challenges of finding flexible yet durable shell material remain which creates research

prospects for the future. These capsules can be easily incorporated into polymer foams or any other protective systems to improve their impact dissipation.

7.2.1.2 PBS composites for impact protection

The same problem of fluidity in the absence of deformation (cold flow) is present in PBS, which makes it difficult to use it as bulk protection without encapsulation/sealing. Same encapsulation approaches can be utilized as were proposed for STF. Although, it possesses higher viscosity since it is in a gel state compared to STF. This opens more composite possibilities without the need to seal it completely.

One of the possible approaches is to develop a sandwich composite where the top and bottom layers will consist of the soft material which could hold the shape (can be 3D fabric or thin elastomeric foam), and a layer of PBS will be placed between these layers and will be stitched over the entire area to create closed cells as it is shown in Figure 7.8. The cell size, the thread thickness, and the seam allowance need to be optimized to make sure PBS will never leak out. This sandwich composite can provide good protection against low-velocity impacts and be worn with comfort due to the flexibility and flowability of PBS polymer.

Figure 7.8 Soft composite concept where PBS is the middle layer closed by 3D fabric from two sides and stitched over the area.

Another approach is to produce bicomponent core-shell yarns with PBS being a core material, and shell material can be any conventional polymers (such as polyester, nylon,

thermoplastic polyurethane, etc.). One of the most promising methods to produce such yarns is electrospinning. The field is rich with ideas for creating micro and nano-bicomponent core-shell fibers[201–203]. Electrospinning with coaxial double nozzle or shell formation of produced fibers from the oversaturated polymer solution is one of the most convenient ones. However, other methods are preferred if thicker yarns are required, such as two-component melt extruding and other methods. These yarns could be used for knitting fabric with various patterns (or even 3D fabric), which theoretically could provide protective properties upon impact for a person wearing it (Figure 7.9). However, the technique of yarn production has to be carefully designed and the parameters to be optimized.

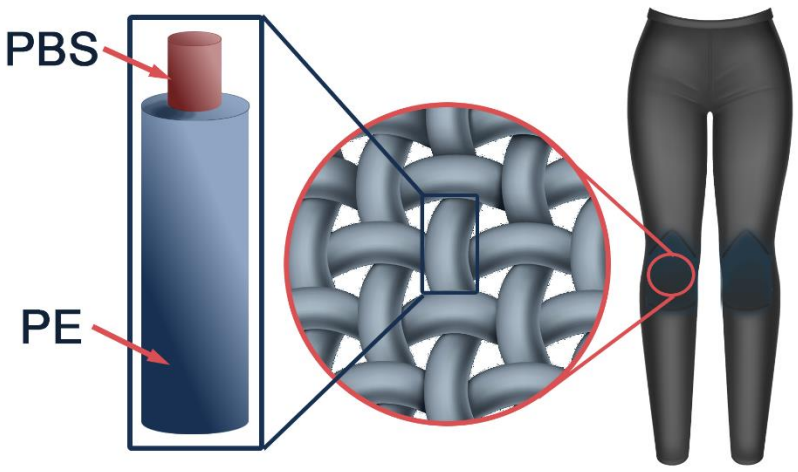

Figure 7.9 Concept of bicomponent yarns with PBS being a core and polyester (PE) a shell for protective fabrics.

REFERENCES

1 M. B. Clay, K. L. Glover and D. T. Lowe, *Journal of Chiropractic Medicine*, 2013, **12**, 230–251.

2 H. Rees, U. McCarthy Persson, E. Delahunt, C. Boreham and C. Blake, *Physical Therapy in Sport*, 2021, **52**, 45–53.

3 S. D. Barboza, C. Joseph, J. Nauta, W. van Mechelen and E. Verhagen, *Sports Medicine*, 2018, **48**, 849–866.

4 T. Farrington, G. Onambele-Pearson, R. L. Taylor, P. Earl and K. Winwood, *British Journal of Oral and Maxillofacial Surgery*, 2012, **50**, 233–238.

5 M. Avalle, G. Belingardi and R. Montanini, *International Journal of Impact Engineering*, 2001, **25**, 455–472.

6 F. Penta, G. Amodeo, A. Gloria, M. Martorelli, S. Odenwald and A. Lanzotti, *Applied Sciences*, 2018, **8**, 1174.

7 M. Nicotra, M. Moncalero, M. Messori, E. Fabbri, M. Fiorini and M. Colonna, *Procedia Engineering*, 2014, **72**, 678–683.

8 S. Kaewunruen, C. Ngamkhanong, M. Papaelias and C. Roberts, *Construction and Building Materials*, 2018, **187**, 1092–1102.

9 N. Mills, *Composites Science and Technology*, 2003, **63**, 2389–2400.

10 M. Tomin and Á. Kmetty, *Journal of Applied Polymer Science*, 2022, **139**, 51714.

11 C. P. Bogerd, J.-M. Aerts, S. Annaheim, P. Bröde, G. de Bruyne, A. D. Flouris, K. Kuklane, T. Sotto Mayor and R. M. Rossi, *International Journal of Industrial Ergonomics*, 2015, **45**, 1–12.

12 S. Gürgen, M. C. Kuşhan and W. Li, *Progress in Polymer Science*, 2017, **75**, 48–72.

13 C. Zhao, X. Gong, S. Wang, W. Jiang and S. Xuan, *Cell Reports Physical Science*, 2020, **1**, 100266.

14 S. Zhang, S. Wang, T. Hu, S. Xuan, H. Jiang and X. Gong, *Composites Part B: Engineering*, 2020, **180**, 107564.

15 C. Clavaud, A. Bérut, B. Metzger and Y. Forterre, *Proceedings of the National Academy of Sciences*, 2017, **114**, 5147–5152.

16 I. R. Peters, S. Majumdar and H. M. Jaeger, *Nature*, 2016, **532**, 214–217.

17 Y. Wang, S. Wang, C. Xu, S. Xuan, W. Jiang and X. Gong, *Composites Science and Technology*, 2016, **127**, 169–176.

18 E. Brown and H. M. Jaeger, *Reports on Progress in Physics*, 2014, **77**, 046602.

19 US7498276B2, 2003.

20 Q. He, S. Cao, Y. Wang, S. Xuan, P. Wang and X. Gong, *Composites Part A: Applied Science and Manufacturing*, 2018, **106**, 82–90.

21 U.S. Patent office, US 2009/0324927 A1, 2009.

22 United States Patent, 7608314 B2, 2009.

23 M. Kawaguchi, *Journal of Dispersion Science and Technology*, 2017, **38**, 642–660.

24 A. Amiri, G. Øye and J. Sjöblom, *Colloids and Surfaces A: Physicochemical and Engineering Aspects*, 2009, **349**, 43–54.

25 P. Alaee, M. Kamkar and M. Arjmand, *Langmuir*, 2022, **38**, 5006–5019.

26 Q. Wu, J. Ruan, B. Huang, Z. Zhou and J. Zou, *Journal of Central South University of Technology*, 2006, **13**, 1–5.

27 M. Tang, W. Wang, D. Xu and Z. Wang, *Industrial and Engineering Chemistry Research*, , DOI:10.1021/acs.iecr.6b03823.

28 Z. Liu, S. J. Picken and N. A. M. Besseling, *Macromolecules*, , DOI:10.1021/ma500632f.

29 L. A. Bloomfield, *arXiv.org [cond-mat.soft]*.

30 V. F. Gridina, A. L. Klebanskii, L. P. Dorofeyenko and L. Ye. Krupnova, *Polymer Science U.S.S.R.*, 1968, **9**, 2196–2202.

31 Q. Wu, H. Xiong, Y. Peng, Y. Yang, J. Kang, G. Huang, X. Ren and J. Wu, *ACS Applied Materials & Interfaces*, 2019, **11**, 19534–19540.

32 W. Jiang, X. Gong, S. Wang, Q. Chen, H. Zhou, W. Jiang and S. Xuan, *Applied Physics Letters*, 2014, **104**, 121915.

33 C. S. Boland, U. Khan, G. Ryan, S. Barwich, R. Charifou, A. Harvey, C. Backes, Z. Li, M. S. Ferreira, M. E. Möbius, R. J. Young and J. N. Coleman, *Science (1979)*, 2016, **354**, 1257–1260.

34 E. D'Elia, S. Barg, N. Ni, V. G. Rocha and E. Saiz, *Advanced Materials*, 2015, **27**, 4788–4794.

35 M. Tang, P. Zheng, K. Wang, Y. Qin, Y. Jiang, Y. Cheng, Z. Li and L. Wu, *Journal of Materials Chemistry A*, 2019, **7**, 27278–27288.

36 P. Wang, L. Yang, M. Sun, Z. Yang, S. Guo, G. Gao, L. Xu, D. Ji, W. Cao and J. Zhu, *Macromolecular Materials and Engineering*, 2021, **306**, 2000621.

37 P. Qu, C. Lv, Y. Qi, L. Bai and J. Zheng, *ACS Applied Materials & Interfaces*, 2021, **13**, 9043–9052.

38 W. L. A. Brooks and B. S. Sumerlin, *Chemical Reviews*, 2016, **116**, 1375–1397.

39 S. Wang, S. Xuan, M. Liu, L. Bai, S. Zhang, M. Sang, W. Jiang and X. Gong, *Soft Matter*, 2017, **13**, 2483–2491.

40 C. Xu, Y. Wang, J. Wu, S. Song, S. Cao, S. Xuan, W. Jiang and X. Gong, *Composites Science and Technology*, 2017, **153**, 168–177.

41 C. Zhao, C. Xu, S. Cao, S. Xuan, W. Jiang and X. Gong, *Smart Materials and Structures*, 2019, **28**, 075036.

42 G. Y. Foran, K. J. Harris, M. A. Brook, B. Macphail and G. R. Goward, *Macromolecules*, 2019, **52**, 1055–1064.

43 L. A. Mitrofanov, Ye. A. Sidorovich, A. V. Karlin and A. I. Marei, *Polymer Science U.S.S.R.*, 1969, **11**, 882–888.

44 A. P. Bapat, B. S. Sumerlin and A. Sutti, *Materials Horizons*, 2020, **7**, 694–714.

45 S. D. Bull, M. G. Davidson, J. M. H. van den Elsen, J. S. Fossey, A. T. A. Jenkins, Y.-B. Jiang, Y. Kubo, F. Marken, K. Sakurai, J. Zhao and T. D. James, *Accounts of Chemical Research*, 2013, **46**, 312–326.

46 P. Bourrianne, V. Niggel, G. Polly, T. Divoux and G. H. McKinley, .

47 M. van der Naald, L. Zhao, G. L. Jackson and H. M. Jaeger, *Soft Matter*, 2021, **17**, 3144–3152.

48 J. F. Morris, *Annual Review of Fluid Mechanics*, 2020, **52**, 121–144.

49 S. Wang, W. Jiang, W. Jiang, F. Ye, Y. Mao, S. Xuan and X. Gong, *Journal of Materials Chemistry C*, , DOI:10.1039/c4tc00903g.

50 A. Kurkin, V. Lipik, K. B. L. Tan, G. L. Seah, X. Zhang and A. I. Y. Tok, *Macromolecular Materials and Engineering*, 2021, **306**, 2100360.

51 L. E. Gates, *Evaluation and Development of Fluid Armor Systems AD0848937*, Fort Belvoir, 1968.

52 T. C. de Goede, K. G. de Bruin and D. Bonn, *Scientific Reports*, 2019, **9**, 1250.

53 X. Gong, Y. Xu, W. Zhu, S. Xuan, W. Jiang and W. Jiang, *Journal of Composite Materials*, 2014, **48**, 641–657.

54 M. Fahool and A. R. Sabet, *International Journal of Impact Engineering*, 2016, **90**, 61–71.

55 M. J. Decker, C. J. Halbach, C. H. Nam, N. J. Wagner and E. D. Wetzel, *Composites Science and Technology*, 2007, **67**, 565–578.

56 C. D. Cwalina, C. M. McCutcheon, R. D. Dombrowski and N. J. Wagner, *Composites Science and Technology*, 2016, **131**, 61–66.

57 A. Majumdar, B. S. Butola and A. Srivastava, *Materials & Design (1980-2015)*, 2014, **54**, 295–300.

58 Q. Zhang, Z. Qin, R. Yan, S. Wei, W. Zhang, S. Lu and L. Jia, *Composite Structures*, 2021, **266**, 113806.

59 S. Gürgen and M. C. Kuşhan, *Materials Science Forum*, 2016, **880**, 132–135.

60 M. A. Abtew, F. Boussu, P. Bruniaux, C. Loghin and I. Cristian, *Composite Structures*, 2019, **223**, 110966.

61 A. Srivastava, A. Majumdar and B. S. Butola, *Critical Reviews in Solid State and Materials Sciences*, 2012, **37**, 115–129.

62 D. Li, R. Wang, F. Guan, Y. Zhu and F. You, *Journal of Materials Research and Technology*, 2022, **18**, 3673–3683.

63 M. A. Dawson, *International Journal of Impact Engineering*, 2009, **36**, 1288–1295.

64 X. Liu, J. Huo, T. T. Li, H. Wang, L. Wu, J. H. Lin and C. W. Lou, *Materials Letters*, , DOI:10.1016/j.matlet.2020.127580.

65 F. J. Galindo-Rosales, S. Martínez-Aranda and L. Campo-Deaño, *Materials & Design*, 2015, **82**, 326–334.

66 K. Fu, H. Wang, L. Chang, M. Foley, K. Friedrich and L. Ye, *Composites Science and Technology*, , DOI:10.1016/j.compscitech.2018.06.013.

67 L. Wu, J. Wang, Q. Jiang, Z. Lu, W. Wang and J.-H. Lin, *Journal of Sandwich Structures & Materials*, 2020, **22**, 1274–1291.

68 F. Zhao, L. Wu, Z. Lu, J.-H. Lin and Q. Jiang, *Materials & Design*, 2022, **213**, 110375.

69 J. N. Fowler, A. A. Pallanta, C. B. Swanik and N. J. Wagner, *Journal of Biomechanical Engineering*, , DOI:10.1115/1.4029982.

70 X. Liu, J.-L. Huo, T.-T. Li, H.-K. Peng, J.-H. Lin and C.-W. Lou, *Polymers (Basel)*, 2019, **11**, 519.

71 H. Zhang, X. Zhang, Q. Chen, X. Li, P. Wang, E.-H. Yang, F. Duan, X. Gong, Z. Zhang and J. Yang, *Journal of Materials Chemistry A*, 2017, **5**, 22472–22479.

72 C. Storm, J. J. Pastore, F. C. MacKintosh, T. C. Lubensky and P. A. Janmey, *Nature*, 2005, **435**, 191–194.

73 K. A. Erk, K. J. Henderson and K. R. Shull, *Biomacromolecules*, 2010, **11**, 1358–1363.

74 K. Bertula, L. Martikainen, P. Munne, S. Hietala, J. Klefström, O. Ikkala and Nonappa, *ACS Macro Letters*, 2019, **8**, 670–675.

75 M. Jaspers, M. Dennison, M. F. J. Mabesoone, F. C. MacKintosh, A. E. Rowan and P. H. J. Kouwer, *Nature Communications*, 2014, **5**, 5808.

76 P. de Almeida, M. Jaspers, S. Vaessen, O. Tagit, G. Portale, A. E. Rowan and P. H. J. Kouwer, *Nature Communications*, 2019, **10**, 609.

77 E. Z. Casassa, A. M. Sarquis and C. H. van Dyke, *Journal of Chemical Education*, 1986, **63**, 57.

78 S. Spoljaric, A. Salminen, N. D. Luong and J. Seppälä, *European Polymer Journal*, 2014, **56**, 105–117.

79 J. Han, T. Lei and Q. Wu, *Carbohydrate Polymers*, 2014, **102**, 306–316.

80 T. Billiet, M. Vandenhaute, J. Schelfhout, S. van Vlierberghe and P. Dubruel, *Biomaterials*, 2012, **33**, 6020–6041.

81 L. Xiaoke, Y. Kejing, F. Qianqian and Q. Kun, *Smart Materials and Structures*, 2019, **28**, 055017.

82 S. Wang, S. Xuan, Y. Wang, C. Xu, Y. Mao, M. Liu, L. Bai, W. Jiang and X. Gong, *ACS Applied Materials & Interfaces*, 2016, **8**, 4946–4954.

83 G. Bossis and J. F. Brady, *The Journal of Chemical Physics*, 1989, **91**, 1866–1874.

84 R. L. Hoffman, *Journal of Colloid and Interface Science*, 1974, **46**, 491–506.

85 J. Comtet, G. Chatté, A. Niguès, L. Bocquet, A. Siria and A. Colin, *Nature Communications*, 2017, **8**, 15633.

86 R. Mari, R. Seto, J. F. Morris and M. M. Denn, *Journal of Rheology*, 2014, **58**, 1693–1724.

87 R. Seto, R. Mari, J. F. Morris and M. M. Denn, *Physical Review Letters*, 2013, **111**, 218301.

88 N. Y. C. Lin, B. M. Guy, M. Hermes, C. Ness, J. Sun, W. C. K. Poon and I. Cohen, *Physical Review Letters*, 2015, **115**, 228304.

89 A. Singh, R. Mari, M. M. Denn and J. F. Morris, *Journal of Rheology*, 2018, **62**, 457–468.

90 A. Singh, S. Pednekar, J. Chun, M. M. Denn and J. F. Morris, *Physical Review Letters*, 2019, **122**, 098004.

91 R. Mari and R. Seto, *Soft Matter*, 2019, **15**, 6650–6659.

92 A. Singh, C. Ness, R. Seto, J. J. de Pablo and H. M. Jaeger, *Physical Review Letters*, 2020, **124**, 248005.

93 C.-P. Hsu, S. N. Ramakrishna, M. Zanini, N. D. Spencer and L. Isa, *Proceedings of the National Academy of Sciences*, 2018, **115**, 5117–5122.

94 N. M. James, H. Xue, M. Goyal and H. M. Jaeger, *Soft Matter*, 2019, **15**, 3649–3654.

95 C.-P. Hsu, J. Mandal, S. N. Ramakrishna, N. D. Spencer and L. Isa, *Nature Communications*, 2021, **12**, 1477.

96 N. M. James, E. Han, R. A. L. de la Cruz, J. Jureller and H. M. Jaeger, *Nature Materials*, 2018, **17**, 965–970.

97 N. M. James, C.-P. Hsu, N. D. Spencer, H. M. Jaeger and L. Isa, *The Journal of Physical Chemistry Letters*, 2019, **10**, 1663–1668.

98 W. Yang, Y. Wu, X. Pei, F. Zhou and Q. Xue, *Langmuir*, 2017, **33**, 1037–1042.

99 B. M. Guy, M. Hermes and W. C. K. Poon, *Physical Review Letters*, 2015, **115**, 088304.

100 S. Pednekar, J. Chun and J. F. Morris, *Soft Matter*, 2017, **13**, 1773–1779.

101 A. D. Moriana, T. Tian, V. Sencadas and W. Li, *Korea-Australia Rheology Journal*, 2016, **28**, 197–205.

102 B. J. Maranzano and N. J. Wagner, *The Journal of Chemical Physics*, 2002, **117**, 10291–10302.

103 B.-W. Lee, I.-J. Kim and C.-G. Kim, *Journal of Composite Materials*, 2009, **43**, 2679–2698.

104 S. S. Shenoy and N. J. Wagner, *Rheologica Acta*, 2005, **44**, 360–371.

105 Y. Otsubo, *Journal of Colloid and Interface Science*, 1999, **215**, 99–105.

106 K. Beazley, in *Rheometry. Industrial Applications*, ed. K. Walters, John Wiley & Sons Inc., Chichester, 1980, pp. 339–407.

107 H. A. Barnes, *Journal of Rheology*, 1989, **33**, 329–366.

108 E. D. Wetzel, in *AIP Conference Proceedings*, AIP, 2004, pp. 288–293.

109 A. Kurkin, V. Lipik, X. Zhang and A. Tok, *Polymers (Basel)*, 2022, **14**, 2768.

110 A. Norbert and W. Johann, *Annales de Chimie Science des Matériaux*, 1999, **24**, 92.

111 J. Warren, S. Offenberger, H. Toghiani, C. U. Pittman, T. E. Lacy and S. Kundu, *ACS Applied Materials & Interfaces*, 2015, **7**, 18650–18661.

112 S. R. Raghavan and S. A. Khan, *Journal of Colloid and Interface Science*, 1997, **185**, 57–67.

113 X.-Q. Liu, R.-Y. Bao, X.-J. Wu, W. Yang, B.-H. Xie and M.-B. Yang, *RSC Advances*, 2015, **5**, 18367–18374.

114 Q. Zhang, C. Wu, Y. Song and Q. Zheng, *Polymer (Guildf)*, 2018, **148**, 400–406.

115 S. Majumdar, I. R. Peters, E. Han and H. M. Jaeger, *Physical Review E*, 2017, **95**, 012603.

116 A. Feray, N. Szely, E. Guillet, M. Hullo, F.-X. Legrand, E. Brun, M. Pallardy and A. Biola-Vidamment, *Nanomaterials*, 2020, **10**, 425.

117 K. Fu, H. Wang, Y. X. Zhang, L. Ye, J. P. Escobedo, P. J. Hazell, K. Friedrich and S. Dai, *International Journal of Impact Engineering*, 2020, **139**, 103525.

118 S. R. Waitukaitis and H. M. Jaeger, *Nature*, 2012, **487**, 205–209.

119 D. Bi, J. Zhang, B. Chakraborty and R. P. Behringer, *Nature*, 2011, **480**, 355–358.

120 E. Han, I. R. Peters and H. M. Jaeger, *Nature Communications*, 2016, **7**, 12243.

121 E. Han, L. Zhao, N. van Ha, S. T. Hsieh, D. B. Szyld and H. M. Jaeger, *Physical Review Fluids*, 2019, **4**, 063304.

122 E. Han, M. Wyart, I. R. Peters and H. M. Jaeger, *Physical Review Fluids*, 2018, **3**, 073301.

123 B. Allen, B. Sokol, S. Mukhopadhyay, R. Maharjan and E. Brown, *Physical Review E*, 2018, **97**, 052603.

124 N. Seetapan, A. Fuongfuchat, D. Sirikittikul and N. Limparyoon, *Journal of Polymer Research*, 2013, **20**, 183.

125 D. Zhang, N. Jiang, X. Chen and B. He, *Journal of Applied Polymer Science*, 2020, **137**, 48421.

126 G. A. Zinchenko, V. P. Mileshkevich and N. V. Kozlova, *Polymer Science U.S.S.R.*, 1981, **23**, 1421–1429.

127 R. L. Vale, *Journal of the Chemical Society* , 1960, 2252–2257.

128 X. Li, D. Zhang, K. Xiang and G. Huang, *RSC Adv.*, 2014, **4**, 32894–32901.

129 Y. Wang, L. Ding, C. Zhao, S. Wang, S. Xuan, H. Jiang and X. Gong, *Composites Science and Technology*, 2018, **168**, 303–311.

130 M. Tang, W. Wang, D. Xu and Z. Wang, *Industrial & Engineering Chemistry Research*, 2016, **55**, 12582–12589.

131 S. Qi, J. Fu, Y. Xie, Y. Li, R. Gan and M. Yu, *Composites Science and Technology*, 2019, **183**, 107817.

132 H. Pang, S. Xuan, T. Liu and X. Gong, *Soft Matter*, 2015, **11**, 6893–6902.

133 K. Danas, S. V. Kankanala and N. Triantafyllidis, *Journal of the Mechanics and Physics of Solids*, 2012, **60**, 120–138.

134 M. Ashtiani, S. H. Hashemabadi and A. Ghaffari, *Journal of Magnetism and Magnetic Materials*, 2015, **374**, 716–730.

135 S. Wang, S. Xuan, W. Jiang, W. Jiang, L. Yan, Y. Mao, M. Liu and X. Gong, *Journal of Materials Chemistry A*, 2015, **3**, 19790–19799.

136 F. Yuan, S. Wang, S. Zhang, Y. Wang, S. Xuan and X. Gong, *Journal of Materials Chemistry C*, 2019, **7**, 8412–8422.

137 S. Zhang, S. Wang, Y. Wang, X. Fan, L. Ding, S. Xuan and X. Gong, *Composites Part A: Applied Science and Manufacturing*, 2018, **112**, 197–206.

138 S. Wang, L. Gong, Z. Shang, L. Ding, G. Yin, W. Jiang, X. Gong and S. Xuan, *Advanced Functional Materials*, 2018, **28**, 1707538.

139 D. P. O'Driscoll, V. Vega-Mayoral, I. Harley, C. S. Boland and J. N. Coleman, *2D Materials*, 2018, **5**, 035042.

140 Y. Wang, S. Wang, C. Xu, S. Xuan, W. Jiang and X. Gong, *Composites Science and Technology*, , DOI:10.1016/j.compscitech.2016.03.009.

141 A. Juhász, P. Tasnádi and L. Fábry, *Physics Education*, 1984, **19**, 315.

142 United States Patent Office, 2431878, 1947.

143 M. Wick, *Kunststoffe*, 1960, **50**, 433–436.

144 L. Zepeda-Velazquez, B. Macphail and M. A. Brook, *Polymer Chemistry*, 2016, **7**, 4458–4466.

145 J. P. LORAND and J. O. EDWARDS, *The Journal of Organic Chemistry*, 1959, **24**, 769–774.

146 R. Nishiyabu, Y. Kubo, T. D. James and J. S. Fossey, *Chemical Communications*, 2011, **47**, 1106.

147 A. J. Barry, *Journal of Applied Physics*, 1946, **17**, 1020–1024.

148 S. J. Singer, 1963, pp. 1–68.

149 R. Heyes and J. C. Lockhart, *Journal of the Chemical Society A: Inorganic, Physical, Theoretical*, 1968, 326.

150 P. J. Flory, *J Am Chem Soc*, 1941, **63**, 3083–3090.

151 W. H. Stockmayer, *The Journal of Chemical Physics*, 1943, **11**, 45–55.

152 M. Gosecki and M. Gosecka, *Polymers (Basel)*, 2022, **14**, 842.

153 X. Zhang, Y. Zhao, S. Wang and X. Jing, *Materials Chemistry Frontiers*, 2021, **5**, 5534–5548.

154 M. Röttger, T. Domenech, R. van der Weegen, A. Breuillac, R. Nicolaÿ and L. Leibler, *Science (1979)*, 2017, **356**, 62–65.

155 J. J. Cash, T. Kubo, D. J. Dobbins and B. S. Sumerlin, *Polymer Chemistry*, 2018, **9**, 2011–2020.

156 A. L. Korich and P. M. Iovine, *Dalton Trans.*, 2010, **39**, 1423–1431.

157 P. M. Iovine, C. R. Gyselbrecht, E. K. Perttu, C. Klick, A. Neuwelt, J. Loera, A. G. DiPasquale, A. L. Rheingold and J. Kua, *Dalton Transactions*, 2008, 3791.

158 W. A. Ogden and Z. Guan, *J Am Chem Soc*, 2018, **140**, 6217–6220.

159 Y. Tokunaga, H. Ueno and Y. Shimomura, *HETEROCYCLES*, 2007, **74**, 219.

160 A. I. Gómez-Merino, J. J. Jiménez-Galea, F. J. Rubio-Hernández, J. L. Arjona-Escudero and I. M. Santos-Ráez, *Processes*, 2020, **8**, 1535.

161 E. Brown and H. M. Jaeger, *Science (1979)*, 2011, **333**, 1230–1231.

162 X. Cheng, J. H. McCoy, J. N. Israelachvili and I. Cohen, *Science (1979)*, 2011, **333**, 1276–1279.

163 D.-M. Liu, *Journal of Materials Science*, 2000, **35**, 5503–5507.

164 A. Fall, F. Bertrand, D. Hautemayou, C. Mezière, P. Moucheront, A. Lemaître and G. Ovarlez, *Physical Review Letters*, 2015, **114**, 098301.

165 E. Brown and H. M. Jaeger, *Journal of Rheology*, 2012, **56**, 875–923.

166 L. D. S. Yadav, *Organic Spectroscopy*, Springer Netherlands, Dordrecht, 2005.
167 F. v. Drozdov, S. A. Milenin, V. v. Gorodov, N. v. Demchenko, M. I. Buzin and A. M. Muzafarov, *Journal of Organometallic Chemistry*, 2019, **891**, 72–77.
168 M. Rubinstein and A. N. Semenov, *Macromolecules*, 1998, **31**, 1386–1397.
169 M. Rubinstein and A. N. Semenov, *Macromolecules*, 2001, **34**, 1058–1068.
170 A. L. Larsen, K. Hansen, P. Sommer-Larsen, O. Hassager, A. Bach, S. Ndoni and M. Jørgensen, *Macromolecules*, 2003, **36**, 10063–10070.
171 L. J. Fetters, D. J. Lohse, S. T. Milner and W. W. Graessley, *Macromolecules*, 1999, **32**, 6847–6851.
172 M. Doi and S. F. Edwards, *The Theory of Polymer Dynamics*, Clarendon Press, Oxford, 3rd edn., 1986.
173 P. E. Reed, 1999, pp. 57–60.
174 S. Wang, L. Ding, X. Fan, W. Jiang and X. Gong, *Nano Energy*, 2018, **53**, 863–870.
175 J. Chen, G. Zhu, W. Yang, Q. Jing, P. Bai, Y. Yang, T.-C. Hou and Z. L. Wang, *Advanced Materials*, 2013, **25**, 6094–6099.
176 G. Zhu, B. Peng, J. Chen, Q. Jing and Z. Lin Wang, *Nano Energy*, 2015, **14**, 126–138.
177 S. Wang, L. Ding, Y. Wang and X. Gong, *Nano Energy*, 2019, **59**, 434–442.
178 F. Yuan, S. Wang, S. Zhang, Y. Wang, S. Xuan and X. Gong, *Journal of Materials Chemistry C*, 2019, **7**, 8412–8422.
179 R. Nishiyabu, Y. Kubo, T. D. James and J. S. Fossey, *Chem. Commun.*, 2011, **47**, 1124–1150.
180 O. R. Cromwell, J. Chung and Z. Guan, *J Am Chem Soc*, 2015, **137**, 6492–6495.
181 D. Peak, G. W. Luther and D. L. Sparks, *Geochimica et Cosmochimica Acta*, 2003, **67**, 2551–2560.
182 P. Qu, C. Lv, Y. Qi, L. Bai and J. Zheng, *ACS Applied Materials & Interfaces*, 2021, **13**, 9043–9052.
183 L. Li, J. Zhao, H. Li and T. Zhao, *Applied Organometallic Chemistry*, 2013, **27**, 723–728.
184 X. Zhao, C. Zang, Y. Sun, K. Liu, Y. Wen and Q. Jiao, *Journal of Materials Science*, 2018, **53**, 1167–1177.
185 G. D. Soraru, F. Babonneau, C. Gervais and N. Dallabona, *Journal of Sol-Gel Science and Technology*, 2000, **18**, 11–19.
186 C. Bao, Z. Guo, H. Sun and J. Sun, *ACS Applied Materials & Interfaces*, 2019, **11**, 9478–9486.
187 C. Kim, H. Ejima and N. Yoshie, *Journal of Materials Chemistry A*, 2018, **6**, 19643–19652.
188 P. J. Flory, *J Am Chem Soc*, 1941, **63**, 3091–3096.
189 A. J. Barry, *Journal of Applied Physics*, 1946, **17**, 1020–1024.
190 J. A. Faniran and H. F. Shurvell, *Canadian Journal of Chemistry*, 1968, **46**, 2089–2095.
191 A. Haaland, *Angewandte Chemie International Edition in English*, 1989, **28**, 992–1007.

192 S. Balcı, N. A. Sezgi and E. Eren, *Industrial & Engineering Chemistry Research*, 2012, **51**, 11091–11096.
193 C. Chen, H.-F. Fei, J. J. Watkins and A. J. Crosby, *Journal of Materials Chemistry A*, 2022, **10**, 11667–11675.
194 V. Caccese, J. R. Ferguson and M. A. Edgecomb, *Composite Structures*, 2013, **100**, 404–412.
195 I. J. Solomon, P. Sevvel and J. Gunasekaran, *Materials Today: Proceedings*, 2021, **37**, 509–514.
196 D. Popescu, A. Zapciu, C. Amza, F. Baciu and R. Marinescu, *Polymer Testing*, 2018, **69**, 157–166.
197 X. Liu, J.-L. Huo, T.-T. Li, H.-K. Peng, J.-H. Lin and C.-W. Lou, *Polymers (Basel)*, 2019, **11**, 519.
198 United States Patent, 20060234572A1, 2006.
199 M. Soutrenon and V. Michaud, *Smart Materials and Structures*, , DOI:10.1088/0964-1726/23/3/035022.
200 C. Caglayan, I. Osken, A. Ataalp, H. S. Turkmen and H. Cebeci, *Composite Structures*, 2020, **243**, 112171.
201 M. Naeimirad, A. Zadhoush, R. Kotek, R. Esmaeely Neisiany, S. Nouri Khorasani and S. Ramakrishna, *Journal of Applied Polymer Science*, 2018, **135**, 46265.
202 A. L. Yarin, *Polymers for Advanced Technologies*, 2011, **22**, 310–317.
203 R. Sahay, V. Thavasi and S. Ramakrishna, *Journal of Nanomaterials*, 2011, **2011**, 1–17.

List of publications

[1] **A. Kurkin**, V. Lipik, X. Zhang and A. Tok. In Situ Observation of Shear-Induced Jamming Front Propagation during Low-Velocity Impact in Polypropylene Glycol/Fumed Silica Shear Thickening Fluids. ***Polymers*** 14 (14), 2768 (**2022**).
[2] **A. Kurkin**, V. Lipik, K. Tan, G. L. Seah, X. Zhang and A. Tok. Correlations Between Precursor Molecular Weight and Dynamic Mechanical Properties of Polyborosiloxane (PBS). ***Macromolecular Materials and Engineering*** 306 (11), 2100360 (**2021**).
[3] X. Zhang, P. Wang, **A. Kurkin**, Q. Chen, X. Gong, Z. Zhang, E.-H. Yang, J. Yang. Mechanical response of shear thickening fluid filled composite subjected to different strain rates. ***International Journal of Mechanical Sciences*** 196, 106304, (**2021**).